

# Optimizing Velocities and Transports for Complex Coastal Regions and Archipelagos

Patrick J. Haley, Jr.<sup>a,b</sup>, Arpit Agarwal<sup>a,c</sup>, Pierre F. J. Lermusiaux<sup>a,d</sup>

<sup>a</sup>Massachusetts Institute of Technology, Cambridge, MA-02139, USA

<sup>b</sup>e-mail: [phaley@mit.edu](mailto:phaley@mit.edu), <sup>c</sup>[arpit@mit.edu](mailto:arpit@mit.edu), <sup>d</sup>[pierrel@mit.edu](mailto:pierrel@mit.edu)

---

## Abstract

We derive and apply a methodology for the initialization of velocity and transport fields in complex multiply-connected regions with multiscale dynamics. The result is initial fields that are consistent with observations, complex geometry and dynamics, and that can simulate the evolution of ocean processes without large spurious initial transients. A class of constrained weighted least squares optimizations is defined to best fit first-guess velocities while satisfying the complex bathymetry, coastline and divergence strong constraints. A weak constraint towards the minimum inter-island transports that are in accord with the first-guess velocities provides important velocity corrections in complex archipelagos. In the optimization weights, the minimum distance and vertical area between pairs of coasts are computed using a Fast Marching Method. Additional information on velocity and transports are included as strong or weak constraints. We apply our methodology around the Hawaiian islands of Kauai/Niihau, in the Taiwan/Kuroshio region and in the Philippines Archipelago. Comparisons with other common initialization strategies, among hindcasts from these initial conditions (ICs), and with independent *in situ* observations show that our optimization corrects transports, satisfies boundary conditions and redirects currents. Differences between the hindcasts from these different ICs are found to grow for at least 2-3 weeks. When compared to independent *in situ* observations, simulations from our optimized ICs are shown to have the smallest errors.

*Key words:* field mapping, least squares, weak constraints, fast marching method, downscaling, two-way nesting, primitive-equation, Euler-Lagrange, free-surface, reduced-dynamics, multiscale, islands, multiply-connected, complex domain

---

## 1 Introduction

Imagine that the Lorenz-63 system (Lorenz, 1963) was representative of the real ocean. Imagine that your goal was to initialize a useful prediction for this system, from imperfect measurements. By useful prediction, we mean the capability of predicting for some time, in the ideal case up to the local predictability limit (initial-condition-dependent). If you knew that the initial state was not zero, why would you spin-up from zero? If one of the state variables was measured initially, but with uncertainty, someone may guess an initial condition by running the Lorenz model for some time, keeping the measured state variable fixed. Unless that person is so lucky to stop at the right time, the likelihood of the result being close to the true initial condition is very small. Hence, being on the “attractor” of the model is not enough. What we need is to be in a neighborhood of the true initial state, such that if we start a prediction from that state, some predictive capability exists. We remark that in that case, the subsequent assimilation of limited data will also have a much easier time at controlling error growth. And second, if the model was imperfect, running the model for too long in the initial adjustment may also lead to large errors. The present manuscript is concerned with such estimation of initial ocean conditions, focusing on regions with complex geometries and multiscale dynamics governed by hydrostatic primitive equations (PEs) (e.g. Cushman-Roisin and Beckers, 2010) with a free ocean surface, referred to next simply as free-surface PEs (e.g. Haley and Lermusiaux, 2010, hereafter denoted as HL10).

The estimation of initial conditions (ICs) for ocean simulations is not a new problem (Wunsch, 1996). For longer time-scale prediction (e.g. climatological studies) the use of spin-up from rest to initialize simulations has been frequent (Artale et al., 2010; Maslowski et al., 2004; Schiller et al., 2008; Timmermann et al., 2005; Zhang and Steele, 2007) in part because of lack of data for initialization. Even for shorter time-scale predictions with more synoptic information, spin-up from rest is still often used. However, studies show that using ICs which are not in dynamical balance (e.g. the zero velocities at the start of the spin-up from rest) can lead to numerical shock (Oke et al., 2002) and erroneous dynamics (Robinson, 1996, 1999; Lozano et al., 1996; Beşiktepe et al., 2003). Some variations on the spin-up procedure have been used to control shocks, including: multi-stage spin-up schemes (Cazes-Boezio et al., 2008; Jiang et al., 2009); spin-up with data assimilation (Balmaseda et al., 2008; Balmaseda and Anderson, 2009; Bender and Ginis, 2000; Cazes-

38 Boezio et al., 2008); and spin-up with relaxation to a reference field (Halli-  
39 well et al., 2008; Sandery et al., 2011). Other methods to incorporate more  
40 synoptic scales and dynamics into the initial fields include feature models  
41 (FM; Gangopadhyay et al., 2003, 2011, 2013; Schmidt and Gangopadhyay,  
42 2013; Falkovich et al., 2005; Yablonsky and Ginis, 2008) and downscaling  
43 (Pinardi et al., 2003; Barth et al., 2008; Mason et al., 2010; Halliwell et al.,  
44 2011; Herzfeld and Andrewartha, 2012). Studies of ocean responses to atmo-  
45 spheric forcing also highlighted the need of incorporating synoptic scales and  
46 dynamics from the beginning (Falkovich et al., 2005; Halliwell et al., 2008,  
47 2011). Here we incorporate the synoptic scales and dynamics by creating  
48 dynamically balanced initializations for *multiply-connected domains*.

49 Our approach is to efficiently estimate three-dimensional (3D) initial ve-  
50 locity fields that are consistent with the synoptic observations available, com-  
51 plex geometry, free-surface PEs and any other relevant information by defin-  
52 ing and semi-analytically solving a global constrained optimization problem.  
53 By consistent initial velocity fields, we signify fields that would evolve in  
54 accord with the free-surface PE dynamics in the complex region, simulat-  
55 ing the evolution of these ocean processes without spurious initial transients.  
56 By “semi-analytically” solving an optimization problem, we mean that we  
57 analytically derive the Euler-Lagrange equations that optimize the cost func-  
58 tion and then solve these equations numerically. Our approach is in contrast  
59 with procedures that attempt to build flows from scratch solely through  
60 model dynamical adjustment, i.e. through time-integration of a numerical  
61 model. However, our aim is not to replace the estimation of ICs by weak-  
62 or strong- constraint generalized inversions over time (Bennett, 1992, 2002;  
63 Moore, 1991; Moore et al., 2004, 2011). Instead, it is to rapidly compute  
64 ICs that are consistent. They can then lead to useful predictions or be em-  
65 ployed as starting conditions in a generalized inversion, solvable with a few  
66 iterations.

67 Some key technical questions arise due to the complex geometries and  
68 multiscale flows. They include: how to account for multiple islands, tortuous  
69 coastlines and variable bathymetries, respecting boundary conditions?, how  
70 to compute the minimum vertical ocean area between islands?, how to utilize  
71 these areas to set through-flows or local currents within (or near) expected  
72 values?, how to optimize the kinetic energy locally, eliminating unrealistic  
73 hot-spots?, how to ensure conservative 3D flow fields that satisfy continuity  
74 constraints with a free ocean surface?, and finally, how to respect a suffi-  
75 ciently accurate internal dynamics in accord with the observations available

76 and the scales being modeled? To address such questions, we introduce a  
77 subtidal/tidal separation of velocities and obtain first-guess subtidal velocity  
78 fields from reduced dynamics and hydrographic and flow data. Our optimiza-  
79 tion then best-fits these first-guess subtidal velocity fields, enforcing tortuous  
80 coastline, bathymetry and divergence strong constraints. To enforce all of  
81 these constraints, cost functions are defined and Euler-Lagrange equations  
82 that optimize these cost functions are derived and numerically solved. Novel  
83 elements of this methodology include: the incorporation of weighting func-  
84 tions in the cost functions; derivation of the optimal Dirichlet open boundary  
85 conditions (OBCs); and the optimization of the inter-island transports and  
86 near island flows, which provides important velocity corrections in complex  
87 archipelagos. To set the weights for the horizontal streamfunctions along  
88 island coastlines, the minimum distance and vertical area between pairs of  
89 islands are computed using a Fast Marching Method (FMM; Sethian, 1996,  
90 1999). The use of all available information to optimally estimate the inter-  
91 island transports makes our methodology a generalization of the “island rule”  
92 (Godfrey, 1989). Our methodology can also incorporate estimates from the  
93 “island rule” as weak constraints.

94 *Problem Statement and Rationale.* Mathematically, denoting the PE state  
95 variable fields as: temperature  $T$ ; salinity  $S$ ; horizontal and vertical compo-  
96 nents of velocity  $\vec{u}$  and  $w$ ; and free-surface elevation  $\eta$ , our objective is to: i)  
97 obtain initial fields that optimize a constrained cost function  $J$  in a complex  
98 domain,  $\mathcal{D}$ , with boundary  $\partial\mathcal{D}$  (open boundaries and coastlines) i.e.,

$$\arg \min_{[\vec{u}, w, \eta, T, S]} J(\text{data, complex geometry, dynamics}) \quad \text{in } \mathcal{D} \cup \partial\mathcal{D};$$

99 but also ii) determine such a cost function  $J$  and corresponding direct solution  
100 scheme that will efficiently compute consistent initial velocity fields.

101 Of course, there are uncertainties even in the form of the cost function,  
102 the constraints and their parameters (Lermusiaux, 2007). We thus seek to  
103 respect the synoptic data, complex geometry, scales and dynamics (or repre-  
104 sentative reduced dynamics) only within uncertainties. In other words, the  
105 objective is to derive an efficient scheme that computes ICs close enough  
106 to the ocean state at the initial time, so as to subsequently evolve without  
107 spurious transients due to complex bathymetry and islands (geometry), and  
108 also without the possible assimilation shocks. As a result, we aim to avoid  
109 creating initial velocities solely via a model “dynamical adjustment” from

110 too inaccurate first-guesses (e.g. either too large or too small velocities, as  
111 in the extreme case of a model “spin-up” from zero velocities). To illustrate  
112 issues with such adjustments, consider first the case where  $T/S$  remain fixed  
113 while  $\vec{u}$ ,  $w$  and  $\eta$  are adjusted from a too inaccurate first-guess. Model errors  
114 (discretization and other error modes) can grow in the velocity fields during  
115 the adjustment. Also, due to nonlinear terms in the free-surface PEs, even if  
116 the  $T/S$  fields are perfect, the velocity adjustment may either not converge  
117 or converge but not towards the true velocity everywhere in the complex do-  
118 main. Second, if a first-guess velocity far from the truth is instead adjusted  
119 by allowing  $T$  and  $S$  to vary during the adjustment, then potential energy and  
120 kinetic energy would be inter-changed. The resulting adjusted density and  
121 velocity fields would differ from the true ones, e.g. be in a different energy  
122 balance or “attractor regime” than the real one. Critically, such adjusted  
123 fields retain some memory of the too erroneous first-guess velocity. Model  
124 predictions from these fields would then be damaged for some time. All of  
125 these considerations due to complex geometries are exemplified in §4.1-§4.2.  
126 Only data assimilation (DA), i.e. re-initialization, could correct these biases.

127 In what follows, we present our methodology for ICs in complex domains  
128 (§2). In §3, we derive the core algorithms to optimally fit velocities and trans-  
129 ports (§3.1) and to optimize them between and near islands (§3.2). In §4, we  
130 apply our methodology around the Hawaiian islands of Kauai/Niihau (§4.1),  
131 in the Taiwan/Kuroshio region (§4.2) and in the Philippines Archipelago  
132 (§4.3). Quantitative comparisons (i) with other commonly-used initialization  
133 strategies, (ii) among hindcasts from these ICs and (iii) with independent *in*  
134 *situ* observations, show that our complex-domain optimization corrects ve-  
135 locity estimates and incorporates critical constraints on the net transports,  
136 all of which lead to more accurate forecasts in multiply-connected regions.  
137 These are coastal mesoscale examples but our methodology is applicable to  
138 other scales. A summary and conclusions are in §?? The free-surface PEs and  
139 our modeling system are outlined in App. A. Specifics of the methodology,  
140 including some details of the derivations, are in Apps. B–D.

## 141 **2. Methodology: Overall Scheme**

142 In this section we present a high-level description of our methodology for  
143 constructing PE-balanced initialization fields in complex domains, including  
144 nesting and downscaling. The steps are outlined in §2.1-2.3 and summarized  
145 in table 1. Implicit in these steps is a separation of the subtidal and tidal

146 velocities/ transports (§2.3). These steps provide the context within which we  
 147 derive our core algorithms of §3 for the subtidal velocities/ transports. These  
 148 core algorithms solve a weighted least squares optimization by obtaining the  
 149 exact solutions to Euler-Lagrange equations for streamfunction formulations  
 150 of subtidal velocity/ transport. The specific equations solved are: (i) a 1D  
 151 Poisson equation along the external boundary for the Dirichlet OBCs, (ii)  
 152 algebraic equations for the constant values for the streamfunction along the  
 153 uncertain islands which optimize the inter-island transports and near-island  
 154 flows and (iii) a Poisson equation for a streamfunction formulation of the  
 155 velocity/ transport, using the BCs from (i) & (ii). Since we focus on velocity  
 156 optimization, we omit a discussion on input data, models, etc., which we  
 157 provide in Haley et al. (2014).

### 158 2.1. First-guess velocity

159 We start by estimating first-guess velocity fields,  $\vec{u}_{(0)}$  and  $w_{(0)}$ , that are in  
 160 dynamical balance among each other and with the  $T/S$  fields, represent the  
 161 specific scales of interest, and satisfy simple bathymetric constraints. These  
 162  $\vec{u}_{(0)}$  and  $w_{(0)}$  are the starting point for adding more complicated coastal,  
 163 bathymetric and transport constraints. The subscript ( $n$ ) represents the  $n^{\text{th}}$ -  
 164 correction of a quantity, hence  $\vec{u}_{(0)}$  is the first guess velocity,  $\vec{u}_{(1)}$  is the first  
 165 correction velocity and so on.

166 Reduced-dynamics models are often used in conjunction with mapped  
 167  $T/S$  fields as the starting point for constructing  $\vec{u}_{(0)}$  and  $w_{(0)}$ . A commonly  
 168 used reduced model is geostrophy, specifically integrating the thermal wind  
 169 equations (Wunsch, 1996; Marshall and Plumb, 2008; Haley et al., 2014). The  
 170  $\vec{u}_{(0)}$  and  $w_{(0)}$  can also combine: additional dynamics (e.g. Ekman dynamics  
 171 and other boundary layers); velocity feature models and data (*in situ* and  
 172 remote). When available, prior knowledge of the flow (e.g. net transports,  
 173 velocity values or throughflow range) should be used to constrain estimates.  
 174 All of these combinations should properly account for the uncertainties in  
 175 the data and estimates. Examples are shown in §4.

176 One can use the velocity fields from existing numerical simulations (often  
 177 at coarser resolutions). We treat these as first-guess velocities because they  
 178 usually do not fit all of our dynamics, scales and resolution. One simple  
 179 constraint we directly impose on  $\vec{u}_{(0)}$  is to set the velocities to zero under the  
 180 model bathymetry (this can require care, see Haley et al., 2014).

181 *2.2. Complex geometry constraints*

182 The first guess velocities  $\vec{u}_{(0)}$  do not respect all model geometry con-  
183 straints nor the bottom-related dynamics. Geostrophic velocities rarely sat-  
184 isfy no-normal flow through coastlines and bottom balances. Velocities ob-  
185 tained from other simulations are in balance with their own bathymetry and  
186 coasts, which, in our applications, are usually of coarser resolution. Reduced  
187 dynamics models and feature models may or may not take either bathymetry  
188 or coasts into account. Therefore the next step in our scheme is to adjust  
189 the first guess velocities to the modeled bathymetry and coasts.

190 *Coastal constraints.* We first discuss imposing constraints on  $\vec{u}_{(0)}$  defined  
191 on constant-depth levels (which can then be interpolated to other vertical  
192 coordinates). No-normal flow into coasts is imposed on levels which reach the  
193 coasts in water and on any additional levels used in subsequent interpolations.  
194 For all levels below these, no additional constraints are enforced.

195 The method to enforce no-normal flow into coastlines employs a con-  
196 strained least squares minimization to find the first correction velocity,  $\vec{u}_{(1)}$ ,  
197 which at all depths/levels best fits the first-guess,  $\vec{u}_{(0)}$ , while satisfying  $\vec{u}_{(1)} \cdot \hat{n}|_{\partial\mathcal{D}} =$   
198 0. This optimum is obtained by solving 2D elliptical problems exactly in one  
199 iteration. The algorithm is derived later in §3 to allow for a unified presen-  
200 tation of both the flow and transport constraints.

201 For terrain-following vertical coordinates, the no-normal flow constraint  
202 is imposed on velocities at constant-depth levels and the results are interpo-  
203 lated to terrain-following. For isopycnal or generalized coordinates (HL10),  
204 the situation is similar to the constant-depth vertical coordinates and the  
205 optimization is applied for layers/levels reaching the coasts.

206 Below the levels where we impose no-normal flow into coasts, we could  
207 use the above optimization to force the very bottom flows to be aligned with  
208 isobaths. However, this is only done when we have strong physical evidence  
209 for such isobaths-aligned bottom flows (see Haley et al., 2014).

210 *3D effects and more complicated bathymetry constraints.* When the full 3D  
211 flow dynamics is critical, we update the algorithm outlined above into a 3D  
212 (x,y,z) best fit. One example is the initialization from an existing numerical  
213 simulation (i.e. downscaling). These fields are in their own 3D dynamical  
214 balance and are assumed to be sufficiently resolved to contain a useful  $w_{(0)}$   
215 at the new, refined, resolution. The goal is then to maintain as much of this  
216 3D balance as is consistent with the model being initialized. Other examples

217 (see Haley et al., 2014) involve the use of 3D feature models or reduced 3D  
 218 dynamics (e.g. geostrophy and Ekman forcing).

219 In appendix B, we derive a predictor-corrector algorithm for fitting the  
 220 no-normal flow constraints in 3D, including vertical velocity  $w$  information.  
 221 The result of this algorithm is the second correction velocity,  $\vec{u}_{(2)} = \vec{u}_{(1)} + \Delta\vec{u}$ ,  
 222 that recovers the first guess vertical velocity by imposing the constraint  $\nabla \cdot$   
 223  $\vec{u}_{(2)} \approx -\frac{\partial w_{(0)}}{\partial z}$ , where  $\nabla \cdot$  is the horizontal divergence operator. Without this  
 224 optimized correction, the above level-by-level 2D streamfunction formulation  
 225 loses the information on  $w$ .

226 *First-guess sub-tidal transport.* Once the geometry-constrained  $\vec{u}_{(1)}$  (or  $\vec{u}_{(2)}$ )  
 227 is computed, it is used to obtain the first-guess transport,  $H\vec{U}_{(0)}$ , from either

$$H\vec{U}_{(0)} = \begin{cases} \int_{-H}^0 \vec{u}_{(2)} dz & \text{if 3D constraints (see App. B)} \\ \text{or } \int_{-H}^0 \vec{u}_{(1)} dz & \text{otherwise} \end{cases} \quad (1)$$

228 where  $\vec{U}$  is the local total-depth-averaged velocity and  $H(x, y)$  the local total  
 229 depth of the water column. In §2.3 our optimization starts from  $H\vec{U}_{(0)}$  over  
 230  $\mathcal{D}$  and imposes additional (strong) transport constraints, leading to the first  
 231 correction transport estimate,  $H\vec{U}_{(1)}$  over  $\mathcal{D}$ .

### 232 2.3. Sub-tidal transport constraints

233 The final constraint on velocity in complex domains is applied on the  
 234 divergence of the horizontal transport. From eq. (A.7), this  $\nabla \cdot (H\vec{U})$  is  
 235 directly related to  $\frac{\partial \eta}{\partial t}$ . We consider separately the portions of the transport  
 236 with significant contributions to  $\frac{\partial \eta}{\partial t}$  and those with negligible contributions.

237 This rate  $\frac{\partial \eta}{\partial t}$  is a function of both external processes (tides, evaporation  
 238 - precipitation, rivers, open boundaries) and local processes (e.g. density  
 239 driven flows). Generally only tides produce significant contributions to  $\frac{\partial \eta}{\partial t}$   
 240 (i.e. barring floods and other catastrophic events, the remaining processes ei-  
 241 ther have time scales which are too slow or amplitudes which are too small).  
 242 We compute the portions of the initial transport with negligible contributions  
 243 to  $\frac{\partial \eta}{\partial t}$ , i.e. the non-divergent sub-tidal transport, and superimpose tidal eleva-  
 244 tions and transports from the tidal fields that will force the simulation being  
 245 initialized. The result is initial and boundary transports with dynamically-  
 246 balanced divergences. During the construction of the transports, the con-  
 247 straint of no-normal flow into the complex coastlines is re-imposed to ensure  
 248 that both it and the desired divergence are maintained in the final solution.



249 A constrained optimization is employed to find the non-divergent sub-  
 250 tidal transport,  $H\vec{U}_{(1)}$ , that best fits  $H\vec{U}_{(0)}$  subject to the constraints of no-  
 251 normal flow at the complex coasts, i.e.  $\vec{U} \cdot \hat{n} \Big|_{\partial\mathcal{D}} = 0$ , and of non-divergence,  
 252 i.e.  $\nabla \cdot (H\vec{U}_{(1)}) = 0$ . This procedure, essentially the same as that for imposing  
 253 no-normal flow on the velocities, ensures that the final 3D velocities will  
 254 maintain no-normal flow into coasts and is derived in §3.

255 *Free surface and tidal initialization.* The final steps in the algorithm ensure  
 256 the consistency amongst the initial transports, initial free surface and tidal  
 257 forcing. This material was largely presented in HL10 and is summarized in  
 258 app. C in the notation of the present manuscript.

### 259 3. Methodology: Core Algorithms

260 We now derive the core algorithms for our constrained optimization of  
 261 the initial velocities and transports in complex domains. Our semi-analytical  
 262 methodology (summarized in table 2) starts by a global weighted optimiza-  
 263 tion of the open boundary values to the first guess and geometric and di-  
 264 vergence constraints, in the absence of islands. We employ these optimized  
 265 values and certain island conditions in a best fit of velocities and transports  
 266 (subject to the same constraints). From this solution, we obtain initial es-  
 267 timates for minimum transports between each island and all other coasts.  
 268 With these estimates and the best-fit OBC values, we solve our constrained  
 269 weighted optimization of the initial velocities and transports in the presence  
 270 of islands. Weighting functions are defined using uncertainty and physics  
 271 considerations. To obtain the exact solutions for these best fits, we derive  
 272 successive Euler-Lagrange equations for the interior, boundary and island  
 273 streamfunctions. This is done next for the case of fitting transports, adding  
 274 notes when needed for fitting 3D velocities.

#### 275 3.1. Core algorithm to optimize sub-tidal transports and velocities

276 The algorithm employs a least squares minimization to find the sub-tidal  
 277  $H\vec{U}_{(1)}$  that best fits the first guess  $H\vec{U}_{(0)}$  (eq. 1) under the geometric and  
 278 divergence constraints with a specific focus on no-normal flow in complex  
 279 geometries. To obtain the exact solutions for these optimizations, we derive  
 280 (i) a Poisson equation (eq. 5) in  $\mathcal{D}$  for a streamfunction representation of  
 281 the transport or velocity, i.e.  $\Psi$  for  $H\vec{U}_{(1)}$  or  $\psi$  for  $\vec{u}_{(1)}$  and (ii) a 1D Poisson

282 equation (eq. 10) along the external boundary,  $\partial\mathcal{D}^e$ , for the Dirichlet OBCs,  
 283  $\Psi_{b^e}$  or  $\psi_{b^e}$ , which best fit the flow through the open boundaries. Specifically,  
 284 the weighted least squares cost function,  $J$ , is defined as

$$\begin{aligned}
 J(H\vec{U}_{(1)}) &= \frac{1}{2} \iint_{\mathcal{D}} \omega \left\| H\vec{U}_{(0)} - H\vec{U}_{(1)} \right\|^2 da \\
 \text{subject to } \nabla \cdot (H\vec{U}_{(1)}) &= 0 \quad (\text{non-divergence}), \\
 \vec{U}_{(1)} \cdot \hat{n} \Big|_{\partial\mathcal{D}} &= 0 \quad (\text{no-normal flow into coasts}),
 \end{aligned} \tag{2}$$

285 where  $H\vec{U}_{(1)}$  is any test transport,  $\omega(x, y)$  a positive definite weighting func-  
 286 tion and  $da$  an area element over domain  $\mathcal{D}$ . This could be formulated as a  
 287 constrained minimization problem, with an operation count of  $O(N_{iter}N_xN_yN_z)$   
 288 (accounting for sparsity). We instead reformulate eq. (2) in terms of 2-3 lin-  
 289 ear PDEs over  $\mathcal{D}$ , each with  $O(N_xN_y(N_z + 1))$  operations, and a linear PDE  
 290 over  $\partial\mathcal{D}$  with  $O((N_x + N_y)(N_z + 1))$  operations (in our cases,  $N_z$  is  $O(100)$ ).

291 The first non-divergence constraint is imposed by replacing  $H\vec{U}_{(1)}$  in eq.  
 292 (2) using a test transport streamfunction,  $\tilde{\Psi}$ , formulation defined as

$$H\vec{U}_{(1)} = \hat{k} \times \nabla\tilde{\Psi} \tag{3}$$

293 where  $\hat{k}$  the unit vector in the vertical. For 3D velocities, one has the choice  
 294 of either working with layer-by-layer transports or directly with level-by-  
 295 level velocities. If one chooses layer transports, then the only change to eq.  
 296 (3) (and in subsequent equations and weighting functions) is that  $H(x, y)$  is  
 297 the (variable) layer thickness, not the total water depth. If one optimizes  
 298 level-by-level velocities, then level-by-level test velocity streamfunctions are  
 299 defined,

$$\vec{u}_{(1)} = \hat{k} \times \nabla\tilde{\psi} \quad . \tag{4}$$

300 This imposes a horizontal non-divergence on  $\vec{u}_{(1)}$ . For cases in which  $\nabla \cdot \vec{u}_{(0)}$   
 301 is important, a corrector to recover this divergence is obtained in App. B.

302 In App. D.1, we obtain, via the calculus of variations, the following PDE  
 303 for the  $\Psi$  that minimizes  $J$  for a given set of imposed BCs,  $\Psi_b$  (to be derived):

$$\begin{aligned}
 \nabla \cdot (\omega \nabla \Psi) &= \left[ \nabla \times \left( \omega H\vec{U}_{(0)} \right) \right] \cdot \hat{k} \\
 \Psi|_{\partial\mathcal{D}} &= \Psi_b \quad .
 \end{aligned} \tag{5}$$

304 Equation (5) without the weighting function,  $\omega$ , is fairly standard and usually  
 305 obtained via the Helmholtz decomposition of a vector into nondivergent and  
 306 irrotational components (e.g., Lynch, 1989; Denaro, 2003; Li et al., 2006).  
 307 The weighting function  $\omega(x, y)$  can be decomposed into the product of a  
 308 weight based on the uncertainty in  $H\vec{U}_{(0)}$  and a physically-based weight.  
 309 Two intuitive choices for the physically-based weight are:  $\omega = 1$ , i.e. eq. (2)  
 310 minimizes the difference in the transports, and  $\omega = \frac{1}{H^2}$ , i.e. eq. (2) minimizes  
 311 the difference in the velocities. In practice, while these two choices give over-  
 312 all similar results, minimizing the difference in transports ( $\omega = 1$ ) tends to  
 313 allow larger velocities. This can exacerbate problems with over-estimating  
 314 the barotropic velocity in isolated channels in complex archipelagos, hence  
 315  $\omega = \frac{1}{H^2}$  (minimizing the velocity differences) is the preferred choice. Other  
 316 choices could be explored, e.g.  $\omega = \left\| H\vec{U}_{(0)} \right\|^{-2}$ , minimizing relative velocity,  
 317 or  $\omega = \|\nabla H\|^{-2}$ , reducing weights over steep bathymetry where  $H\vec{U}_{(0)}$  may  
 318 be less accurate. When working with velocity streamfunctions,  $\psi$ ,  $\omega = 1$   
 319 provides the velocity best fit and  $\omega = \|\vec{u}_{(0)}\|^{-2}$  provides the relative velocity  
 320 best fit. When implementing eq. (5) for  $\psi$ , we often impose it at all verti-  
 321 cal levels to ensure interpolations with global vertical stencils (e.g. splines)  
 322 maintain no-normal flow.

323 *Boundary Conditions.* Before eq. (5) can be solved for  $\Psi$ , the Dirichlet  
 324 boundary values  $\Psi_b$  need to be optimized. Here, we derive a system of equa-  
 325 tions to obtain the best-fit Dirichlet conditions along the open boundaries  
 326 and complex “external coasts”, coastlines which intersect the boundary of the  
 327 computational domain. The external coasts and open boundaries are grouped  
 328 together to form the exterior boundary,  $\partial\mathcal{D}^e \subset \partial\mathcal{D}$ , of the complex domain.  
 329 This scheme assumes that the boundary values of  $\vec{U}_{(0)}$  are known with equal  
 330 confidence to the interior values, which is appropriate when downscaling or  
 331 when the coverage (data or feature model) extends to the boundaries. For  
 332 other cases, we derive a scheme to first extend the interior velocity informa-  
 333 tion to the boundaries, and then use them in the present scheme. Obtaining  
 334 boundary values for “islands” (landforms fully contained in the interior of  
 335  $\mathcal{D}$ ) is discussed in §3.2.

336 Since  $H\vec{U}_{(0)}$  does not respect the divergence or coastal constraints even  
 337 at the boundary (e.g. no net transport), we need best-fit boundary values  
 338 which do. The cost function,  $J_{be}$ , defined on  $\partial\mathcal{D}^e$  which optimizes candidate

339 Dirichlet BCs,  $\tilde{\Psi}_{b^e}$ , to best-fit the normal transport provided by  $H\vec{U}_{(0)}$  is:

$$\begin{aligned}
J_{b^e}(H\vec{U}_{b^e}) &= \frac{1}{2} \oint_{\partial\mathcal{D}^e} \omega \left[ \left( H\vec{U}_{(0)} - H\vec{U}_{b^e} \right) \cdot \hat{n} \right]^2 ds \\
\Leftrightarrow J_{b^e}(\tilde{\Psi}_{b^e}) &= \frac{1}{2} \oint_{\partial\mathcal{D}^e} \omega \left( \frac{\partial\tilde{\Psi}_{b^e}}{\partial s} + H\vec{U}_{(0)} \cdot \hat{n} \right)^2 ds \quad (6)
\end{aligned}$$

340 where  $\omega$  is the same weighting function as used in eqs. (2-5),  $H\vec{U}_{b^e}$  are the  
341 candidate boundary transports corresponding to  $\tilde{\Psi}_{b^e}$ , and  $s$  is the tangential  
342 coordinate to the boundary in the counter-clockwise direction.

343 Employing calculus of variations (App. D.2), we obtain a PDE along the  
344 open segments for the  $\Psi_{b^e}$  that minimizes  $J_{b^e}$

$$-\frac{\partial}{\partial s} \left( \omega \frac{\partial\Psi_{b^e}}{\partial s} \right) = \frac{\partial}{\partial s} \left( \omega H\vec{U}_{(0)} \cdot \hat{n} \right) \quad (7)$$

345 along with the jump conditions at the coastal endpoints

$$-\left[ \omega \left( \frac{\partial\Psi_{b^e}}{\partial s} + H\vec{U}_{(0)} \cdot \hat{n} \right) \right] \Big|_{C_m^{e-}}^{C_m^{e+}} = 0 \quad (8)$$

346 where  $C_m^{e+}$  is the end of coast  $m$  (traversing the coast counter-clockwise) and  
347  $C_m^{e-}$  is the beginning, see Fig. 1. To ensure no-normal flow (i.e.  $\Psi_{b^e}$  constant  
348 along  $C_m^e$ ), we append the following condition

$$\Psi_{b^e} \Big|_{C_m^{e-}}^{C_m^{e+}} = 0 \quad . \quad (9)$$

349 Physically, eq. (8) equalizes the mismatch (weighted by  $\omega$ ) between  $H\vec{U}_{(0)} \cdot \hat{n}$   
350 and  $H\vec{U}_{(1)} \cdot \hat{n} = -\frac{\partial\Psi_{b^e}}{\partial s}$  at both ends of a coast (i.e. between open boundary  
351 segments), while eq. (7) equilibrates the variations in the mismatch along  
352 the open boundary segments. Enforcing both (7) and (8) thus penalizes the  
353 mismatch along all boundaries. Note that if one integrates (7) along coast  
354  $m$  instead of an open segment (where (7) applies), one recovers (8).

355 Known transport information (most often in the form of a net transport  
356 between coasts) can also be included, taking advantage of the additive inde-  
357 terminacy in  $\Psi$ . To do this, we identify the set of coasts,  $\{C_k^e\}$ , along which  
358 the values for the transport streamfunction,  $\{\Psi_{C_k^e}\}$  are known and directly

359 impose these values. As an example, consider the domain of Fig. 1 and as-  
 360 sume that the literature reports a net 1 Sv southeast transport between  $C_1^e$   
 361 and  $C_2^e$ . We can arbitrarily pick two values for these coasts whose difference  
 362 is equal to the net transport (e.g.  $\Psi_{C_1^e} = 0$  and  $\Psi_{C_2^e} = 1$  Sv) and include  
 363 those two identity equations to impose this net transport. The final, general,  
 364 system for finding the Dirichlet boundary values (separating the unknowns  
 365 on the left-hand side from the knowns on the right) is

$$\begin{aligned}
 -\frac{\partial}{\partial s} \left( \omega \frac{\partial \Psi_{be}}{\partial s} \right) &= \frac{\partial}{\partial s} \left( \omega H \vec{U}_{(0)} \cdot \hat{n} \right) && \text{along open boundaries} \\
 - \left( \omega \frac{\partial \Psi_{be}}{\partial s} \right) \Big|_{C_m^{e-}}^{C_m^{e+}} &= \left( \omega H \vec{U}_{(0)} \cdot \hat{n} \right) \Big|_{C_m^{e-}}^{C_m^{e+}} && \text{at unknown coasts } \{C_m^e\} \\
 \Psi_{be} \Big|_{C_m^{e-}}^{C_m^{e+}} &= 0 && \text{at unknown coasts } \{C_m^e\} \\
 \Psi_{be} \Big|_{C_k^e} &= \Psi_{C_k^e} && \text{at known coasts } \{C_k^e\}
 \end{aligned} \tag{10}$$

366 After eqs. (10) are solved, the values for  $\Psi_{be}$  found at the ends of the unknown  
 367 coasts,  $C_m^{e\pm}$ , are applied all along their respective coasts,  $C_m^e$ . For velocity  
 368 streamfunctions, replace  $(\Psi, \Psi_{be})$  with  $(\psi, \psi_{be})$  and  $H\vec{U}_{(0)}$  with  $\vec{u}_{(0)}$  in eqs.  
 369 (5) and (10). The algorithm and its equations are summarized in table 2.

370 *Propagating interior information to the boundaries.* Here we give the solution  
 371 in which  $\vec{U}_{(0)}$  in the interior of the complex domain, or in part of it, is known  
 372 with a higher degree of confidence than  $\vec{U}_{(0)}$  along the open boundary. Hence  
 373 we propagate the interior information to the boundary prior to solving eq.  
 374 (10). The basic idea is to use a modified version of the best-fit eq. (5) to  
 375 perform the propagation. There are two modifications. The first modifies  $\mathcal{D}$   
 376 by removing all but a single coast,  $C^{1\text{cst}}$ , (i.e. we transform the remaining  
 377 land points into shallow ocean points and take advantage of the fact that  
 378  $\vec{U}_{(0)} = 0$  under all land and coasts). Along this single coast we are free  
 379 to impose any constant,  $\Psi_{C^{1\text{cst}}}$ . The second modification is to replace the  
 380 Dirichlet OBCs by either the Neumann OBCs derived in App. D.1 or by a  
 381 combination of weaker free-OBCs with  $\omega$  identically zero at the boundary (to  
 382 maintain a best-fit solution, App. D.1). Finally, the function  $\omega(x, y)$  needs  
 383 to be small (e.g. based on uncertainty) near the open boundaries. This gives:

$$\begin{aligned}
 \nabla \cdot (\omega \nabla \Psi_{(-1)}) &= \left[ \nabla \times \left( \omega H \vec{U}_{(0)} \right) \right] \cdot \hat{k} \\
 \Psi_{(-1)} \Big|_{C^{1\text{cst}}} &= \Psi_{C^{1\text{cst}}}
 \end{aligned} \tag{11}$$

and either

$$\nabla \Psi_{(-1)} \cdot \hat{n} \Big|_{\partial \mathcal{D}} = -\hat{k} \times H \vec{U}_{(0)} \cdot \hat{n} \Big|_{\partial \mathcal{D}}$$

or

$$\omega \Big|_{\partial \mathcal{D}} = 0 \quad \& \quad \text{e.g.} \quad \frac{\partial H U \cdot \hat{n}}{\partial n} \Big|_{\partial \mathcal{D}} = \frac{\partial^2 \Psi_{(-1)}}{\partial n \partial t} \Big|_{\partial \mathcal{D}} = 0$$

384 We then recompute  $\vec{U}_{(0)}$  from the  $\Psi_{(-1)}$  and use this new  $\vec{U}_{(0)}$  in eq. (10). For  
385 velocity streamfunctions, replace  $\Psi_{(-1)}$  by  $\psi_{(-1)}$  and  $H \vec{U}_{(0)}$  by  $\vec{u}_{(0)}$ .

386 *Nesting Considerations.* When preparing initializations for nested domains  
387 with complex multiply-connected geometries, a key consideration is consis-  
388 tency between the fields in coarser and finer grids. To ensure this consistency,  
389 we by-pass eq. (10) for the fine grid, and instead interpolate the coarse-  
390 domain  $\Psi$  to obtain the fine domain  $\Psi_{be}$ . This is illustrated in §4.3.3 where  
391 we explore options for the fine-domain islands.

392 *3.2. Core algorithm to optimize sub-tidal transports between islands and ve-*  
393 *locities near islands*

394 To obtain the Dirichlet values along islands ( $\Psi_{Ci}$ ), either transport esti-  
395 mates from additional sources (e.g. estimates in the literature) are used or  
396 a scheme is required to construct the necessary constant values from  $\vec{U}_{(0)}$ .  
397 Care is needed to ensure that the selected constant values do not produce  
398 unrealistic velocities, especially in multiply-connected archipelagos. Here we  
399 derive a system of algebraic equations (eq. 15) for the optimized constant  
400 values of the streamfunction along islands that were uncertain,  $\Psi_{Ciu}$  or  $\psi_{Ciu}$ ,  
401 a common situation in complex domains.

402 *“Certain coast” Solution.* In order to obtain a first estimate for the unknown  
403 transports between islands and other coasts, we best-fit transports and ve-  
404 locities in the absence of islands (i.e. we transform the islands into ocean  
405 points). We begin by separating  $\partial \mathcal{D}$  into certain,  $\partial \mathcal{D}^c$ , and uncertain,  $\partial \mathcal{D}^{iu}$ ,  
406 segments.  $\partial \mathcal{D}^c$  will be comprised of  $\partial \mathcal{D}^e$ , the solved external boundaries (eq.  
407 10), and of  $\partial \mathcal{D}^{ic}$ , islands  $C_k^{ic}$  along which we have streamfunction values,  
408  $\Psi_{C_k^{ic}}$ , we wish to impose (e.g. a literature estimate for the transport between  
409  $C_k^{ic}$  and  $C_m^e$  added to the previously obtained  $\Psi_{be}$  along  $C_m^e$ ). We solve for  
410 the “certain coast solution”,  $\Psi_{(0)}$ , over  $\mathcal{D}$  using the PDE

$$\nabla \cdot (\omega \nabla \Psi_{(0)}) = \left[ \nabla \times \left( \omega H \vec{U}_{(0)} \right) \right] \cdot \hat{k} \quad (12)$$

$$\Psi_{(0)}|_{\partial\mathcal{D}^c} = \Psi_{b^c} \equiv \begin{cases} \Psi_{b^e} & \text{if } s \in \partial\mathcal{D}^e \\ \Psi_{C_k^{ic}} & \text{if } s \in C_k^{ic} \end{cases}$$

411 (table 2). Note that  $\Psi_{(0)}$  is not constrained to satisfy no-normal flow along  
 412 the uncertain islands.  $\Psi_{(0)}$  contains useful information from the data and  
 413 dynamics that went into  $\vec{U}_{(0)}$  (e.g. the position of major currents relative to  
 414 the various coastlines, the effects of bathymetry on the flow) which will be  
 415 used to determine the appropriate constant  $\Psi_{C^{iu}}$  along the uncertain coasts.  
 416 These  $\Psi_{C^{iu}}$  will be used along with  $(\Psi_{b^e}, \Psi_{C_k^{ic}})$  to complete the set of all BCs  
 417  $\Psi_b$ . Eq. (5) can then be solved to construct the final  $\Psi$ . We next define  
 418 two methods for determining  $\Psi_{C^{iu}}$ : averaging and weighted Least Squares  
 419 optimization.

420 *Averaging.* The first simpler method we define is to average  $\Psi_{(0)}$  along each  
 421  $C_k^{iu}$  and use those averages for  $\Psi_b$  in eq. (5) as

$$\Psi_b = \begin{cases} \Psi_{b^e} & \text{if } s \in \partial\mathcal{D}^e \\ \Psi_{C_k^{ic}} & \text{if } s \in C_k^{ic} \\ \frac{\oint_{C_k^{iu}} \Psi_{(0)} ds}{\oint_{C_k^{iu}} ds} & \text{if } s \in C_k^{iu} \end{cases} \quad (13)$$

422 In practice, we found that this averaging only works if the differences between  
 423 the finally determined  $\Psi$  and  $\Psi_{(0)}$  are localized around each island (i.e. only  
 424 small perturbations introduced at other islands). In general, one can not re-  
 425 quire such localization assumptions. Hence, we derive a new, robust method  
 426 for constructing  $\Psi_{C^{iu}}$ . We compare results using these two methods in §4.

427 *Weighted Least Squares optimization.* The optimization best fits the inter-  
 428 island transports to the minimum inter-island transports as calculated from  
 429  $\Psi_{(0)}$  in order to find  $\Psi_{C^{iu}}$  that produce a balanced and smooth velocity field,  
 430 e.g. with no unrealistically large velocities. In the uncertain straits, the goal  
 431 is to minimize the difference between the minimum net transports between  
 432 islands estimated from  $\Psi_{(0)}$  and the net transports between islands with  $\Psi_{C^{iu}}$   
 433 constant along each island. Alternatively one can minimize the differences  
 434 between the average barotropic velocities between islands from  $\Psi_{(0)}$  and using  
 435  $\Psi_{C^{iu}}$ . In §3.2.1 we show how to compute weights to select between fitting the  
 436 transports or the barotropic velocities. The addition of weak constraints to  
 437 provide additional bounds on the velocity is presented in §3.2.2.

438 We define  $M^c$  as the number of coasts in  $\partial\mathcal{D}^c$  and  $N^{iu}$  as the number of  
 439 coasts in  $\partial\mathcal{D}^{iu}$ . The global optimization functional to find the  $\Psi_{C^{iu}}$  is

$$\begin{aligned}
 J_{bu} \left( \Psi_{C_1^{iu}}, \dots, \Psi_{C_{N^{iu}}^{iu}} \right) &= \frac{1}{2} \sum_{n=1}^{N^{iu}} \sum_{m=n+1}^{N^{iu}} \left[ \varpi_{nm}^{uu} \left( \Psi_{C_n^{iu}} - \Psi_{C_m^{iu}} - \Delta_{nm}^{uu} \Psi_{(0)} \right)^2 \right] \\
 &+ \frac{1}{2} \sum_{n=1}^{N^{iu}} \sum_{k=1}^{M^c} \left[ \varpi_{nk}^{uc} \left( \Psi_{C_n^{iu}} - \Psi_{(0)}(s_{nk}^{uc}) \right)^2 \right] \\
 &+ \frac{1}{2} \sum_{n=1}^{N^{iu}} \left[ \varpi_{nb}^{uo} \left( \Psi_{C_n^{iu}} - \Psi_{(0)}(s_{nb}^{uo}) \right)^2 \right] \quad (14)
 \end{aligned}$$

440 Equation (14) is comprised of three terms: (i) a double summation to opti-  
 441 mize the transport between all pairs of uncertain coasts,  $C^{iu}$ ; (ii) a dou-  
 442 ble summation to optimize the transport between all pairs of uncertain and  
 443 certain coasts,  $C^c$ ; and (iii) a single summation to optimize the transport  
 444 between each of the uncertain coasts and the open boundaries of the com-  
 445 plex domain. These three terms are derived in appendix D.3. Note that the  
 446 physical constraints on this optimization come from  $\Psi_{(0)}$  (e.g. if  $\Psi_{(0)}$  contains  
 447 a strong current between two islands, the minimization target value of the  
 448 first term,  $\Delta_{nm}^{uu} \Psi_{(0)}$ , contains the minimum transport of that current). We  
 449 utilize the superscript notation:  $uu$  for weights and differences between pairs  
 450 of uncertain coasts;  $uc$  between uncertain and certain coasts; and  $uo$  between  
 451 uncertain coasts and the open boundaries. The first double summation in  
 452 eq. (14) measures the weighted ( $\varpi_{nm}^{uu}$ ) difference between the optimized net  
 453 transport,  $\Psi_{C_n^{iu}} - \Psi_{C_m^{iu}}$ , between the pairs of coasts and the minimum net  
 454 transport,  $\Delta_{nm}^{uu} \Psi_{(0)}$ , computed from the certain coast solution,  $\Psi_{(0)}$ . The  
 455 second double summation measures the weighted ( $\varpi_{nk}^{uc}$ ) difference between  
 456 the optimized  $\Psi_{C_n^{iu}}$  and  $\Psi_{(0)}(s_{nk}^{uc})$ , the value of  $\Psi_{(0)}$  along  $C_n^{iu}$  which mini-  
 457 mizes the net transport (estimated by  $\Psi_{(0)}$ ) between  $C_n^{iu}$  and  $C_k^c$ .  $s_{nk}^{uc}$  is the  
 458 point along  $C_n^{iu}$  at which  $\Psi_{(0)}$  attains this value. The final single summa-  
 459 tion measures the weighted ( $\varpi_{nb}^{uo}$ ) difference between the optimized  $\Psi_{C_n^{iu}}$  and  
 460  $\Psi_{(0)}(s_{nb}^{uo})$ , the value of  $\Psi_{(0)}$  along  $C_n^{iu}$  which minimizes the net transport (es-  
 461 timated by  $\Psi_{(0)}$ ) between  $C_n^{iu}$  and  $\partial\mathcal{D}^o$ .  $s_{nb}^{uo}$  is the point along  $C_n^{iu}$  at which  
 462  $\Psi_{(0)}$  attains this value. The first double sum provides the algorithm robust-  
 463 ness to non-localized changes from imposing the  $\Psi_{C^{iu}}$ , while the second two  
 464 provide a pathway for the absolute value of  $\Psi_{be}$  (App. D.3).

465 The least square minimum of  $J_{bu}$  in (14) is computed by setting gradients



466 with respect to  $\Psi_{C_n^{iu}}$ 's equal to zero. The result is given by:

$$\begin{aligned}
& \left[ \sum_{\substack{m=1 \\ m \neq n}}^{N^{iu}} \varpi_{nm}^{uu} + \sum_{k=1}^{M^c} \varpi_{nk}^{uc} + \varpi_{nb}^{uo} \right] \Psi_{C_n^{iu}} - \sum_{\substack{m=1 \\ m \neq n}}^{N^{iu}} \varpi_{nm}^{uu} \Psi_{C_m^{iu}} \\
&= \sum_{\substack{m=1 \\ m \neq n}}^{N^{iu}} \varpi_{nm}^{uu} \Delta_{nm}^{uu} \Psi_{(0)} + \sum_{k=1}^{M^c} \varpi_{nk}^{uc} \Psi_{(0)}(s_{nk}^{uc}) + \varpi_{nb}^{uo} \Psi_{(0)}(s_{nb}^{uo}) \quad (15)
\end{aligned}$$

467 Eq. (15) represents a system of  $N^{iu}$  equations that we solve to obtain the  
468 constant values of transport streamfunction ( $\Psi_{C_n^{iu}}$ ) along the coastlines in  
469  $\partial\mathcal{D}^{iu}$ . These streamfunction values, which smooth the velocity field, are  
470 then included as Dirichlet BCs to then solve (5).

$$\Psi_b = \begin{cases} \Psi_{b^e} & \text{if } s \in \partial\mathcal{D}^e \\ \Psi_{C_k^{ic}} & \text{if } s \in C_k^{ic} \\ \Psi_{C_n^{iu}} & \text{if } s \in C_n^{iu} \end{cases} \quad (16)$$

471 *Imposing additional inter-island transport constraints.* If there exists any ad-  
472 ditional transport information that can be imposed, for example a known  
473 transport  $\Delta_{nm}^{\text{imp}}\Psi$  between a specific pair of islands both in  $\partial\mathcal{D}^{iu}$ , the corre-  
474 sponding  $\Delta_{nm}^{uu}\Psi_{(0)}$  (app. D.3) would be replaced:

$$\Delta_{nm}^{uu}\Psi_{(0)} = \begin{cases} \Delta_{nm}^{\text{imp}}\Psi & \text{if imposing transport} \\ \Psi_{(0)}(s_{nm}^{uu}) - \Psi_{(0)}(s_{mn}^{uu}) & \text{otherwise} \end{cases} \quad (17)$$

475 and the corresponding  $\varpi_{nm}^{uu}$  would be increased to ensure this imposed con-  
476 straint is weighted much more heavily than any of the constraints derived  
477 from  $\Psi_{(0)}$ . This is illustrated in §4.3.2. If the transport being imposed is less  
478 certain, then one would not increase the weight as much (i.e. multiply the  
479 weight needed to enforce  $\Delta_{nm}^{\text{imp}}\Psi$  by an uncertainty-based weight).

### 480 3.2.1. Constructing weights using the Fast Marching Method (FMM)

481 We now discuss the selection of the weighting functions to be used in  
482 eq. (15). As for  $\omega$  (discussion following eq. (5)), we can decompose these  
483 weights into the product of uncertainty-based and physically-based weights.

484 The primary purpose of the physically-based weights is to ensure that the  
485 optimization functional weights the transport differences between adjacent

486 coasts more heavily than those between widely separated coasts. One class  
 487 of such weights can be constructed by using the minimum distance between  
 488 a pair of coasts,  $d_{nm}$ , such as  $\varpi_{nm}^{uu} = (d_{global\ min}/d_{nm})^2$  where the weight  
 489 is nondimensionalized by minimum distance between all pairs of coasts,  
 490  $d_{global\ min}$ . A second class can be obtained by integrating eq. (3) along a  
 491 path,  $S_{nm}$ , between two coasts,  $C_n$  and  $C_m$ , to get

$$\begin{aligned} \int_{S_{nm}} H\vec{U} \cdot \hat{n} dS &= \int_{S_{nm}} \hat{k} \times \nabla\Psi \cdot \hat{n} dS \\ \langle \vec{U} \rangle_{nm} A_{nm} &= \int_{S_{nm}} \frac{\partial\Psi}{\partial S} dS \\ &= \Psi_{C_n} - \Psi_{C_m} \end{aligned} \tag{18}$$

492 where  $\langle \vec{U} \rangle_{nm}$  is the average barotropic velocity along path  $S_{nm}$  and  $A_{nm}$  is  
 493 the cross-sectional area of the ocean along that path. The path between the  
 494 two coasts that corresponds to the minimum cross-sectional area,  $\mathcal{A}_{nm}$ , will  
 495 have the maximum  $\langle \vec{U} \rangle_{nm}$ . Therefore, comparing eqs. (14) and (18), a weight-  
 496 ing function which will lead to minimizing the average barotropic velocity is  
 497  $\varpi_{nm}^{uu} = (\mathcal{A}_{global\ min}/\mathcal{A}_{nm})^2$ , where again  $\varpi_{nm}^{uu}$  is nondimensionalized by the  
 498 minimum  $\mathcal{A}_{nm}$  between all coasts and between all coasts and open bound-  
 499 aries,  $\mathcal{A}_{global\ min}$ . Note: if  $d_{nm}$  is the distance along the shortest path in the  
 500 ocean, then similar arguments can be used to show  $\varpi_{nm}^{uu} = (d_{global\ min}/d_{nm})^2$   
 501 is equivalent to minimizing the transport. The effects of different choices for  
 502 the weights ( $\varpi_{nm}^{uu}$ ,  $\varpi_{nk}^{uc}$  and  $\varpi_{nb}^{uo}$ ) are illustrated in §4.3.1. For the case of ve-  
 503 locity streamfunctions,  $\psi$ , eq. (18) reduces to  $\langle \vec{u} \rangle_{nm} d_{nm} = \psi_{C_n} - \psi_{C_m}$ . Hence  
 504 for  $\psi$ , minimizing the maximum  $\langle \vec{u} \rangle_{nm}$  requires  $\varpi_{nm}^{uu} = (d_{global\ min}/d_{nm})^2$ .

505 To efficiently find the minimum  $\mathcal{A}_{nm}$  among all paths between a pair  
 506 of islands, we employ the FMM (see Agarwal, 2009; Haley et al., 2014).  
 507 This method solves an Eikonal equation for an implicit representation of a  
 508 monotonically expanding front:

$$|\nabla\mathcal{T}(x, y)|\mathcal{F}(x, y) = 1 \tag{19}$$

509 where  $\mathcal{F}(x, y)$  is the scalar speed and  $\mathcal{T}(x, y)$  is the minimum time to reach  
 510 any point in the domain from a given starting point  $(x_0, y_0)$ . To obtain the  
 511 minimum area,  $\mathcal{A}_{nm}$ , or the minimum distance,  $d_{nm}$  we set

$$\mathcal{F}(x, y) = \begin{cases} \frac{1}{H(x, y)} & \text{to find } \mathcal{A}_{nm} \\ 1 & \text{to find } d_{nm} \end{cases}$$

512 and  $\mathcal{T}|_{C_n^i} = 0$  along one island ( $C_n^i$ ). We then solve eq. (19) for  $\mathcal{T}(x, y)$  using  
 513 the FMM. With these choices for speed  $\mathcal{F}$ , the minimum time to reach the  
 514 second island,  $\min(\mathcal{T}|_{C_m^i})$ , is numerically equal to  $\mathcal{A}_{nm}$  or  $d_{nm}$ . Since we  
 515 are only interested in the value of the minimal cross-sectional area and not  
 516 its path, we do not need to perform a back-tracking step to find that path  
 517 (e.g., Lolla et al., 2012, 2014b,a; Lermusiaux et al., 2014).

### 518 3.2.2. Weak bounds on velocity and transport constraints

519 We finally present one optional variation of our algorithm to find the  
 520 inter-island transports: the inclusion of additional weak constraints on the  
 521 barotropic velocity. Focusing on the example of the flow between a pair  
 522 of islands, assume that eq. (15) is being solved using the minimum area  
 523 for the physically-based portion of the weighting. Then, prior to solving  
 524 eq. (15), estimates exist for both the target transport,  $\Delta_{nm}^{uu}\Psi_{(0)}$ , and the  
 525 minimum cross-sectional area,  $\mathcal{A}_{nm}$ , between the islands. Using eq. (18), the  
 526 corresponding average barotropic velocity,  $\langle \vec{U} \rangle_{nm}$  can also be computed. If  
 527 an independent upper bound,  $V_{lim}$ , exists for the mean barotropic velocity  
 528 between the islands (e.g. from literature or a precautionary upper bound),  
 529 then we modify the definition of  $\Delta_{nm}^{uu}\Psi_{(0)}$  (app. D.3) to be

$$\Delta_{nm}^{uu}\Psi_{(0)} = \begin{cases} V_{lim} \mathcal{A}_{nm} \text{sign}(\Psi_{(0)}(s_{nm}^{uu}) - \Psi_{(0)}(s_{mn}^{uu})) & \text{if } |\langle \vec{U} \rangle_{nm}| > V_{lim} \\ \Psi_{(0)}(s_{nm}^{uu}) - \Psi_{(0)}(s_{mn}^{uu}) & \text{otherwise} \end{cases} \quad (20)$$

530 and use this in eq. (15). Eq. (20) is similar to eq. (17). Differences here are  
 531 that (i) we apply weak upper and lower bounds to the velocity but do not  
 532 force a specific transport hence we do not increase the weights and (ii) we ob-  
 533 tain the transport based on the velocity estimates. For the transport between  
 534 islands and external coasts, the same change applies, except that  $\Psi_{(0)}(s_{nk}^{uc})$   
 535 is replaced by  $\Psi_{C_k^c} + V_{lim} \mathcal{A}_{nm} \text{sign}(\Delta_{nk}^{uc}\Psi_{(0)})$  (similarly for the transport be-  
 536 tween islands and the exterior open boundary). The application of these  
 537 bounds is illustrated in §4.3.1. This can be adapted to also provide lower  
 538 bounds for the mean barotropic velocities or directly bound the transports.  
 539 Uncertainty information can also be incorporated into the weights.

## 540 4. Applications

541 In §4.1 we illustrate our core algorithm to optimize sub-tidal velocities  
 542 and transports in complex domains around the Hawaiian islands of Kauai and

543 Niihau. We then compare our core algorithm to the result of an averaging  
 544 method (eq. 13) to obtain the streamfunction values along the uncertain  
 545 islands and to the result of a spin-up IC. Subsequent simulations starting  
 546 from the three ICs show that our optimized IC does a significantly better  
 547 job at reproducing the historically observed circulation patterns. In §4.2, we  
 548 consider the Taiwan region and compare the results of our optimized ICs, ICs  
 549 using  $\Psi_{C^{iu}}$  from averaging and two spin-up ICs. We also compare hindcast  
 550 simulations initialized from four different fields to independent *in situ* data  
 551 off the coast of Taiwan. The hindcasts from reduced physics ICs outperform  
 552 those from spin-up ICs, with the hindcast from our optimized ICs providing  
 553 again the overall best fit to data. In the Philippine Archipelago, §4.3, our  
 554 optimization removes spurious velocities introduced by the averaging method.  
 555 In light of the many islands, in §4.3.1 we explore the impacts of different  
 556 choices of weights (§3.2.1) and the application of velocity limits (§3.2.2).  
 557 In §4.3.2, we demonstrate imposing inter-island transports in selected straits  
 558 (eq. 17) in conjunction with the optimization. Finally in §4.3.3, we exemplify  
 559 our optimization in nested configurations. Note that in all these examples  
 560 we compare methods for constructing  $\vec{u}_{(1)}$ ,  $\vec{u}_{(2)}$  and  $H\vec{U}_{(1)}$ . The final initial  
 561  $w$  estimate is computed at a later step, eq. (C.6).

#### 562 4.1. Hawaiian Islands Region

563 We illustrate the steps of our optimization method in a  $269 \times 218$  km  
 564 domain around the island of Kauai, which also encompasses the island of  
 565 Niihau and the western tip of Oahu (Fig. 2). This domain was employed  
 566 for the Kauai-09 field exercise (July 28 - August 8, 2009). We discretize the  
 567 domain with 1 km horizontal resolution and 90 vertical levels in a terrain-  
 568 following coordinate system. We objectively analyze a combination of CTDs  
 569 from GTSP (July 1-24, 2009) with a corrected July WOA01 climatology  
 570 to create July 25, 2009 ICs on flat levels. The correction shifted the mean  
 571 salinity profile in the upper 100 m to be consistent with the 2009 profiles.  
 572 A 7 day analysis SST from the UK NCOF Operational SST and Sea Ice for  
 573 July 25, 2009 is combined with the mapped  $T$  in a 40 m mixed layer with a  
 574 7 m exponential decay in the transition zone.  $\vec{u}_{(0)}$  is then constructed by a  
 575 combination of (i) velocities in geostrophic balance with the 3D  $T/S$  fields  
 576 using a 2000 m level of no-motion (LNM), (ii) velocity anomalies derived  
 577 from SSH anomaly estimates for July 25, 2009 obtained from the Colorado  
 578 Center for Astrodynamic Research (CCAR; Leben et al., 2002), and, (iii)  
 579 feature models for the North Hawaiian Ridge Current (north of Oahu) and

580 the Hawaiian Lee Current (south of Oahu) which add broad northwesterly  
 581 currents that become more westerly with increasing latitude. The surface  
 582 velocity anomalies,  $\Delta\vec{u}_{SSH}$ , derived from the SSH anomaly,  $\Delta\eta_{SSH}$ , are con-  
 583 structed from geostrophy and hydrostatics using

$$\hat{k} \times f \Delta\vec{u}_{SSH} = -g \nabla \Delta\eta_{SSH} \quad (21)$$

584 where  $f$  is the Coriolis factor and  $g$  the acceleration due to gravity. The  
 585  $\Delta\vec{u}_{SSH}$  are extended in the vertical using a Gaussian profile with a 250 m  
 586 decay scale. After the superposition, the simple bathymetry constraints are  
 587 applied, leading to  $\vec{u}_{(0)}$  (Fig. 2(a)). We fit  $\vec{u}_{(1)}$  to the level-by-level coastal  
 588 constraints (Fig. 2(b)), interpolate to the terrain-following coordinates and  
 589 construct  $H\vec{U}_{(0)}$  from the interpolated  $\vec{u}_{(1)}$  (eq. 1, Fig. 2(c)). Even though  
 590  $\vec{u}_{(1)}$  has been fit to coasts,  $\vec{U}_{(0)}$  has not and it still has velocities into the coasts  
 591 of Kauai and Niihau. Thus, we next fit  $\vec{U}_{(1)}$  to the coastal constraints, using  
 592 our optimization (eq. 15, Fig. 2(d)). We then rescale  $\vec{U}_{(1)}$  for the subtidal free  
 593 surface ( $\vec{U}_{(2)}$ , not shown) and finally superimpose barotropic tides, created  
 594 using Logutov and Lermusiaux (2008) with boundary forcing from OTIS  
 595 (Egbert and Erofeeva, 2002), to obtain  $\vec{U}_{(3)}$  (Fig. 2(e)). For comparison,  
 596 we also present an initialization from geostrophy, without the level-by-level  
 597 optimization, with the subtidal barotropic velocity obtained using  $\Psi_{C^{iu}}$  from  
 598 averaging via eq. (13) and with barotropic tides superimposed (Fig. 2(f)).  
 599 The averaging overestimates the transport between the islands.

600 Fig. 3 compares the initial evolution of three simulations: one using the  
 601 full optimization IC of Fig. 2(e), the second using the averaging IC of Fig. 2(f)  
 602 and the third a spin-up from zero with tidal forcing added. These simulations  
 603 were made using the MSEAS PE model (App. A and HL10) and forced  
 604 with atmospheric fluxes from NOGAPS and the barotropic tides described  
 605 above. To compare the transports between Kauai and Niihau, Fig. 3(a)-3(f)  
 606 show the 24 hr time averages of  $\vec{U}$  at the beginning of the simulation and  
 607 after an initial adjustment to the PE dynamics (4 days). Both the reduced  
 608 physics IC using  $\Psi_{C^{iu}}$  from averaging and the spin-up IC overestimate the  
 609 transports between Kauai and Niihau, even after the initial adjustment. Both  
 610 also have an excessively strong transport inflow along the northern coast of  
 611 Oahu (21.5N,158W). The flow across  $f/H$  contours is due in part to the  
 612 inability of the sparse TS data, coarse TS climatology and the relatively  
 613 coarse SSH to resolve topographic effects. This would also be an issue when  
 614 downscaling from an insufficiently resolved model. A sufficiently resolved TS

615 (say from a dedicated synoptic survey) or downscaling from a sufficiently  
 616 resolved model would resolve topography and remove spurious cross isobath  
 617 flow. The optimization process drives the velocities towards the minimum  
 618 transport  $\Psi_{(0)}$  between these islands that is in accord with the initial guess.  
 619 Since none of the initial TS, SSH, nor feature models contained strong initial  
 620 guess currents between the islands, the optimized currents are diverted away  
 621 from the channel and around the topography, much more closely following  
 622 vorticity contours ( $f/H$  if that is the dominant term). “Averaging” merely  
 623 splits the transport evenly around each island, which concentrates the flow  
 624 between them. The initial spin-up also blindly splits the transport around  
 625 each island. In real-time exercises, even the addition of data assimilation of  
 626 the available sparse data did not correct the initial transports (not shown).  
 627 Hence, the optimization (especially eq. 15) provides additional information  
 628 on the inter-island transports which enables it to produce superior ICs to  
 629 those from spin-up or “averaging”.

630 Fig. 4(a) shows the 50 m temperature from day 4 of the simulation from  
 631 optimized ICs. Differences in the 50 m temperature between the run from  
 632 averaged  $\Psi_{C^{iu}}$  IC and our optimized IC, and between the spin-up IC and the  
 633 optimized IC, are shown in Fig. 4(c) and 4(d) respectively. The differences are  
 634 significant,  $O(1-1.5\text{ }^{\circ}C)$ . Large patches of higher differences to the Northwest  
 635 of Kauai by day 4 start as smaller regions off the Northern tip of Niihau and  
 636 are advected to the north. These differences are directly attributable to  
 637 the difference in transports. The differences in temperature between the 3  
 638 simulations continue to grow throughout the 2 week simulation (Fig. 4(b)),  
 639 even though the transports become more similar to each other (not shown).  
 640 This indicates that initial kinetic energy errors are transferred to potential  
 641 energy errors, as hinted in the problem statement.

642 The circulation pattern of the optimized solution is corroborated by data.  
 643 Qiu et al. (1997) produced a spaghetti diagram of surface drifter tracks  
 644 around the Hawaiian islands for the period 1989-1996. Many more drifters  
 645 passed south or north of Kauai/Niihau than crossed between them. Chavanne  
 646 et al. (2007) produced a map of surface currents for 9 April 2003, using al-  
 647 timetry and high frequency radar. A strong westward current is seen south of  
 648 Kauai/Niihau with only a small current between them. Firing and Brainard  
 649 (2004) examined 10 years of shipboard ADCP from 1990-2000. Among their  
 650 conclusions was that the North Hawaiian Ridge Current flowed (westward)  
 651 to the south of Kauai/Niihau. The common element, namely the current be-  
 652 ing primarily around Kauai/Niihau rather than between them, is much more

653 faithfully represented using the optimization ICs rather than the averaging or  
654 spin-up ICs. Even a variational initialization could benefit by starting from  
655 the optimized ICs, to drastically reduce the number of iterations or prevent  
656 convergence to a wrong local minima, especially if the available data are too  
657 sparse. Finally, we stress again that during a numerical “model adjustment”  
658 of too inaccurate (too large or too small) velocities, both the density and  
659 velocity fields are modified. Even if the velocities are corrected by such ad-  
660 justments, the modeled fields still have some memory of the erroneous initial  
661 velocity (the adjustment is dynamical after all). Such errors can thus dam-  
662 age the field estimation for some time, especially if the erroneous inter-island  
663 velocities are well within the interior of the modeling domain, in which case  
664 their dynamical effects could remain there for a significant duration. In fact,  
665 it is likely that only data assimilation could correct these effects. Of course,  
666 even if there is sufficient data to correct these effects, assimilating data into  
667 fields that have smaller errors reduces the potential for assimilation shock.

#### 668 4.2. Taiwan-Kuroshio Region

669 We next consider a  $1125 \times 1035$  km domain off the southeast coast of  
670 China encompassing Taiwan and the Kuroshio. This domain was employed  
671 for one of the Quantifying, Predicting and Exploiting uncertainty experi-  
672 ments during Aug 13 - Sep 10, 2009 (Gawarkiewicz et al., 2011). We dis-  
673 cretize the domain with 4.5km horizontal resolution and 70 vertical levels in a  
674 terrain-following coordinate system (HL10). For the initialization, we objec-  
675 tively analyze a summer climatology  $T/S$  data set created from HydroBase 2  
676 (Lozier et al., 1995) and World Ocean Atlas 2001 (WOA-01; Stephens et al.,  
677 2002; Boyer et al., 2002). We compute  $\vec{u}_{(0)}$  using the thermal wind eqs. with  
678 a 1000 m LNM and imposing the simple bathymetry constraints. We then  
679 construct  $\vec{u}_{(1)}$ , satisfying the level-by-level coastal constraints, interpolate to  
680 terrain-following coordinates and construct the first-guess sub-tidal trans-  
681 port  $H\vec{U}_{(0)}$  from the interpolated  $\vec{u}_{(1)}$  (eq. 1). We then fit  $\vec{U}_{(1)}$  to the coastal  
682 constraints, using our optimization (eq. 15).

683 We compare the 25 m velocity from the above initialization (Fig. 5(a)) to  
684 three other initializations. The first starts from the same  $\vec{u}_{(0)}$ , does not apply  
685 the level-by-level optimization and constructs a nondivergent  $\vec{U}$  using  $\Psi_{C^{iu}}$   
686 obtained by averaging (eq. 13, Fig. 5(b)). The other two ICs are spin-ups  
687 from zero velocity, the first “freezing” tracers at the initial values (Fig. 5(c)),  
688 the second allowing the tracers to vary during the spin-up but nudged to their  
689 ICs at the boundaries (Fig. 5(d)). Both the optimized IC and the IC using

690 averaged  $\Psi_{C^{iu}}$  (Fig. 5(a) and 5(b)) show a defined Kuroshio current. The  
 691 spin-up ICs after 12.5 days of adjustment do not show nearly as well-defined  
 692 Kuroshio currents, even though their KEs have stabilized by then (Fig. 5(e)).  
 693 Also shown in Fig. 5(e) are the KE from the unforced simulations from the  
 694 reduced physics ICs. The optimized and averaged  $\Psi_{C^{iu}}$  ICs show a much more  
 695 uniform KE history over the simulation, indicating that the reduced physics  
 696 ICs were near one attracting dynamic equilibria of the PE dynamics for that  
 697 region and period. The spin-up solutions have KEs with large oscillations for  
 698 a long duration before settling into different attracting regime (with larger  
 699 KE). The larger KE in spin-up solutions are reflected in over estimates of  
 700 currents and eddies away from the Kuroshio. That a nonlinear PE model can  
 701 have multiple (dynamic) equilibria should come as no surprise, even relatively  
 702 simple nonlinear systems can have multiple equilibria (Dijkstra and Katsman,  
 703 1997; Simonnet et al., 2009; Sapsis et al., 2013).

704 Forced hindcast simulations, starting from 5 Aug 2009, from these ICs  
 705 were made using the MSEAS PE model (App. A and HL10) with atmospheric  
 706 fluxes from NOGAPS and barotropic tides created using Logutov and Lermu-  
 707 siaux (2008) with boundary forcing from OTIS (Egbert and Erofeeva, 2002).  
 708 Fig. 6 shows the 100 m velocities from these simulations. After 20 days, the  
 709 simulations from the reduced physics ICs (Fig. 6(c), 6(f)) maintain defined  
 710 Kuroshio currents and develop a loop branch into the strait of Luzon. The  
 711 spin-up from frozen tracers develops a better defined Kuroshio in the interior  
 712 but not at the inflow and outflow boundaries of the domain (Fig. 6(i)). The  
 713 Kuroshio in the spin-up from nudged tracers loses coherency (Fig. 6(l)). Fig.  
 714 7 shows a comparison of the 100 m temperature between these hindcasts.  
 715 The 100 m  $T$  of the simulation from optimized ICs is shown in Fig. 7(a)-  
 716 7(c). Differences between 100 m  $T$  from the run using averaged  $\Psi_{C^{iu}}$  ICs  
 717 with the 100 m  $T$  from the run using optimized ICs are in Fig. 7(d)-7(f).  
 718 Larger ( $0.25\text{ }^{\circ}C$ ) differences appear in initial adjustment (0.25 d, Fig. 7(e))  
 719 off the NE coast of Taiwan. These differences advect off Taiwan and lead to  
 720 differences in the Kuroshio of  $0.1\text{-}0.2\text{ }^{\circ}C$ . The simulations from spin-up ICs  
 721 showed larger differences,  $1\text{ }^{\circ}C$  for the spin-up from “frozen” tracers (Fig.  
 722 7(g)-7(i)) and  $1\text{-}2\text{ }^{\circ}C$  for the spin-up in which tracers were allowed to vary  
 723 (Fig. 7(j)-7(l)). These differences grew throughout the 20 day simulation.

724 We compare the hindcasts to independent  $T$  data from sea gliders (Gawarkiewicz  
 725 et al., 2011) repositioned in the Kuroshio off the coast of Taiwan (Fig. 8(a)-  
 726 8(b)) during 19-22 August 2009, 2 weeks into the simulations. Temperature  
 727 RMS errors (averaged along the glider tracks, Fig. 8(c)) show that the hind-



728 casts from the optimized and averaged  $\Psi_{C^{in}}$  ICs have significantly smaller  
729 errors than did the hindcasts from spin-up ICs. Along-track temperature  
730 differences between the hindcasts from optimized ICs and the glider data  
731 are shown in Fig. 8(d). Similar difference sections are shown for the other  
732 hindcasts (Fig. 8(e)-8(g)), but only where these differences exceed the dif-  
733 ferences in the optimized run. The optimized ICs are better than all other  
734 simulations almost everywhere.

### 735 4.3. Philippine Archipelago

736 For further evaluation of our methodology, we turn to the Philippine  
737 Archipelago region during February 2 - March 20, 2009, as part of the Philip-  
738 pine Straits Dynamics Experiment (PhilEx; Gordon and Villanoy, 2011; Ler-  
739 musiaux et al., 2011). We consider a  $1656 \times 1503$  km domain (Fig. 9) that is  
740 discretized with 9 km horizontal resolution and 70 vertical levels in a general-  
741 ized coordinate system. The resulting geometry is complex, with 30 interior  
742 islands, 2 exterior coasts and numerous straits. A 2 Feb 2009 initialization  
743 is created using the February WOA05 climatology (Locarnini et al., 2006;  
744 Antonov et al., 2006) mapped with the FMM-based OA (Agarwal and Ler-  
745 musiaux, 2011). The  $\vec{u}_{(0)}$  is constructed using a combination of (i) velocities  
746 in geostrophic balance with a 1000 m LNM, (ii) velocity anomalies derived  
747 from SSH anomaly (CCAR; Leben et al., 2002) using eq. (21) vertically  
748 extended with a 400 m Gaussian decay scale, (iii) feature model velocities  
749 for the bottom currents through the Mindoro (12N,120.75E) and Dipolog  
750 (9N,123E) Straits, and, (iv) at the open boundaries, transports from the  
751 HYbrid Coordinate Ocean Model (HYCOM; Bleck, 2002; Hurlburt et al.,  
752 2011). When using feature models for straits, care is needed to ensure the  
753 transports enter and exit through  $\partial\mathcal{D}$ , rather than close in the interior of  $\mathcal{D}$ .  
754 Based on literature estimates the flow originated a mid-level jet in the South  
755 China Sea (SCS; 15N,120E) and broadly exited the domain in the Mindanao  
756 current in the Pacific (7N,123E). To model this we added a feature model jet  
757 in the SCS and a boundary outflow velocity in the Pacific:

$$u_{FM} = u_{Mindoro} + u_{Dipolog} + u_{SCS} + u_{boundary\ outflow}$$

758 and use eq. (5) to smoothly join the pieces. The HYCOM transports are  
759 divided by bathymetry of our modeling domain to produce barotropic veloc-  
760 ities, which are then added to the velocities from (i)-(iii) at the open bound-  
761 aries of the modeling domain. This procedure puts the HYCOM transports

762 directly into  $\Psi_{be}$  (eq. 10) and uses the optimizing eq. (5) to extend these  
 763 boundary transports into the interior, consistent with our bathymetry and  
 764 coastlines. Applying the simple bathymetry constraints leads to  $\vec{u}_{(0)}$ . Fol-  
 765 lowing with the level-by-level coastal constraints results in  $\vec{u}_{(1)}$ , which is  
 766 interpolated to generalized coordinates and used to construct  $H\vec{U}_{(0)}$  (eq. 1).

767 We start by comparing in Fig. (9) the fields  $\Psi$  and  $\vec{U}_{(1)}$  estimated using  
 768 island values,  $\Psi_{C^{iu}}$ , obtained by our optimization (eq. 15) to those estimated  
 769 using  $\Psi_{C^{iu}}$  obtained by averaging of  $\Psi_{(0)}$  along the islands (eq. 13). In the  
 770 broad strokes, the solution obtained from averaging (Figs. 9(b) and 9(d))  
 771 agrees with that obtained from the optimization (Figs. 9(a) and 9(c)). This  
 772 can be attributed to the constraints imposed by the SSH and HYCOM trans-  
 773 ports on the overall solution and by bathymetry constraints on the currents  
 774 (e.g. the Northern Equatorial Current, NEC, which has already split into  
 775 northern and southern branches by the time it enters the eastern boundary of  
 776 our domain, remains east of the archipelago, following the Philippines escarp-  
 777 ment). However, looking at differences (Figs. 9(b) and 9(d)), we see signifi-  
 778 cant updates in how currents circulate the Archipelago in the two solutions.  
 779 The solution obtained from averaged  $\Psi_{C^{iu}}$  suffers from over estimates of the  
 780 sub-tidal transports in many of the straits (near the northern end of the is-  
 781 land of Palawan (12N,120E); in the Balabac Strait (7N,117E), Surigao Strait  
 782 (10.5N,126E), Sibutu Strait (5N,120E) and Zamboanga Strait (5N,122E);  
 783 and between the islands of Panay and Negros (12N,123E)): peak barotropic  
 784 velocities reach 110 cm/s. The solution obtained using optimized  $\Psi_{C^{iu}}$  re-  
 785 duces the peak barotropic velocity to 48 cm/s (around Borneo (5N,119E),  
 786 eastern Sulu Archipelago (6N,122E) and northern end of Palawan).

#### 787 4.3.1. Optimization weights and velocity limits

788 We now consider the effects of different choices for the weights ( $\varpi_{nm}^{uu}$ ,  
 789  $\varpi_{nk}^{uc}$  and  $\varpi_{nb}^{uo}$ ) in the island optimization as well as the effects of including  
 790 velocity limits. In Fig. 9(c), we presented  $\vec{U}_{(1)}$  computed using  $\Psi_{C^{iu}}$  obtained  
 791 by our optimization with weights equal to the reciprocal of the square of the  
 792 minimum cross-sectional area between the islands obtained via FMM, i.e.  
 793  $\varpi_{nm}^{uu} = (\mathcal{A}_{global\ min}/\mathcal{A}_{nm})^2$ , similarly for  $\varpi_{nk}^{uc}$  and  $\varpi_{nb}^{uo}$ . To this, we compare  
 794 the  $\vec{U}_{(1)}$  computed using  $\Psi_{C^{iu}}$  obtained by our optimization but weighted by  
 795 the squared-reciprocal of the minimum Euclidean distance ( $d_{Enm}^2$ ) between  
 796 the islands, i.e.  $\varpi_{nm}^{uu} = (d_{E\ global\ min}/d_{Enm})^2$ , similarly for  $\varpi_{nk}^{uc}$  and  $\varpi_{nb}^{uo}$  and  
 797 weighted by the squared reciprocal of the minimum in-water distance com-

798 puted by FMM, i.e.  $\varpi_{nm}^{uu} = (d_{global\ min}/d_{nm})^2$ , similarly for  $\varpi_{nk}^{uc}$  and  $\varpi_{nb}^{uo}$ .  
799 Both distance weightings produce very similar currents to each other and  
800 increase the peak barotropic velocity to 58 cm/s. This strong similarity be-  
801 tween the two distance-weighted solutions is because the two distance mea-  
802 sures are the same for neighboring islands (with the largest weights) while  
803 they generally differ most for the widest separated islands (with the least  
804 weight). To see the updates between these two distance-weighted solutions  
805 and the area weighted solution, we consider the two difference fields (Figs.  
806 10(a) and 10(b)). The largest updates are in the Sibutu Strait, Balabac  
807 Strait, Visayan sea (11N,123E) and Surigao Strait.

808 We illustrate the velocity limiting option by limiting the target trans-  
809 ports between islands and between islands and coasts with a maximum *av-*  
810 *erage* barotropic velocity of 5 cm/s. The resulting solution slightly reduced  
811 the peak barotropic velocity to 44 cm/s. The differences between the solu-  
812 tions with and without velocity limiting (Fig. 10(c)) show that the largest  
813 differences are in the Sibutu Strait, Balabac Strait, northern Sibuyan sea  
814 (13N,122E), Surigao Strait and eastern Sulu Archipelago.

#### 815 4.3.2. *Imposing inter-island transports*

816 We now utilize and illustrate our optimization method (table 2) but turn-  
817 ing on the option of imposing externally obtained transports between pairs of  
818 islands, eq. (17). Specifically, Gordon et al. (2011) estimate mean westward  
819 transports through the Dipolog (9N,123E) and Surigao (10.5N,126E) Straits  
820 of 0.5 Sv and 0.3 Sv, respectively, using moorings (15 months deployment,  
821 Jan 2008 - Mar 2009) and ADCP from several cruises (Jun 2007, Jan 2008  
822 and Mar 2009). For the much smaller subset period 2 Feb - 25 Mar 2009, Ler-  
823 musiaux et al. (2011) estimate a mean 0.77 Sv westward transport through  
824 Dipolog with a 1.4 Sv standard deviation (fig. 7e). During 2-8 Feb 2009, they  
825 find that the mean transport through Dipolog is reversed (mean eastward  
826 transport of 0.7 Sv and an initial eastward transport of 1.1 Sv) in response  
827 to the northeast monsoon (May et al., 2011). Hence we choose here as an  
828 extreme test to impose the Gordon et al. (2011) 15-month-average trans-  
829 ports in an updated Feb 2 initialization. Of course, these 15-month averages  
830 are not expected to be accurate for the single-day 2 Feb 2009 transports,  
831 we merely use them as a test of our method: the average and single-day  
832 transport estimates are within the variability and so are representative of  
833 the kinds of changes the method should be able to handle. The questions  
834 we wish to answer are: (a) can the method impose these values? and (b) if

835 so, are the transports through the remaining straits still sensible? For the  
 836 first question, we ran our optimization with a wide range of weights, shown  
 837 in table 3. From this we see that these specific transports can be imposed if  
 838 the weights are large enough (increase the FMM weights by a factor 100 for  
 839 Surigao and by a factor of 1000-10000 for Dipolog). To answer the second  
 840 question, the barotropic velocities resulting from the imposed transports are  
 841 shown in Fig. 11 for the PhilEx domain previously shown and two nested  
 842 sub-domains with 3 km resolution. The first is a  $552 \times 519$  km domain cov-  
 843 ering the Mindoro Strait and the Sibuyan and Visayan seas. The second  
 844 is a  $895 \times 303$  km domain covering the Bohol Sea (9N,125E). The number  
 845 and distribution of generalized vertical levels in both sub-domains is identi-  
 846 cal to the 9 km domain, although the bathymetry is refined. Even though  
 847 the transports are reversed through Dipolog and Surigao, the barotropic ve-  
 848 locities elsewhere remain sensible (peak values remain less than 50 cm/s in  
 849 all domains), confirming that such reversal could occur in the real ocean.  
 850 Looking at the differences between the solution with and without imposed  
 851 transports (Fig. 11(b)), we see the changes are as expected. The flows are  
 852 reversed in the two straits as imposed. The imposition of a larger trans-  
 853 port through Dipolog than Surigao draws additional transport through the  
 854 San Bernadino strait (12N,124E) and the Visayan Sea. The added trans-  
 855 port through Dipolog into the Sulu Sea (7.5N,120E) exits through the Sulu  
 856 Archipelago. Elsewhere the changes are negligible.

### 857 4.3.3. Nesting strategies

858 We now exemplify our optimized initialization for use in nested multi-  
 859 resolution simulations (HL10). To ensure consistency between a coarse and  
 860 fine solution, we obtain the BCs at the outer boundary of the fine domain  
 861 by interpolation from the coarse domain solution (i.e. we by-pass eq. (10)  
 862 the ‘‘Construct Exterior BCs’’ step of table 2 and instead interpolate the  
 863 coarse-domain  $\Psi$  to obtain the fine domain  $\Psi_{b^e}$  values). Here we explore how  
 864 much of the additional information from the coarse domain (i.e. inter-island  
 865 transports) should be included in the fine domain solution.

866 We consider the 3 km Mindoro Strait domain nested within our larger  
 867 9 km domain. In Fig. 12, we zoom in on the southeast portion of our nested  
 868 sub-domain, encompassing the Sibuyan sea. Fig. 12(a) shows the  $\vec{U}_{(1)}$  in the  
 869 9 km domain obtained with our optimization scheme (table 2) including the  
 870 velocity limiting option with an imposed maximum 80 cm/s target average  
 871 barotropic velocity. Fig. 12(b) shows the final  $\vec{U}_{(1)}$  in the 3 km domain. We

872 compare this final result with a couple of different strategies. The first was  
873 to not only use the 9 km solution for BCs,  $\Psi_{be}$ , at the outer boundary of the  
874 3 km domain, but to also retain the transport streamfunction values along the  
875 islands that are also resolved in the larger domain (e.g. Mindoro 13N,121E;  
876 Panay 11N,123E). This occurs in two steps (i) these values of  $\Psi_{C^c}$  are included  
877 in the “certain coast solution” (eq. 12 and table 2) and (ii) these islands are  
878 included in the set of coastlines with known streamfunction values. The  
879 intent is to ensure a greater consistency between the initial coarse and fine  
880 domain fields. The difference between this strategy and the final strategy  
881 is shown in Fig. 12(c). An unintended consequence of retaining the 9 km  
882 island values is an increase in  $\vec{U}_{(1)}$  in certain channels due to the increased  
883 coastal and bathymetry resolution of the fine domain. In particular, the peak  
884  $\vec{U}_{(1)}$  in the Verde Island passage between Mindoro and Luzon (13.5N,121E)  
885 increases from 17 cm/s in the coarse domain to 50 cm/s in the fine.

886 To reduce these velocities, we allow our optimization algorithm to work  
887 on all the islands in the fine domain: the streamfunction values on all islands  
888 are then assumed uncertain. The OBCs are still obtained by interpolation  
889 from the 9 km domain. Fig. 12(d) shows the difference between this strategy  
890 and the final one. Optimizing these island values for the fine domain reduces  
891 the peak barotropic velocity in the Verde Island passage to 30 cm/s, but  
892 increases it to 30 cm/s at the southern tip of Mindoro (12.25N,121E). When  
893 we add velocity limits to the optimization (keeping the interpolated OBCs,  
894 our final strategy), we obtain the results shown on Fig. 12(b): the peak  
895 barotropic velocities are brought down to 20 cm/s in the Verde Island passage  
896 and 10 cm/s at the southern tip of Mindoro. This shows that for nested  
897 initialization, our weak-constraint optimization algorithm should be used for  
898 all islands, adding local weak velocity bounds as needed. The results are then  
899 well adjusted fine domain fields that still match the coarse domain solution  
900 at the boundaries of the fine domain.

## 901 5. Summary and Conclusions

902 In this manuscript, we derived and applied a methodology for the efficient  
903 semi-analytical initialization of 3D velocity and transport fields in coastal  
904 regions with multiscale dynamics and complex multiply-connected geometries,  
905 including islands and archipelagos. These fields are consistent with the  
906 synoptic observations available, geometry, free-surface PE dynamics and any  
907 other relevant information to evolve without spurious initial transients. They

908 can be directly used for model initialization or as an improved initial guess  
909 for a variational scheme.

910 Our weighted least squares optimization starts from first-guess sub-tidal  
911 velocity fields that satisfy simple bathymetric constraints. To obtain the ex-  
912 act solutions for the first correction velocities which best fit these first-guesses  
913 while satisfying no-normal flow into complex coastlines and bathymetry, we  
914 derive successive level-by-level (layer-by-layer) Euler-Lagrange equations for  
915 the interior, boundary and island streamfunction variables. These new equa-  
916 tions are: (i) a Poisson equation for a streamfunction representation of the  
917 velocity; (ii) a 1D Poisson equation along the external boundary for the  
918 Dirichlet OBCs which best fit the first-guess flow through the open bound-  
919 aries; and (iii) robust algebraic equations for selecting constant values for  
920 the streamfunction along the uncertain islands, best-fitting the first-guess  
921 values using weights that are functions of minimum ocean distances or cross  
922 sectional areas, both computed by FMM. A second correction is derived for  
923 cases where the full 3D dynamics is critical, employing a predictor-corrector  
924 algorithm to fit the no-normal flow constraints in 3D. The first guess sub-  
925 tidal transport is computed from either the first or second guess velocities  
926 as appropriate. A first correction transport is then computed using steps  
927 (i)-(iii) derived for transport. Additional information on the transport and  
928 velocity fields is also incorporated as weak or strong constraints, including  
929 for example specific net transports between coasts or weak upper and lower  
930 bounds on the barotropic velocity in specific straits.

931 We applied our methodology in three regions: (i) around the Hawaiian  
932 islands of Kauai/Niihau (ii) the Taiwan/Kuroshio region, and (iii) in the  
933 Philippines Archipelago. In the Hawaiian study, four day simulations from 3  
934 initializations were compared: (i) starting from our optimized ICs (ii) from  
935 ICs using averaged  $\Psi_{C^{iu}}$  and (iii) from spin-up ICs. If our optimization is not  
936 used, both the ICs and the initial adjustment simulations from the ICs over  
937 estimate the transport between the islands. Our optimization produced a cur-  
938 rent which was primarily around Kauai/Niihau rather than between them,  
939 in accord with historical observations. The erroneous transports led to large  
940  $O(1-1.5 \text{ }^\circ\text{C})$  differences in temperature. These temperature differences grew  
941 as the simulations progressed (i.e. initial velocity errors were transferred to  
942 tracer errors). In the Taiwan-Kuroshio region, we compared four initializa-  
943 tions and their subsequent evolutions, starting from (i) our optimized ICs,  
944 (ii) ICs using averaged  $\Psi_{C^{iu}}$ , (iii) spin-up with fixed TS and (iv) spin-up al-  
945 lowing TS to vary but nudged to ICs at the open boundaries. Neither of the

946 spin-up ICs led to as well-developed Kuroshio currents as (i) or (ii) did, even  
947 after the spin-up KEs grew and stabilized around an erroneous “attractor  
948 regime”. However, the KEs from the unforced runs of (i) and (ii) showed a  
949 KE history quasi-steady at the optimized value. The forced 20-day hindcasts  
950 confirmed the advantages of initializing from our optimized velocities, includ-  
951 ing better representations of the Kuroshio. The quantitative evaluation of  
952 these hindcasts by comparison with independent *in situ* data after 2 weeks  
953 of simulation showed by far the largest errors in the hindcasts from spin-up  
954 while our optimized ICs produced the best match.

955 The third region was the multiply-connected Philippines Archipelago.  
956 The solution obtained from the averaging method suffered from over esti-  
957 mates of the transports in many of the straits while our optimized solution  
958 produced realistic peak sub-tidal barotropic velocities. We also evaluated  
959 the effects of different weighting functions and showed that using weights  
960 based on the minimum cross-sectional areas among islands (computed by  
961 FMM) was the most adequate. We tested the effects of including weak up-  
962 per bounds on velocities and found that optimized results were in accord with  
963 the bounds chosen. We also showed that our option of weakly imposing ex-  
964 ternally obtained transports between pairs of islands could reverse the initial  
965 flows through the Dipolog and Surigao Straits if the corresponding weights  
966 were strong enough. This example was used to show that transports through  
967 these straits could also reverse in reality since their reversals retained sensible  
968 velocities and expected currents elsewhere. Finally, we studied our optimized  
969 nested initialization schemes to use in multi-resolution simulations. Since  
970 the multi-resolution domains have different bathymetries, coastlines, islands,  
971 flow features and dynamics, we found that the best approach was to let our  
972 optimization algorithm work on all islands and flows between islands, only  
973 imposing the cross-scale information as strong constraints on the boundary  
974 and applying weak bounds on the average barotropic velocity where needed.  
975 The result is then well adjusted multi-resolution initial velocity fields, con-  
976 sistent at all scales within and across the nested domains.

977 We have found that our optimization, particularly the weak constraint  
978 towards the minimum inter-island transport that is in accord with the first-  
979 guess velocities (eq. 15), provides important velocity corrections in complex  
980 archipelagos. This was found to be critical where the available data did  
981 not resolve the bathymetric/coastal effects. The velocity corrections from  
982 our methodology optimized the kinetic energy locally, eliminating unreal-  
983 istic hot-spots, while respecting continuity constraints and the boundary

984 conditions for multiple islands and tortuous coastlines. When optimizing  
985 transports, weighting functions that lead to the minimization of barotropic  
986 velocity differences are found to be more robust and to better control veloc-  
987 ities than those that lead to the minimization of transport differences. In all  
988 of the examples shown, it is key to realize that in complex domains without  
989 our optimization, the initial fields were too erroneous and unbalanced. We  
990 confirmed that such errors can damage predictions for future times.

991 For the future, there are many opportunities for refinement and applica-  
992 tion of our methodology. For the refinements, even though our approach is  
993 independent of the discretization employed, other discretizations (Deleersnij-  
994 der et al., 2010; Ueckermann and Lermusiaux, 2010; Lermusiaux et al., 2013)  
995 may have specific challenges. Different weighting and cost functions can be  
996 researched, for example specific functions for non-hydrostatic flow initializa-  
997 tion. Considering applications to other regions and dynamics, a promising  
998 example is the downscaling of climate predictions to initialize simulations in  
999 complex coastal regions, including sea-level change implications. Real-time  
1000 optimized initialization for rapid responses operations to specific events or  
1001 for other societal applications are useful directions. Finally, ocean ecosys-  
1002 tem initialization (Beşiktepe et al., 2003) as well as other multi-model and  
1003 multi-dynamics applications should be further investigated.

1004 *Acknowledgments* We are grateful to the Office of Naval Research for re-  
1005 search support under grants N00014-08-1-109 (ONR6.1), N00014-08-1-0680  
1006 (PLUS-INP), N00014-08-1-0586 (QPE), N00014-07-1-0473 (PhilEx), N00014-  
1007 09-1-0676 (Autonomy), N00014-11-1-0701 (MURI-IODA), N00014-12-1-0944  
1008 (ONR6.2) and N00014-13-1-0518 (Multi-DA), and to the Naval Research  
1009 Laboratory for research support under grant N00173-13-2-C009 to the Mas-  
1010 sachusetts Institute of Technology. We are thankful to Wayne G. Leslie,  
1011 Carlos Lozano and to the MSEAS group for useful inputs and discussions.  
1012 We are grateful to the QPE, PLUS-INP and PhilEx teams for their fruitful  
1013 collaborations. We thank C. Lee for providing sea glider data and B. Leben  
1014 and CCAR for providing SSH anomaly data. We thank the three anonymous  
1015 reviewers and the associate editor for their useful suggestions.



1016 **Appendices**

1017 **A. Ocean Modeling Primitive Equations and the MSEAS Model-**  
 1018 **ing System**

1019 *Free-Surface Primitive Equations (PEs)*. The equations are derived from the  
 1020 Navier-Stokes equations and first law of thermodynamics and conservation of  
 1021 salt, under the Boussinesq, thin-layer and hydrostatic approximations (e.g.  
 1022 Cushman-Roisin and Beckers, 2010). They consist of,

$$\text{Cons. Mass} \quad \nabla \cdot \vec{u} + \frac{\partial w}{\partial z} = 0 \quad , \quad (\text{A.1})$$

$$\text{Cons. Horiz. Mom.} \quad \frac{D\vec{u}}{Dt} + f\hat{k} \times \vec{u} = -\frac{1}{\rho_0}\nabla p + \vec{F} \quad , \quad (\text{A.2})$$

$$\text{Cons. Vert. Mom.} \quad \frac{\partial p}{\partial z} = -\rho g \quad , \quad (\text{A.3})$$

$$\text{Cons. Heat} \quad \frac{DT}{Dt} = F^T \quad , \quad (\text{A.4})$$

$$\text{Cons. Salt} \quad \frac{DS}{Dt} = F^S \quad , \quad (\text{A.5})$$

$$\text{Eq. of State} \quad \rho = \rho(z, T, S) \quad , \quad (\text{A.6})$$

$$\text{Free Surface} \quad \frac{\partial \eta}{\partial t} + \nabla \cdot \left( \int_{-H}^{\eta} \vec{u} dz \right) = 0 \quad (\text{A.7})$$

1023 where:  $(\vec{u}, w)$  are horizontal and vertical components of velocity;  $(x, y, z)$   
 1024 spatial positions;  $t$  time;  $T$  temperature;  $S$  salinity;  $\frac{D}{Dt}$  three-dimensional  
 1025 material derivative;  $p$  pressure;  $f$  Coriolis parameter;  $\rho$  density,  $\rho_0$  (con-  
 1026 stant) density from a reference state;  $g$  acceleration due to gravity;  $\eta$  surface  
 1027 elevation,  $H = H(x, y)$  local water depth in the undisturbed ocean; and,  $\hat{k}$   
 1028 unit direction vector in the vertical direction. The gradient operators,  $\nabla$ , in  
 1029 eqs. (A.1 & A.2) are two dimensional (horizontal) operators. The turbulent  
 1030 sub-gridscale processes are represented by  $\vec{F}$ ,  $F^T$  and  $F^S$ .

1031 *MSEAS Modeling System*. The above equations are numerically integrated  
 1032 using the finite-volume structured ocean model (HL10) of the Multidisci-  
 1033 plinary Simulation, Estimation and Assimilation System (MSEAS group,  
 1034 2010). MSEAS is used to study and quantify tidal-to-mesoscale processes  
 1035 over regional domains with complex geometries and varied interactions. Mod-  
 1036 eling capabilities include implicit two-way nesting for multiscale hydrostatic

1037 PE dynamics with a nonlinear free-surface (HL10) and a high-order finite  
 1038 element code on unstructured grids for non-hydrostatic processes also with  
 1039 a nonlinear free-surface (Ueckermann and Lermusiaux, 2010, 2014). Other  
 1040 MSEAS subsystems include: initialization schemes, nested data-assimilative  
 1041 tidal prediction and inversion (Logutov and Lermusiaux, 2008); fast-marching  
 1042 coastal objective analysis (Agarwal and Lermusiaux, 2011); stochastic subgrid-  
 1043 scale models (e.g., Lermusiaux, 2006; Phadnis, 2013); generalized adapt-  
 1044 able biogeochemical modeling system; Lagrangian Coherent Structures; non-  
 1045 Gaussian data assimilation and adaptive sampling (Sondergaard and Lermu-  
 1046 siaux, 2013a,b; Lermusiaux, 2007); dynamically-orthogonal equations for un-  
 1047 certainty predictions (Sapsis and Lermusiaux, 2009, 2012; Ueckermann et al.,  
 1048 2013); and machine learning of model formulations. The MSEAS software  
 1049 is used for basic and fundamental research and for realistic simulations and  
 1050 predictions in varied regions of the world’s ocean (Leslie et al., 2008; Onken  
 1051 et al., 2008; Haley et al., 2009; Gangopadhyay et al., 2011; Ramp et al., 2011;  
 1052 Colin et al., 2013), including monitoring (Lermusiaux et al., 2007), naval ex-  
 1053 ercises including real-time acoustic-ocean predictions (Xu et al., 2008) and  
 1054 environmental management (Cossarini et al., 2009).

## 1055 **B. Retaining vertical velocity for 3D effects and more complicated** 1056 **bathymetry constraints**

1057 In this appendix, we deal with cases in which desired velocity properties  
 1058 are fully 3D, including both horizontal and vertical components (e.g. veloci-  
 1059 ties from a dynamical simulation with its own 3D balance, feature models for  
 1060 flows over sills, geostrophic-Ekman balance with bottom interaction) and are  
 1061 of sufficient resolution to contain meaningful estimates of  $w_{(0)}$ . For hydro-  
 1062 static PEs, this vertical velocity comes in through the 2D divergence of the  
 1063 horizontal velocity. However, in §3 the algorithms obtained for fitting the 3D  
 1064 velocities and horizontal transports to the geometry enforce a layer-by-layer  
 1065 2D non-divergence in the chosen vertical discretization. (For non-hydrostatic  
 1066 PEs, one still desires ICs which satisfy continuity.) Hence we now derive a  
 1067 predictor/corrector method to recover the non-zero 2D divergence of the  
 1068 horizontal velocities when that divergence contains a sufficiently meaning-  
 1069 ful estimate of  $w_{(0)}$ . The predictor is the first correction velocity estimate,  
 1070  $\vec{u}_{(1)}$ , that satisfies the 2D level-by-level constraints. The corrector is a ve-  
 1071 locity correction,  $\Delta\vec{u}$ , to recover the nonzero 2D divergences.  $\Delta\vec{u}$  best fits  
 1072 the difference  $\vec{u}_{(1)} - \vec{u}_{(0)}$  under the no-normal flow constraint in 3D (thereby

1073 recovering  $w_{(0)}$  via vertical integration of continuity eq. A.2). The result is  
 1074 the second correction velocity,  $\vec{u}_{(2)} = \vec{u}_{(1)} + \Delta\vec{u}$  which recovers the first guess  
 1075 vertical velocity,  $\nabla \cdot \vec{u}_{(2)} \approx -\frac{\partial w_{(0)}}{\partial z}$ , subject to constraints.

1076 Let  $\vec{u}_{(2)}$  be the second correction velocity which best fits the first-guess  
 1077 velocity,  $\vec{u}_{(0)}$ , while satisfying no-normal flow and retaining the non-zero 2D  
 1078 divergence. By the Helmholtz decomposition,  $\vec{u}_{(2)}$  can be written as

$$\vec{u}_{(2)} = \left( \hat{k} \times \nabla\psi \right) + \nabla\phi \quad (\text{B.1})$$

1079 where  $\psi$  is a level-by-level streamfunction and  $\phi$  is a level-by-level velocity  
 1080 potential.  $\vec{u}_{(1)}$  best fits  $\vec{u}_{(0)}$  while satisfying no-normal flow and

$$\vec{u}_{(1)} = \hat{k} \times \nabla\psi \quad .$$

1081 We choose  $\vec{u}_{(1)}$  as the predictor for  $\vec{u}_{(2)}$  and define the corrector,  $\Delta\vec{u}$ , as

$$\begin{aligned} \Delta\vec{u} &= \vec{u}_{(2)} - \vec{u}_{(1)} \\ &= \nabla\phi \quad . \end{aligned} \quad (\text{B.2})$$

1082 Then, defining

$$\Delta\vec{u}_{(0)} = \vec{u}_{(0)} - \vec{u}_{(1)} \quad , \quad (\text{B.3})$$

1083 the weighted least squares cost function,  $J_{div}$ , to recover the divergence is

$$\begin{aligned} J_{div}(\Delta\vec{u}) &= \frac{1}{2} \iint_{\mathcal{D}} \omega_{\phi} \left\| \Delta\vec{u} - \Delta\vec{u}_{(0)} \right\|^2 da \\ \Leftrightarrow J_{div}(\tilde{\phi}) &= \frac{1}{2} \iint_{\mathcal{D}} \omega_{\phi} \left\| \nabla\tilde{\phi} - \Delta\vec{u}_{(0)} \right\|^2 da \end{aligned} \quad (\text{B.4})$$

1084 where  $\Delta\vec{u}$  is any test velocity corrector,  $\tilde{\phi}$  the corresponding test velocity  
 1085 potential,  $\omega_{\phi}$  a positive definite weighting function and  $da$  an area element.  
 1086 To find the  $\phi$  that minimizes  $J_{div}$ , variational calculus is employed:

$$\begin{aligned} J_{div}(\phi + \delta\phi) &= J_{div}(\phi) + \frac{1}{2} \iint_{\mathcal{D}} \omega_{\phi} \|\nabla(\delta\phi)\|^2 da \\ &\quad - \iint_{\mathcal{D}} \delta\phi \nabla \cdot [\omega_{\phi} (\nabla\phi - \Delta\vec{u}_{(0)})] da \\ &\quad + \oint_{\partial\mathcal{D}} \omega_{\phi} \delta\phi (\nabla\phi - \Delta\vec{u}_{(0)}) \cdot \hat{n} ds \end{aligned} \quad (\text{B.5})$$

1087 The potential  $\phi$  will minimize  $J_{div}$  provided the second and third integrals in  
 1088 eq. (B.5) are zero. Applying the fundamental theorem of variational calculus,  
 1089 these integrals will be identically zero for  $\phi$  satisfying

$$\nabla \cdot (\omega_\phi \nabla \phi) = \nabla \cdot (\omega_\phi \Delta \vec{u}_{(0)}) \quad (\text{B.6})$$

$$\nabla \phi \cdot \hat{n}|_{\partial \mathcal{D}} = \Delta \vec{u}_{(0)} \cdot \hat{n}|_{\partial \mathcal{D}} \quad . \quad (\text{B.7})$$

1090 To enforce no flow through coasts,  $\Delta \vec{u}_{(0,np)}$  is defined as

$$\Delta \vec{u}_{(0,np)} \cdot \hat{n}|_{coasts} = 0 \quad (\text{B.8})$$

$$\Delta \vec{u}_{(0,np)} \cdot \hat{t}|_{coasts} = \Delta \vec{u}_{(0)} \cdot \hat{t}|_{coasts}$$

$$\Delta \vec{u}_{(0,np)} = \Delta \vec{u}_{(0)} \quad \text{elsewhere}$$

1091 where  $\hat{t}$  is the unit tangent. Replacing  $\Delta \vec{u}_{(0)}$  with  $\Delta \vec{u}_{(0,np)}$  in (B.7) results in

$$\nabla \phi \cdot \hat{n}|_{\partial \mathcal{D}} = \Delta \vec{u}_{(0,np)} \cdot \hat{n}|_{\partial \mathcal{D}} \quad . \quad (\text{B.9})$$

1092 As a check on the consistency of using (B.9) with (B.6), eq. (B.6) is integrated  
 1093 over the domain, followed by an application of the divergence theorem, and  
 1094 a substitution from (B.9). The result is the solvability condition

$$\oint_{\partial \mathcal{D}} \omega_\phi \Delta \vec{u}_{(0,np)} \cdot \hat{n} ds = \oint_{\partial \mathcal{D}} \omega_\phi \Delta \vec{u}_{(0)} \cdot \hat{n} ds \quad . \quad (\text{B.10})$$

1095 Along the open boundaries,  $\Delta \vec{u}_{(0)} = \Delta \vec{u}_{(0,np)}$  while along the coasts  $\Delta \vec{u}_{(0,np)} \cdot \hat{n}$   
 1096 is zero. Therefore, eq. (B.10) reduces to

$$\int_{coasts} \omega_\phi \Delta \vec{u}_{(0)} \cdot \hat{n} ds = 0 \quad . \quad (\text{B.11})$$

1097 In general eq. (B.11) is not satisfied. Therefore a ‘‘no net normal flow’’ target  
 1098 velocity correction,  $\Delta \vec{u}_{(0,nnp)}$  is sought which best fits  $\Delta \vec{u}_{(0)}$  while satisfying  
 1099 (B.11). The least squares cost function  $J_{nnp}$  to fit  $\Delta \vec{u}_{(0,nnp)}$  is

$$\begin{aligned} J_{nnp}(\Delta \vec{u}_{(0,nnp)}; \lambda) &= \int_{coasts} \omega_\phi (\Delta \vec{u}_{(0,nnp)} \cdot \hat{n} - \Delta \vec{u}_{(0)} \cdot \hat{n})^2 ds \\ &+ \lambda \int_{coasts} \omega_\phi \Delta \vec{u}_{(0,nnp)} \cdot \hat{n} ds \end{aligned} \quad (\text{B.12})$$

1100 where  $\lambda$  is a Lagrange multiplier. To minimize eq. (B.12) we take derivatives  
 1101 of  $J_{nnp}$  with respect to  $\Delta \vec{u}_{(0,nnp)}$  and  $\lambda$  and set them equal to zero:

$$\frac{\partial J_{nnp}}{\partial \Delta \vec{u}_{(0,nnp)}} = \omega_\phi (\Delta \vec{u}_{(0,nnp)} \cdot \hat{n} - \Delta \vec{u}_{(0)} \cdot \hat{n}) + \omega_\phi \lambda = 0$$

$$\frac{\partial J_{nnp}}{\partial \lambda} = \int_{coasts} \omega_\phi \Delta \vec{u}_{(0, nnp)} \cdot \hat{n} ds = 0 \quad . \quad (\text{B.13})$$

1102 Solving the resulting system yields:

$$\begin{aligned} \Delta \vec{u}_{(0, nnp)} \cdot \hat{n} \Big|_{coasts} &= \Delta \vec{u}_{(0)} \cdot \hat{n} \Big|_{coasts} - \frac{\int_{coasts} \omega_\phi \Delta \vec{u}_{(0)} \cdot \hat{n} ds}{\int_{coasts} \omega_\phi ds} \quad (\text{B.14}) \\ \Delta \vec{u}_{(0, nnp)} \cdot \hat{t} \Big|_{coasts} &= \Delta \vec{u}_{(0)} \cdot \hat{t} \Big|_{coasts} \\ \Delta \vec{u}_{(0, nnp)} &= \Delta \vec{u}_{(0)} \quad \text{elsewhere} \quad . \end{aligned}$$

1103 Substituting (B.14) in (B.6), results in the well-posed modified system

$$\begin{aligned} \nabla \cdot (\omega_\phi \nabla \phi) &= \nabla \cdot (\omega_\phi \Delta \vec{u}_{(0, nnp)}) \quad (\text{B.15}) \\ \nabla \phi \cdot \hat{n} \Big|_{\partial \mathcal{D}} &= \Delta \vec{u}_{(0, nnp)} \cdot \hat{n} \Big|_{\partial \mathcal{D}} \quad . \end{aligned}$$

1104 The level-by-level solutions to (B.15) are substituted into (B.2), and solved  
1105 for  $\vec{u}_{(2)}$ , which preserves no-normal flow in the final velocities:

$$\vec{u}_{(2)} = \vec{u}_{(1)} + \nabla \phi \quad . \quad (\text{B.16})$$

## 1106 C. Free surface and tidal initialization

1107 This appendix summarizes our scheme to create ICs consistent with the  
1108 free surface and tides in complex domains. Some of this material is in  
1109 app. 2.2-2.3 of HL10. Here we expand on details needed for the present  
1110 work and apply the notation of this manuscript.

### 1111 C.1. Sub-tidal free surface

1112 Once velocities and transport are constrained for the model geometry, we  
1113 need a sub-tidal free surface in dynamic balance with them. When initializing  
1114 from another model output, the free surface should be directly available.  
1115 When initializing from reduced dynamics, a consistent free surface needs  
1116 to be constructed. Summarizing app. 2.2 of HL10, the reduced dynamical  
1117 equation, with the free surface contribution made explicit, is integrated in  
1118 the vertical (HL10 eq. 67) and the divergence operator is applied to obtain  
1119 a Poisson equation for  $\eta_{(0)}$  (HL10 eq. 68). Dirichlet OBCs are obtained by  
1120 a tangential integral of the vertically integrated equation along the open  
1121 boundaries. Along the coastlines, no-normal flow is enforced by applying

1122 zero Neumann conditions. The resulting system of equations is solved for  
 1123  $\eta_{(0)}$ . To maintain the transport, the barotropic velocity is rescaled from

$$\vec{U}_{(2)} = \frac{H}{H + \eta_{(0)}} \vec{U}_{(1)} \quad . \quad (\text{C.1})$$

1124 If tides are not in initial fields,  $\vec{u}'$ ,  $\vec{u}$  and  $w$  are constructed using eqs. (C.4–  
 1125 C.6) but with  $\eta_{(0)}$ ,  $\vec{U}_{(2)}$  replacing  $\eta_{(1)}$ ,  $\vec{U}_{(3)}$  ( $\vec{u}$  still respects no-normal flow).

### 1126 C.2. Tides and other external forcing

1127 The final step of the initialization is to obtain the tidal free surface and  
 1128 velocity, and add both to the sub-tidal fields computed above. Regional  
 1129 barotropic tidal fields are readily available (e.g., Egbert and Erofeeva, 2002,  
 1130 2013) and if higher spatial resolutions are needed, finer inversions can be  
 1131 used (e.g., Logutov, 2008; Logutov and Lermusiaux, 2008). The barotropic  
 1132 tides,  $\eta_{tide}$  and  $\vec{U}_{tide}$ , are best-fit to a set of tidal fields under the constraints  
 1133 of satisfying the exact discrete divergence relation of the model geometry  
 1134 and no-normal flow into coasts. The tidal elevations and transports are  
 1135 superimposed with the sub tidal counterparts constructed in §C.1

$$\eta_{(1)} = \eta_{(0)} + \eta_{tide} \quad (\text{C.2})$$

$$\vec{U}_{(3)} = \frac{H + \eta_{(0)}}{H + \eta_{(1)}} \vec{U}_{(2)} + \begin{cases} \frac{H}{H + \eta_{(1)}} \vec{U}_{tide} & \text{linear tidal model} \\ \frac{H + \eta_{tide}}{H + \eta_{(1)}} \vec{U}_{tide} & \text{nonlinear tidal model} \end{cases} \quad (\text{C.3})$$

1136 Finally these elevations and transports are combined with the chosen vertical  
 1137 shear and continuity to obtain the initial velocities:

$$\vec{u}' = \begin{cases} \vec{u}_{(2)} - \frac{1}{H + \eta_{(1)}} \int_{-H}^{\eta_{(1)}} \vec{u}_{(2)} dz & \text{if 3D constraints (see App. B)} \\ \vec{u}_{(1)} - \frac{1}{H + \eta_{(1)}} \int_{-H}^{\eta_{(1)}} \vec{u}_{(1)} dz & \text{otherwise} \end{cases} \quad (\text{C.4})$$

$$\vec{u} = \vec{u}' + \vec{U}_{(3)} \quad (\text{C.5})$$

$$w = - \int_{-H}^z \nabla \cdot \vec{u} d\zeta - (\vec{u} \cdot \nabla H)|_{z=-H} \quad . \quad (\text{C.6})$$

1138 With these choices for  $\vec{u}$  and  $w$ , the initial velocities will also satisfy

$$w|_{z=\eta_{(1)}} = \frac{\partial \eta_{tide}}{\partial t} + (\vec{u} \cdot \nabla \eta_{(1)})|_{z=\eta_{(1)}} \quad ; \quad w|_{z=-H} = - (\vec{u} \cdot \nabla H)|_{z=-H} \quad ; \quad \frac{\partial \eta_{tide}}{\partial t} + \nabla \cdot \int_{-H}^{\eta_{(1)}} \vec{u} dz = 0$$

1139 which represent the kinematic BCs at the top and bottom and the vertically  
 1140 integrated conservation of mass, all under the previously stated assumption  
 1141 that non-tidal temporal variations in the free surface are negligible. Note that  
 1142 for time-dependent BCs, the superposition of tidal and sub tidal components  
 1143 is also done, but with the sub-tidal components computed above and the  
 1144 tidal components evaluated in real time from an attached tidal model.

## 1145 D. Derivations of Cost Functions

1146 Here we briefly outline the derivation the cost functions and subsequent  
 1147 schemes for optimizing them. Details are in available in Haley et al. (2014).

### 1148 D.1. Evaluating full domain cost function, $J$ , for variations around $\Psi$

1149 Substituting eq. (3) or eq. (4) in eq. (2), and performing a bit of algebra  
 1150 to transfer the  $\hat{k} \times$  term, we obtain for  $J$ ,

$$J(\tilde{\Psi}) = \frac{1}{2} \iint_{\mathcal{D}} \omega \left( \hat{k} \times H\vec{U}_{(0)} + \nabla\tilde{\Psi} \right) \cdot \left( \hat{k} \times H\vec{U}_{(0)} + \nabla\tilde{\Psi} \right) da. \quad (\text{D.1})$$

1151 Applying calculus of variations to obtain the  $\Psi$  that minimizes  $J$  yields

$$\begin{aligned} J(\Psi + \delta\Psi) &= J(\Psi) + \frac{1}{2} \iint_{\mathcal{D}} \omega \|\nabla(\delta\Psi)\|^2 da \\ &\quad - \iint_{\mathcal{D}} \delta\Psi \nabla \cdot \left[ \omega \left( \nabla\Psi + \hat{k} \times H\vec{U}_{(0)} \right) \right] da \\ &\quad + \oint_{\partial\mathcal{D}} \omega \delta\Psi \left( \nabla\Psi + \hat{k} \times H\vec{U}_{(0)} \right) \cdot \hat{n} ds \end{aligned} \quad (\text{D.2})$$

1152 where  $\partial\mathcal{D}$  is the boundary of the domain  $\mathcal{D}$ .  $\Psi$  will minimize  $J$  provided  
 1153 the second and third integrals in eq. (D.2) are zero for all permissible choices  
 1154 of  $\delta\Psi$ . The second integral will only be identically zero for all  $\delta\Psi$  if the  
 1155 divergence in the integrand is everywhere zero. For the third integral around  
 1156  $\partial\mathcal{D}$ , two choices exist. One choice would be to set  $(\nabla\Psi + \hat{k} \times H\vec{U}_{(0)}) \cdot \hat{n}$   
 1157 zero along  $\partial\mathcal{D}$ . This condition would constrain the circulation around the  
 1158 domain. The other choice is to provide Dirichlet BCs to the problem for  
 1159  $\tilde{\Psi}$ , which, in turn, limits the variations  $\delta\Psi$  to those that vanish along the  
 1160 boundary ( $\delta\Psi|_{\partial\mathcal{D}} = 0$ ). Dirichlet BCs provide a pathway for incorporating  
 1161 information on the transports into and out of the domain. Such information  
 1162 is an important addition to reduced physics initializations (e.g. geostrophy),  
 1163 providing constraints on the external forcing applied to the domain. To  
 1164 summarize, the second integrand is set to zero along with Dirichlet BCs.

1165 *D.2. Evaluating exterior boundary cost function,  $J_{b^e}$ , for variations around*

1166  $\Psi_{b^e}$

1167 We separate eq. (6) into a series of integrals along the open boundaries and  
 1168 a series of integrals along the coasts. We introduce the set of  $M^e$  labels for  
 1169 the  $M^e$  external coasts  $\{C_m^e\}$ . The corresponding set of  $M^e$  open boundary  
 1170 segments go from one external coast to the next. They are defined such that  
 1171 the  $m^{\text{th}}$  open boundary segment starts at external coast  $C_m^e$  and ends at  
 1172 external coast  $C_{m+1}^e$  or  $C_1^e$  if  $m = M^e$ . To denote this, we use the notation  
 1173  $C_m^e$ .  $J_{b^e}$  is then rewritten in terms of the open and coastal contributions:

$$\begin{aligned}
 J_{b^e}(\tilde{\Psi}_{b^e}) &= \frac{1}{2} \sum_{m=1}^{M^e} \int_{C_m^{e+}}^{C_m^{e-}} \omega \left( \frac{\partial \tilde{\Psi}_{b^e}}{\partial s} + H\vec{U}_{(0)} \cdot \hat{n} \right)^2 ds + \\
 &\quad \frac{1}{2} \sum_{m=1}^{M^e} \int_{C_m^e} \omega \left( H\vec{U}_{(0)} \cdot \hat{n} \right)^2 ds \quad (D.3)
 \end{aligned}$$

1174 where the  $+/-$  notation in  $C_m^e$  were defined just after eq. (8). The first series  
 1175 of integrals contains the contributions from the open sections of  $\partial\mathcal{D}^e$  while  
 1176 the second contains the contributions from the external coasts. Variational  
 1177 calculus results in an eq. different from, but similar to, (D.2):

$$\begin{aligned}
 J_{b^e}(\Psi_{b^e} + \delta\Psi_{b^e}) &= J_{b^e}(\Psi_{b^e}) + \frac{1}{2} \sum_{m=1}^{M^e} \int_{C_m^{e+}}^{C_m^{e-}} \omega \left( \frac{\partial \delta\Psi_{b^e}}{\partial s} \right)^2 ds \\
 &\quad - \sum_{m=1}^{M^e} \int_{C_m^{e+}}^{C_m^{e-}} \delta\Psi_{b^e} \frac{\partial}{\partial s} \left[ \omega \left( \frac{\partial \Psi_{b^e}}{\partial s} + H\vec{U}_{(0)} \cdot \hat{n} \right) \right] ds \\
 &\quad - \sum_{m=1}^{M^e} \left[ \omega \left( \frac{\partial \Psi_{b^e}}{\partial s} + H\vec{U}_{(0)} \cdot \hat{n} \right) \right] \Big|_{C_m^{e-}}^{C_m^{e+}} (\delta\Psi_{b^e})|_{C_m^e} \quad (D.4)
 \end{aligned}$$

1178 Here the contributions from the external coasts are all contained in  $J_{b^e}(\Psi_{b^e})$ ,  
 1179 leaving only the open boundaries (the 3 series) affected by the variations  
 1180  $\delta\Psi_{b^e}$ .  $\Psi_{b^e}$  is guaranteed to minimize eq. (6) if the last two series in eq. (D.4)  
 1181 are zero for all permissible  $\delta\Psi_{b^e}$ , resulting in eq. (7&8).

1182 *D.3. Deriving cost function,  $J_{b^u}$ , for optimizing  $\Psi$  along uncertain coasts,*

1183  $C^{\text{iu}}$

1184 The optimization functional,  $J_{b^u}$ , is constructed as the sum of three terms:

$$J_{b^u} \left( \Psi_{C_1^{\text{iu}}}, \dots, \Psi_{C_{N^{\text{iu}}}^{\text{iu}}} \right) = J_{b^u}^{uu} \left( \Psi_{C_1^{\text{iu}}}, \dots, \Psi_{C_{N^{\text{iu}}}^{\text{iu}}} \right) + J_{b^u}^{uc} \left( \Psi_{C_1^{\text{iu}}}, \dots, \Psi_{C_{N^{\text{iu}}}^{\text{iu}}} \right)$$



$$+ J_{b^u}^{uo} \left( \Psi_{C_1^{iu}}, \dots, \Psi_{C_{N^{iu}}^{iu}} \right) \quad (\text{D.5})$$

1185 where  $J_{b^u}^{uu}$  is the optimizing functional for the transport between all pairs  
 1186 of the uncertain coasts,  $J_{b^u}^{uc}$  is the optimizing functional for the transport  
 1187 between all pairs of uncertain and certain coasts and  $J_{b^u}^{uo}$  is the optimizing  
 1188 functional for the transport between each of the uncertain coasts and the open  
 1189 boundaries of the domain (Fig. 13). We introduce the superscript notation  
 1190  $uu$  for functionals and quantities evaluated between pairs of uncertain coasts,  
 1191  $uc$  between uncertain and certain coasts and  $uo$  between uncertain coasts and  
 1192 the open boundaries. The three terms in eq. D.5 are constructed as follows:

- 1193 1. *Constructing  $J_{b^u}^{uu}$* : Let  $C_n^{iu}$  and  $C_m^{iu}$  be two of the coasts in  $\partial\mathcal{D}^{iu}$ .  $\Psi_{(0)}$  is  
 1194 not constrained to be a constant along these coasts. Denoting a point  
 1195  $s$  on  $C_m^{iu}$  by  $s_{iu,m}$ , we find the points  $s_{nm}^{uu}$  and  $s_{mn}^{uu}$  which minimize the  
 1196 transport (as estimated by  $\Psi_{(0)}$ ) between the islands:

$$[s_{nm}^{uu}, s_{mn}^{uu}] = \arg \min_{[s_{iu,n}, s_{iu,m}]} |\Psi_{(0)}(s_{iu,n}) - \Psi_{(0)}(s_{iu,m})|$$

1197 (i.e.  $s_{nm}^{uu}$  is the point along  $C_n^{iu}$  which minimizes the difference in  $\Psi_{(0)}$  be-  
 1198 tween  $C_n^{iu}$  and  $C_m^{iu}$ ). Then, denoting  $\Delta_{nm}^{uu} \Psi_{(0)} = \Psi_{(0)}(s_{nm}^{uu}) - \Psi_{(0)}(s_{mn}^{uu})$ ,  
 1199 the optimization functional for the transport between islands  $n$  and  $m$   
 1200 is chosen to be  $\varpi_{nm}^{uu} (\Psi_{C_n^{iu}} - \Psi_{C_m^{iu}} - \Delta_{nm}^{uu} \Psi_{(0)})^2$  where  $\Psi_{C_n^{iu}}$ ,  $\Psi_{C_m^{iu}}$  are the  
 1201 unknown optimized (constant) values of the transport streamfunction  
 1202 along coasts  $n$  and  $m$  respectively.  $\varpi_{nm}^{uu}$  is a weight applied to the  
 1203 inter-island transport difference in the optimization. The weights are  
 1204 chosen to emphasize the transports between adjacent islands over the  
 1205 transports between widely separated islands (e.g. in figure 1, the trans-  
 1206 port between islands 2 and 3 will be much more heavily weighted than  
 1207 the transport between islands 1 and 3). The details of the weighting  
 1208 function are presented in §3.2.1. Summing these weighted differences  
 1209 over all distinct pairs of islands (and pre-multiplying by  $\frac{1}{2}$ ) results in:

$$J_{b^u}^{uu} \left( \Psi_{C_1^{iu}}, \dots, \Psi_{C_{N^{iu}}^{iu}} \right) = \frac{1}{2} \sum_{n=1}^{N^{iu}} \sum_{m=n+1}^{N^{iu}} \left[ \varpi_{nm}^{uu} (\Psi_{C_n^{iu}} - \Psi_{C_m^{iu}} - \Delta_{nm}^{uu} \Psi_{(0)})^2 \right] \quad (\text{D.6})$$

- 1210
- 1211 2. *Constructing  $J_{b^u}^{uc}$* : Let  $C_k^c$  be one of the coasts in  $\partial\mathcal{D}^c$ ,  $\Psi_{C_k^c}$  be the  
 1212 certain (constant) value of  $\Psi$  along  $C_k^c$  and  $C_n^{iu}$  be a coast in  $\partial\mathcal{D}^{iu}$ .  
 1213 Find the point  $s_{nk}^{uc}$  on  $C_n^{iu}$  which minimizes the transport (as estimated  
 1214 by  $\Psi_{(0)}$ ) between the island and certain coast:

$$s_{nk}^{uc} = \arg \min_{s_{iu,n}} |\Psi_{(0)}(s_{iu,n}) - \Psi_{C_k^c}|$$

1215 and define  $\Delta_{nk}^{uc}\Psi_{(0)} = \Psi_{(0)}(s_{nk}^{uc}) - \Psi_{C_k^c}$ . The optimization functional for  
 1216 the transport between island  $n$  and coast  $k$  is chosen to be  $\varpi_{nk}^{uc}(\Psi_{C_n^{iu}} -$   
 1217  $\Psi_{C_k^c} - \Delta_{nk}^{uc}\Psi_{(0)})^2 = \varpi_{nk}^{uc}(\Psi_{C_n^{iu}} - \Psi_{(0)}(s_{nk}^{uc}))^2$ . Here the certain value  
 1218  $\Psi_{C_k^c}$  cancels out. One side effect of this cancellation is that this func-  
 1219 tional provides a mechanism for the constant of integration selected in  
 1220 constructing  $\Psi_b$  to enter into the optimization (while  $J_{bu}^{uu}$  retains only  
 1221 differences of  $\Psi_{(0)}$ ). As before, the transport differences are weighted  
 1222 by  $\varpi_{nk}^{uc}$ . Summing these weighted differences over all pairs of islands  
 1223 and coasts (and pre-multiplying by  $\frac{1}{2}$ ) results in:

$$J_{bu}^{uc}(\Psi_{C_1^{iu}}, \dots, \Psi_{C_{N^{iu}}^{iu}}) = \frac{1}{2} \sum_{n=1}^{N^{iu}} \sum_{k=1}^{M^c} \left[ \varpi_{nk}^{uc} (\Psi_{C_n^{iu}} - \Psi_{(0)}(s_{nk}^{uc}))^2 \right] \quad (D.7)$$

1224

1225 3. *Constructing  $J_{bu}^{uo}$* : Let  $s_{o,b}$  be a point along the open boundary,  $\partial\mathcal{D}^o$ .  
 1226 Find  $s_{nb}^{uo}$  on  $C_n^{iu}$  and  $s_{bn}^{ou}$  on  $\partial\mathcal{D}^o$  which minimizes the transport (as  
 1227 estimated by  $\Psi_{(0)}$ ) between the island and open boundary:

$$[s_{nb}^{uo}, s_{bn}^{ou}] = \arg \min_{[s_{iu,n}, s_{o,b}]} |\Psi_{(0)}(s_{iu,n}) - \Psi_{(0)}(s_{o,b})| \quad .$$

1228 Then, defining  $\Delta_{nb}^{uo}\Psi_{(0)} = \Psi_{(0)}(s_{nb}^{uo}) - \Psi_{(0)}(s_{bn}^{ou})$ , the optimization func-  
 1229 tional for the transport between the island  $n$  and the open boundary is  
 1230 chosen to be  $\varpi_{nb}^{uo}(\Psi_{C_n^{iu}} - \Psi_{(0)}(s_{bn}^{ou}) - \Delta_{nb}^{uo}\Psi_{(0)})^2 = \varpi_{nb}^{uo}(\Psi_{C_n^{iu}} - \Psi_{(0)}(s_{nb}^{uo}))^2$ .  
 1231 As above, the transport difference is weighted by  $\varpi_{nb}^{uo}$  and the known  
 1232 value of  $\Psi$  along the boundary cancels (providing a second path for  
 1233 information on the constant of integration). Summing these weighted  
 1234 differences over all islands (and pre-multiplying by  $\frac{1}{2}$ ) results in:

$$J_{bu}^{uo}(\Psi_{C_1^{iu}}, \dots, \Psi_{C_{N^{iu}}^{iu}}) = \frac{1}{2} \sum_{n=1}^{N^{iu}} \left[ \varpi_{nb}^{uo} (\Psi_{C_n^{iu}} - \Psi_{(0)}(s_{nb}^{uo}))^2 \right] \quad (D.8)$$

1235 These expressions for  $J_{bu}^{uu}$ ,  $J_{bu}^{uc}$  and  $J_{bu}^{uo}$  are substituted into eq. (D.5),  
 1236 resulting in eq. (14).  $J_{bu}^{uc}$  and  $J_{bu}^{uo}$  provide a pathway for the absolute value  
 1237 of  $\Psi_{be}$  (i.e. the constant of integration) to be included in the optimized  $\Psi_{C^{iu}}$ ,  
 1238 since they are formulated directly in terms of the  $\Psi_{C^{iu}}$ 's. In contrast, the  
 1239 formulation of  $J_{bu}^{uu}$  in terms of differences between the  $\Psi_{C^{iu}}$ 's provides the  
 1240 algorithm robustness to non-localized changes from imposing the  $\Psi_{C^{iu}}$  (i.e.  
 1241 the values along  $C^{iu}$  are allowed to “float” with the changes).

1242 **References**

- 1243 Agarwal, A., May 2009. Statistical Field Estimation and Scale Estimation for Complex Coastal Regions  
1244 and Archipelagos. Master's thesis, Massachusetts Institute of Technology, Department of Mechanical  
1245 Engineering, Cambridge, Massachusetts.
- 1246 Agarwal, A., Lermusiaux, P. F. J., 2011. Statistical field estimation for complex coastal regions and  
1247 archipelagos. *Ocean Modelling* 40 (2), 164–189.
- 1248 Antonov, J. I., Locarnini, R. A., Boyer, T. P., Mishonov, A. V., Garcia, H. E., 2006. World Ocean Atlas  
1249 2005, Volume 2: Salinity. NOAA Atlas NESDIS 62, US Government Printing Office, Washington, DC.,  
1250 S. Levitus (ed.).
- 1251 Artale, V., Calmanti, S., Carillo, A., DellAquila, A., Herrmann, M., Pisacane, G., Ruti, P. M., Sannino, G.,  
1252 Struglia, M. V., Giorgi, F., Bi, X., Pal, J. S., Rauscher, S., 2010. An atmosphere-ocean regional climate  
1253 model for the Mediterranean area: assessment of a present climate simulation. *Climate Dynamics* 35 (5),  
1254 721–740.
- 1255 Balmaseda, M., Anderson, D., 2009. Impact of initialization strategies and observations on seasonal fore-  
1256 cast skill. *Geophysical Research Letters* 36 (1), L01701.
- 1257 Balmaseda, M. A., Vidard, A., Anderson, D. L., 2008. The ECMWF ocean analysis system: ORA-S3.  
1258 *Monthly Weather Review* 136 (8), 3018–3034.
- 1259 Barth, A., Alvera-Azcrate, A., Weisberg, R. H., 2008. Benefit of nesting a regional model into a large-scale  
1260 ocean model instead of climatology. Application to the West Florida Shelf. *Continental Shelf Research*  
1261 28 (4-5), 561 – 573.
- 1262 Bender, M. A., Ginis, I., 2000. Real-case simulations of hurricane-ocean interaction using a high-resolution  
1263 coupled model: Effects on hurricane intensity. *Monthly Weather Review* 128 (4), 917–946.
- 1264 Bennett, A. F., 1992. Inverse methods in physical oceanography. Cambridge University Press.
- 1265 Bennett, A. F., 2002. Inverse modeling of the ocean and atmosphere. Cambridge University Press.
- 1266 Beşiktepe, Ş. T., Lermusiaux, P. F. J., Robinson, A. R., 2003. Coupled physical and biogeochemical data-  
1267 driven simulations of Massachusetts Bay in late summer: real-time and postcruise data assimilation.  
1268 *Journal of Marine Systems* 40-41, 171–212.
- 1269 Bleck, R., 2002. An oceanic general circulation model framed in hybrid isopycnic-Cartesian coordinates.  
1270 *Ocean Modelling* 4 (1), 55–88.
- 1271 Boyer, T. P., Stephens, C., Antonov, J. I., Conkright, M. E., Locarnini, R. A., O'Brien, T. D., Garcia,  
1272 H. E., 2002. World Ocean Atlas 2001 Volume 2: Salinity. NOAA Atlas NESDIS 50, US Government  
1273 Printing Office, Washington, DC., S. Levitus (ed.).
- 1274 Cazes-Boezio, G., Menemenlis, D., Mechoso, C. R., 2008. Impact of ECCO ocean-state estimates on the  
1275 initialization of seasonal climate forecasts. *Journal of Climate* 21 (9), 1929–1947.
- 1276 Chavanne, C., Flament, P., Gurgel, K.-W., 2007. Observations of vortices and vortex rossby waves in the  
1277 lee of an island. In: 18th Congres Francais de Mecanique.  
1278 URL <http://hdl.handle.net/2042/16729>
- 1279 Colin, M., Duda, T., te Raa, L., van Zon, T., Haley, P., Lermusiaux, P., Leslie, W., Mirabito, C., Lam, F.,  
1280 Newhall, A., Lin, Y.-T., Lynch, J., 2013. Time-evolving acoustic propagation modeling in a complex  
1281 ocean environment. In: OCEANS - Bergen, 2013 MTS/IEEE. pp. 1–9.

- 1282 Cossarini, G., Lermusiaux, P. F. J., Solidoro, C., 2009. The Lagoon of Venice Ecosystem: Seasonal Dynam-  
1283 ics and Environmental Guidance with Uncertainty Analyses and Error Subspace Data Assimilation.  
1284 *Journal of Geophysical Research* 114, C0626.
- 1285 Cushman-Roisin, B., Beckers, J.-M., 2010. Introduction to geophysical fluid dynamics: Physical and  
1286 Numerical Aspects. Academic Press.
- 1287 Deleersnijder, E., Legat, V., Lermusiaux, P. F. J., 2010. Multi-scale modelling of coastal, shelf and global  
1288 ocean dynamics. *Ocean Dynamics* 60 (6), 1357–1359.
- 1289 Denaro, F. M., 2003. On the application of the Helmholtz–Hodge decomposition in projection methods for  
1290 incompressible flows with general boundary conditions. *International Journal for Numerical Methods*  
1291 *in Fluids* 43 (1), 43–69.
- 1292 Dijkstra, H. A., Katsman, C. A., 1997. Temporal variability of the wind-driven quasi-geostrophic double  
1293 gyre ocean circulation: Basic bifurcation diagrams. *Geophysical & Astrophysical Fluid Dynamics* 85 (3-  
1294 4), 195–232.
- 1295 Egbert, G. D., Erofeeva, S. Y., 2002. Efficient inverse modeling of barotropic ocean tides. *Journal of*  
1296 *Atmospheric and Oceanic Technology* 19 (2), 183–204.
- 1297 Egbert, G. D., Erofeeva, S. Y., 2013. TPXO8-ATLAS.  
1298 URL <http://volkov.oce.orst.edu/tides/tpxo8.atlas.html>
- 1299 Falkovich, A., Ginis, I., Lord, S., 2005. Ocean data assimilation and initialization procedure for the  
1300 coupled GFDL/URI hurricane prediction system. *Journal of Atmospheric and Oceanic Technology*  
1301 22 (12), 1918–1932.
- 1302 Firing, J., Brainard, R. E., 2004. Ten years of shipboard ADCP measurements along the northwestern  
1303 Hawaiian Islands. Tech. rep., 3rd Scientific Symposium, Honolulu.
- 1304 Gangopadhyay, A., Lermusiaux, P. F., Rosenfeld, L., Robinson, A. R., Calado, L., Kim, H. S., Leslie,  
1305 W. G., Haley, Jr., P. J., 2011. The California Current System: A multiscale overview and the develop-  
1306 ment of a feature-oriented regional modeling system (FORMS). *Dynamics of Atmospheres and Oceans*  
1307 52 (1-2), 131–169, special issue of DAO in honor of Prof. A.R.Robinson.
- 1308 Gangopadhyay, A., Robinson, A. R., Haley, Jr., P. J., Leslie, W. G., Lozano, C. J., Bisagni, J. J., Yu, Z.,  
1309 2003. Feature oriented regional modeling and simulations (FORMS) in the Gulf of Maine and Georges  
1310 Bank. *Continental Shelf Research* 23 (3-4), 317–353.
- 1311 Gangopadhyay, A., Schmidt, A., Agel, L., Schofield, O., Clark, J., 2013. Multiscale forecasting in the  
1312 Western North Atlantic: Sensitivity of model forecast skill to glider data assimilation. *Continental*  
1313 *Shelf Research* 63, S159–S176.
- 1314 Gawarkiewicz, G., Jan, S., Lermusiaux, P. F. J., McClean, J. L., Centurioni, L., Taylor, K., Cornuelle, B.,  
1315 Duda, T. F., Wang, J., Yang, Y. J., Sanford, T., Lien, R.-C., Lee, C., Lee, M.-A., Leslie, W., Haley, Jr.,  
1316 P. J., Niiler, P. P., Gopalakrishnan, G., Velez-Belchi, P., Lee, D.-K., Kim, Y. Y., 2011. Circulation and  
1317 intrusions northeast of Taiwan: Chasing and predicting uncertainty in the cold dome. *Oceanography*  
1318 24 (4), 110–121.
- 1319 Godfrey, J. S., 1989. A Sverdrup model of the depth-integrated flow for the world ocean allowing for island  
1320 circulations. *Geophys. Astrophys. Fluid Dynamics* 45 (1-2), 89–112.
- 1321 Gordon, A. L., Sprintall, J., Ffield, A., 2011. Regional oceanography of the Philippine Archipelago.  
1322 *Oceanography* 24 (1), 15–27.

- 1323 Gordon, A. L., Villanoy, C. L., 2011. Oceanography. Special issue on the Philippine Straits Dynamics  
1324 Experiment. Vol. 24. The Oceanography Society.
- 1325 Haley, Jr., P. J., Agarwal, A., Lermusiaux, P. F. J., 2014. Deriving a methodology for optimizing velocities  
1326 and transports in complex coastal regions and archipelagos. MSEAS Report 19, Massachusetts Institute  
1327 of Technology, Cambridge, MA, USA.
- 1328 Haley, Jr., P. J., Lermusiaux, P. F. J., 2010. Multiscale two-way embedding schemes for free-surface  
1329 primitive equations in the “Multidisciplinary Simulation, Estimation and Assimilation System”. Ocean  
1330 Dynamics 60 (6), 1497–1537.
- 1331 Haley, Jr., P. J., Lermusiaux, P. F. J., Robinson, A. R., Leslie, W. G., Logutov, O., Cossarini, G.,  
1332 Liang, X. S., Moreno, P., Ramp, S. R., Doyle, J. D., Bellingham, J., Chavez, F., Johnston, S., 2009.  
1333 Forecasting and reanalysis in the Monterey Bay/California Current region for the Autonomous Ocean  
1334 Sampling Network-II experiment. Deep Sea Research II 56 (3-5), 127–148.
- 1335 Halliwell, Jr., G. R., Shay, L. K., Brewster, J. K., Teague, W. J., 2011. Evaluation and sensitivity analysis  
1336 of an ocean model response to hurricane Ivan. Mon. Wea. Rev. 139 (3), 921–945.
- 1337 Halliwell, Jr., G. R., Shay, L. K., Jacob, S. D., Smedstad, O. M., Uhlhorn, E. W., 2008. Improving ocean  
1338 model initialization for coupled tropical cyclone forecast models using GODAE nowcasts. Monthly  
1339 Weather Review 136 (7), 2576–2591.
- 1340 Herzfeld, M., Andrewartha, J. R., 2012. A simple, stable and accurate Dirichlet open boundary condition  
1341 for ocean model downscaling. Ocean Modelling 43-44, 1–21.
- 1342 Hurlburt, H. E., Metzger, E. J., Sprintall, J., Riedlinger, S. N., Arnone, R. A., Shinoda, T., Xu, X., 2011.  
1343 Circulation in the Philippine Archipelago simulated by  $1/12^\circ$  and  $1/25^\circ$  global HYCOM and EAS  
1344 NCOM. Oceanography 24 (1), 28–47.
- 1345 Jiang, X., Zhong, Z., Jiang, J., 2009. Upper ocean response of the South China Sea to typhoon Krovanh  
1346 (2003). Dynamics of Atmospheres and Oceans 47 (1), 165–175.
- 1347 Leben, R. R., Born, G. H., Engebret, B. R., 2002. Operational altimeter data processing for mesoscale  
1348 monitoring. Marine Geodesy 25 (1-2), 3–18.
- 1349 Lermusiaux, P. F. J., 2006. Uncertainty estimation and prediction for interdisciplinary ocean dynamics.  
1350 Journal of Computational Physics 217 (1), 176–199.
- 1351 Lermusiaux, P. F. J., 2007. Adaptive modeling, adaptive data assimilation and adaptive sampling. Physica  
1352 D: Nonlinear Phenomena 230 (1), 172–196.
- 1353 Lermusiaux, P. F. J., 2007. Adaptive modeling, adaptive data assimilation and adaptive sampling. Physica  
1354 D 230 (1-2), 172–196.
- 1355 Lermusiaux, P. F. J., Haley, P. J., Leslie, W. G., Agarwal, A., Logutov, O., Burton, L., 2011. Multiscale  
1356 physical and biological dynamics in the Philippines Archipelago: Predictions and processes. Oceanog-  
1357 raphy 24 (1), 70–89.
- 1358 Lermusiaux, P. F. J., Haley, Jr., P. J., Yilmaz, N. K., 2007. Environmental prediction, path planning  
1359 and adaptive sampling-sensing and modeling for efficient ocean monitoring, management and pollution  
1360 control. Sea Technology 48 (9), 35–38.
- 1361 Lermusiaux, P. F. J., Lolla, T., Haley, P. J., Yiğit, K., Ueckermann, M. P., Sondergaard, T., Leslie, W. G.,  
1362 2014. Science of autonomy: Time-optimal path planning and adaptive sampling for swarms of ocean  
1363 vehicles. In: Curtin, T. (Ed.), Springer Handbook of Ocean Engineering: Autonomous Ocean Vehicles,  
1364 Subsystems and Control. Springer-Verlag, Ch. 11, in Press.

- 1365 Lermusiaux, P. F. J., Schröter, J., Danilov, S., Iskandarani, M., Pinarci, N., Westerink, J. J., 2013.  
1366 Multiscale modeling of coastal, shelf, and global ocean dynamics. *Ocean Dynamics* 63 (11-12), 1341–  
1367 1344.
- 1368 Leslie, W. G., Robinson, A. R., Haley, P., Logoutov, O., Moreno, P., Lermusiaux, P. F. J., Coehlo, E.,  
1369 2008. Verification and training of real-time forecasting of multi-scale ocean dynamics for maritime rapid  
1370 environmental assessment. *Journal of Marine Systems* 69 (1-2), 3–16.
- 1371 Li, Z., Chao, Y., McWilliams, J. C., 2006. Computation of the streamfunction and velocity potential for  
1372 limited and irregular domains. *Monthly weather review* 134 (11), 3384–3394.
- 1373 Locarnini, R. A., Mishonov, A. V., Antonov, J. I., Boyer, T. P., Garcia, H. E., 2006. *World Ocean Atlas*  
1374 2005, Volume 1: Temperature. NOAA Atlas NESDIS 61, US Government Printing Office, Washington,  
1375 DC., S. Levitus (ed.).
- 1376 Logutov, O. G., 2008. A multigrid methodology for assimilation of measurements into regional tidal  
1377 models. *Ocean Dynamics* 58 (5-6), 441–460.
- 1378 Logutov, O. G., Lermusiaux, P. F. J., 2008. Inverse barotropic tidal estimation for regional ocean appli-  
1379 cations. *Ocean Modelling* 25 (1-2), 17–34.
- 1380 Lolla, T., Haley, Jr., P. J., Lermusiaux, P. F. J., 2014a. Time-optimal path planning in dynamic flows  
1381 using level set equations: Realistic applications. *Ocean Dynamics* 64 (10), 1399–1417.
- 1382 Lolla, T., Lermusiaux, P. F. J., Ueckermann, M. P., Haley, Jr., P. J., 2014b. Time-optimal path planning  
1383 in dynamic flows using level set equations: Theory and schemes. *Ocean Dynamics* 64 (10), 1373–1397.
- 1384 Lolla, T., Ueckermann, M. P., Yiğit, K., Haley, P. J., Lermusiaux, P. F. J., 2012. Path planning in time  
1385 dependent flow fields using level set methods. In: *IEEE International Conference on Robotics and*  
1386 *Automation (ICRA)*. pp. 166–173.
- 1387 Lorenz, E. N., 1963. Deterministic nonperiodic flow. *Journal of the Atmospheric Sciences* 20 (2), 130–141.
- 1388 Lozano, C. J., Robinson, A. R., Arango, H. G., Gangopadhyay, A., Sloan, Q., Haley, P. J., Anderson, L.,  
1389 Leslie, W., 1996. An interdisciplinary ocean prediction system: Assimilation strategies and structured  
1390 data models. In: Malanotte-Rizzoli, P. (Ed.), *Modern Approaches to Data Assimilation in Ocean*  
1391 *Modeling*. Vol. 61 of Elsevier Oceanography Series. Elsevier, pp. 413–452.
- 1392 Lozier, M. S., Owens, W. B., Curry, R. G., 1995. The climatology of the North Atlantic. *Progress in*  
1393 *Oceanography* 36 (1), 1–44.
- 1394 Lynch, P., 1989. Partitioning the wind in a limited domain. *Monthly weather review* 117 (7), 1492–1500.
- 1395 Marshall, J., Plumb, R. A., 2008. *Atmosphere, Ocean and Climate Dynamics: An Introductory Text*.  
1396 Elsevier Academic Press, London, United Kingdom.
- 1397 Maslowski, W., Marble, D., Walczowski, W., Schauer, U., Clement, J. L., Semtner, A. J., 2004. On  
1398 climatological mass, heat, and salt transports through the Barents Sea and Fram Strait from a pan-  
1399 Arctic coupled ice-ocean model simulation. *Journal of Geophysical Research: Oceans* 109 (C3), C03032.
- 1400 Mason, E., Molemaker, J., Shchepetkin, A. F., Colas, F., McWilliams, J. C., Sangrà, P., 2010. Procedures  
1401 for offline grid nesting in regional ocean models. *Ocean Modelling* 35 (1-2), 1–15.
- 1402 May, P. W., Doyle, J. D., Pullen, J. D., David, L. T., 2011. Two-way coupled atmosphere-ocean modeling  
1403 of the PhilEx Intensive Observational Periods. *Oceanography* 24 (1), 48–57.

- 1404 Moore, A. M., 1991. Data assimilation in a quasi-geostrophic open-ocean model of the Gulf Stream region  
1405 using the adjoint method. *Journal of Physical Oceanography* 21 (3), 398–427.
- 1406 Moore, A. M., Arango, H. G., Broquet, G., Powell, B. S., Weaver, A. T., Zavala-Garay, J., 2011. The  
1407 regional ocean modeling system (roms) 4-dimensional variational data assimilation systems: part i–  
1408 system overview and formulation. *Progress in Oceanography* 91 (1), 34–49.
- 1409 Moore, A. M., Arango, H. G., Di Lorenzo, E., Cornuelle, B. D., Miller, A. J., Neilson, D. J., 2004.  
1410 A comprehensive ocean prediction and analysis system based on the tangent linear and adjoint of a  
1411 regional ocean model. *Ocean Modelling* 7 (1), 227–258.
- 1412 MSEAS group, 2010. MSEAS manual. MSEAS Report 6, Massachusetts Institute of Technology, Cam-  
1413 bridge, MA, USA.
- 1414 Oke, P. R., Allen, J. S., Miller, R. N., Egbert, G. D., Kosro, P. M., 2002. Assimilation of surface velocity  
1415 data into a primitive equation coastal ocean model. *Journal of Geophysical Research: Oceans* 107 (C9),  
1416 5–1–5–25.
- 1417 Onken, R., Álvarez, A., Fernández, V., Vizoso, G., Basterretxea, G., Tintoré, J., Haley, Jr., P., Nacini,  
1418 E., 2008. A forecast experiment in the Balearic Sea. *Journal of Marine Systems* 71 (1-2), 79–98.
- 1419 Phadnis, A., 2013. Uncertainty quantification and prediction for non-autonomous linear and nonlinear  
1420 systems. Master’s thesis, Massachusetts Institute of Technology, Cambridge, MA.
- 1421 Pinardi, N., Allen, I., Demirov, E., Mey, P. D., Korres, G., Lascaratos, A., Traon, P.-Y. L., Maillard, C.,  
1422 Manzella, G., Tziavos, C., 2003. The Mediterranean ocean forecasting system: first phase of imple-  
1423 mentation (1998–2001). *Annales Geophysicae* 21 (1), 3–20.
- 1424 Qiu, B., Koh, D. A., Lumpkin, C., Flament, P., 1997. Existence and formation mechanism of the North  
1425 Hawaiian Ridge Current. *Journal of Physical Oceanography* 27 (3), 431–444.
- 1426 Ramp, S., Lermusiaux, P. F. J., Shulman, I., Chao, Y., Wolf, R. E., Bahr, F. L., 2011. Oceanographic  
1427 and atmospheric conditions on the continental shelf north of the Monterey Bay during August 2006.  
1428 *Dynamics of Atmospheres and Oceans* 52 (1-2), 192–223.
- 1429 Robinson, A., 1996. Physical processes, field estimation and an approach to interdisciplinary ocean mod-  
1430 eling. *Earth-Science Reviews* 40 (1-2), 3–54.
- 1431 Robinson, A. R., 1999. Forecasting and simulating coastal ocean processes and variabilities with the  
1432 Harvard Ocean Prediction System. In: Mooers, C. N. K. (Ed.), *Coastal Ocean Prediction*. Vol. 56 of  
1433 *Coastal and Estuarine Studies*. American Geophysical Union, Washington, D. C., pp. 77–99.
- 1434 Sandery, P. A., Brassington, G. B., Freeman, J., 2011. Adaptive nonlinear dynamical initialization. *Journal*  
1435 *of Geophysical Research: Oceans* (1978–2012) 116 (C1), C01021.
- 1436 Sapsis, T. P., Lermusiaux, P. F. J., 2009. Dynamically orthogonal field equations for continuous stochastic  
1437 dynamical systems. *Physica D* 238 (23-24), 2347–2360.
- 1438 Sapsis, T. P., Lermusiaux, P. F. J., 2012. Dynamical criteria for the evolution of the stochastic dimen-  
1439 sionality in flows with uncertainty. *Physica D* 241 (1), 60–76.
- 1440 Sapsis, T. P., Ueckermann, M. P., Lermusiaux, P. F. J., 2013. Global analysis of Navier–Stokes and  
1441 Boussinesq stochastic flows using dynamical orthogonality. *Journal of Fluid Mechanics* 734, 83–113.
- 1442 Schiller, A., Oke, P. R., Brassington, G., Entel, M., Fiedler, R., Griffin, D. A., Mansbridge, J., 2008.  
1443 Eddy-resolving ocean circulation in the Asian-Australian region inferred from an ocean reanalysis  
1444 effort. *Progress in Oceanography* 76 (3), 334 – 365.

- 1445 Schmidt, A., Gangopadhyay, A., 2013. An operational ocean circulation prediction system for the western  
1446 North Atlantic: hindcasting during July-September of 2006. *Continental Shelf Research* 63, S177–S192.
- 1447 Sethian, J. A., 1996. A fast marching level set method for monotonically advancing fronts. *Proceedings of*  
1448 *the National Academy of Sciences* 93 (4), 1591–1595.
- 1449 Sethian, J. A., 1999. *Level Set Methods and Fast Marching Method*. Cambridge University Press, Cam-  
1450 bridge, United Kingdom.
- 1451 Simonnet, E., Dijkstra, H. A., Ghil, M., 2009. Bifurcation analysis of ocean, atmosphere, and climate  
1452 models. In: Temam, R., Tribbia, J., Ciarlet, P. G. (Eds.), *Computational Methods for the Ocean and*  
1453 *the Atmosphere*. Vol. 14 of *Handbook of Numerical Analysis*. Elsevier, pp. 187–229.
- 1454 Sondergaard, T., Lermusiaux, P. F. J., 2013a. Data assimilation with Gaussian Mixture Models using the  
1455 Dynamically Orthogonal field equations. Part I: Theory and scheme. *Monthly Weather Review* 141 (6),  
1456 1737–1760.
- 1457 Sondergaard, T., Lermusiaux, P. F. J., 2013b. Data assimilation with Gaussian Mixture Models using  
1458 the Dynamically Orthogonal field equations. Part II: Applications. *Monthly Weather Review* 141 (6),  
1459 1761–1785.
- 1460 Stephens, C., Antonov, J. I., Boyer, T. P., Conkright, M. E., Locarnini, R. A., O'Brien, T. D., Gar-  
1461 cia, H. E., 2002. *World Ocean Atlas 2001 Volume 1: Temperature*. NOAA Atlas NESDIS 49, US  
1462 Government Printing Office, Washington, DC., S. Levitus (ed.).
- 1463 Timmermann, R., Goosse, H., Madec, G., Fichefet, T., Etche, C., Duliere, V., 2005. On the representation  
1464 of high latitude processes in the ORCA-LIM global coupled sea ice–ocean model. *Ocean Modelling*  
1465 8 (1), 175–201.
- 1466 Ueckermann, M. P., Lermusiaux, P. F. J., 2010. High order schemes for 2D unsteady biogeochemical ocean  
1467 models. *Ocean Dynamics* 60 (6), 1415–1445.
- 1468 Ueckermann, M. P., Lermusiaux, P. F. J., 2014. Hybrid discontinuous Galerkin methods for Boussinesq  
1469 flows. Submitted.
- 1470 Ueckermann, M. P., Lermusiaux, P. F. J., Sapsis, T. P., 2013. Numerical schemes for Dynamically Orthog-  
1471 onal equations of stochastic fluid and ocean flows. *Journal of Computational Physics* 233, 272–294.
- 1472 Wunsch, C., 1996. *The Ocean Circulation Inverse Problem*. Cambridge University Press, Cambridge,  
1473 United Kingdom.
- 1474 Xu, J., Lermusiaux, P. F. J., Haley, P. J., Leslie, W. G., Logoutov, O. G., 2008. Spatial and temporal vari-  
1475 ations in acoustic propagation during the PLUSNet07 exercise in Dabob Bay. *Proceedings of Meetings*  
1476 *on Acoustics (POMA)*, 155th Meeting Acoustical Society of America 4, 070001.
- 1477 Yablonsky, R. M., Ginis, I., 2008. Improving the ocean initialization of coupled hurricane-ocean models  
1478 using feature-based data assimilation. *Monthly Weather Review* 136 (7), 2592–2607.
- 1479 Zhang, J., Steele, M., 2007. Effect of vertical mixing on the Atlantic Water layer circulation in the Arctic  
1480 Ocean. *Journal of Geophysical Research: Oceans* (1978–2012) 112 (C4).



---

**(1)** Input data and models for computing velocity

**(2)** (§2.1) Compute first-guess velocity  $\vec{u}_{(0)}$

- Use data and reduced models to estimate velocity e.g. thermal wind
- Enforce direct bathymetry strong constraints, e.g. zero flow below bathymetry, compute consistent  $\vec{u}_{(0)}$

**(3)** (§2.2) Geometry constraints: Best-fit  $\vec{u}_{(0)}$  level-by-level, enforcing coastline strong constraints

- Best fit 3D velocities, enforcing no-normal flow through coastlines.
  - Propagate interior data to uncertain BCs (island-free) table 2a, eq. (11) in §3.1
  - Best fit external BCs (interpolate for nesting) (island-free) table 2a, eq. (10) in §3.1
  - Best fit internal island BCs, solving weak-constraint optimization table 2a, eqs. (12, 15) in §3.2
  - Combine all BCs and best-fit no-normal flow velocity table 2a, eqs. (5, 16) in §3.1  
 $\vec{u}_{(1)} = \hat{k} \times \nabla \psi$  eq. (4)
- To retain 3D effects or more complex bathymetry constraints, solve for corrector velocity appendix B  
 $\vec{u}_{(2)} = \vec{u}_{(1)} + \nabla \phi$  eq. (B.16)
- Compute first-guess sub-tidal transports from the resultant geometry-constrained velocity.  

$$\vec{U}_{(0)} = \begin{cases} \int_{-H}^0 \vec{u}_{(2)} dz & \text{if 3D constraints} \\ \int_{-H}^0 \vec{u}_{(1)} dz & \text{otherwise} \end{cases}$$
 eq. (1)

**(4)** (§2.3) Sub-tidal transport strong constraints: best-fit transport in (complex)-domain, enforcing non-divergence

- Best fit non-divergent transport to  $H\vec{U}_{(0)}$  obtained in §2.2 and other transport data
  - Propagate interior data to uncertain BCs (island-free) table 2b, eq. (11) in §3.1
  - Best fit external BCs (interpolate for nesting) (island-free) table 2b, eq. (10) in §3.1
  - Best fit internal island BCs, solving weak-constraint optimization tables 2b, eqs. (12, 15) in §3.2
  - Combine all BCs and best-fit non-divergent transport preserving no-normal flow table 2b, eqs. (5, 16) in §3.1  
 $H\vec{U}_{(1)} = \hat{k} \times \nabla \Psi$  eq. (3)

**(5)** (§C.1) Solve for sub-tidal free surface  $\eta_{(0)}$

e.g.,  $\eta_{(0)}$  from HL10 eq. (68)  

$$\vec{U}_{(2)} = \frac{H}{H+\eta_{(0)}} \vec{U}_{(1)}$$
 eq. (C.1)

**(6)** (§C.2) Superimpose tides  $\eta_{tide}$  and  $\vec{U}_{tide}$ , preserving divergence and no-normal flow strong constraints

$\eta_{(1)} = \eta_{(0)} + \eta_{tide}$  eq. (C.2)  
 $\vec{U}_{(3)}$  from eq. (C.3)  
 $\vec{u}'$  from eq. (C.4)  
 $\vec{u} = \vec{u}' + \vec{U}_{(3)}$  eq. (C.5)  
 $w = -\int_{-H}^z \nabla \cdot \vec{u} d\zeta - (\vec{u} \cdot \nabla H)|_{z=-H}$  eq. (C.6)

---

Table 1: Summary of the six steps of our scheme to initialize velocity and transport for PE simulations in complex geometries (multiply-connected domains). Table is presented in the order the operations are performed. Repeat steps 1-6 for nested sub-domains.

Table 2a: Algorithm for 3D velocity

Propagate interior data to boundaries (eq. 11)	$\nabla \cdot (\omega \nabla \psi_{(-1)}) = [\nabla \times (\omega \vec{u}_{(0)})] \cdot \hat{k}$ $\psi_{(-1)} _{C^{1\text{cst}}} = \psi_{C^{1\text{cst}}}$
<ul style="list-style-type: none"> <li>in 2<sup>nd</sup> BC, <math>\partial^2 \psi_{(-1)} / \partial n \partial t</math> is a simple weak OBC, conserving the normal advective flux (locally maintained streamfunction). Other good choices are possible.</li> <li>(11) not needed for downscaling or “certain boundaries”</li> </ul>	<p>and either</p> $\nabla \psi_{(-1)} \cdot \hat{n} _{\partial \mathcal{D}} = -\hat{k} \times \vec{u}_{(0)} \cdot \hat{n} _{\partial \mathcal{D}}$ <p>or zero wt &amp; weak OBC</p> $\omega _{\partial \mathcal{D}} = 0 \quad \& \quad \frac{\partial \omega \cdot \hat{n}}{\partial n} _{\partial \mathcal{D}} = \frac{\partial^2 \psi_{(-1)}}{\partial n \partial t} _{\partial \mathcal{D}} = 0$ <p>recompute: <math>\vec{u}_{(0)} = \hat{k} \times \nabla \psi_{(-1)}</math></p>
Construct exterior BCs (optimize $J_b$ , eq. 10) using either original $\vec{u}_{(0)}$ or recomputed $\vec{u}_{(0)}$ above (for nesting, interpolate $\psi_{b^e}$ from larger domain)	$-\frac{\partial}{\partial s} \left( \omega \frac{\partial \psi_{b^e}}{\partial s} \right) = \frac{\partial}{\partial s} (\omega \vec{u}_{(0)} \cdot \hat{n}) \quad \text{along open boundaries}$ $-\left( \omega \frac{\partial \psi_{b^e}}{\partial s} \right) \Big _{C_m^{e+}} = (\omega \vec{u}_{(0)} \cdot \hat{n}) \Big _{C_m^{e+}} \quad \text{at unknown coasts } \{C_m^e\}$ $\psi_{b^e} \Big _{C_m^{e-}} = 0 \quad \text{at unknown coasts } \{C_m^e\}$ $\psi_{b^e} \Big _{C_k^e} = \psi_{C_k^e} \quad \text{at known coasts } \{C_k^e\}$
Construct “certain coast” solution (eq. 12) using $\psi_{b^e}$ from above	$\nabla \cdot (\omega \nabla \psi_{(0)}) = [\nabla \times (\omega \vec{u}_{(0)})] \cdot \hat{k}$ $\psi_{(0)} _{\partial \mathcal{D}^e} = \psi_{b^e} \equiv \begin{cases} \psi_{b^e} & \text{if } s \in \partial \mathcal{D}^e \\ \psi_{C_k^{\text{ic}}} & \text{if } s \in C_k^{\text{ic}} \end{cases}$
Construct interior island BCs (optimize $J_{b^u}$ , eq. 15) using $\psi_{(0)}$ from above	$\left[ \sum_{\substack{m=1 \\ m \neq n}}^{N^{iu}} \varpi_{nm}^{uu} + \sum_{k=1}^{M^c} \varpi_{nk}^{\text{uc}} + \varpi_{nb}^{\text{uo}} \right] \psi_{C_n^{\text{iu}}} - \sum_{\substack{m=1 \\ m \neq n}}^{N^{iu}} \varpi_{nm}^{\text{uu}} \psi_{C_m^{\text{iu}}} =$ $\sum_{\substack{m=1 \\ m \neq n}}^{N^{iu}} \varpi_{nm}^{\text{uu}} \Delta_{nm}^{uu} \psi_{(0)} + \sum_{k=1}^{M^c} \varpi_{nk}^{\text{uc}} \psi_{(0)}(s_{nk}^{\text{uc}}) + \varpi_{nb}^{\text{uo}} \psi_{(0)}(s_{nb}^{\text{uo}})$
Solve full problem (optimize $J$ , eqs. 5, 16) using $\psi_{b^e}$ and $\psi_{C_n^{\text{iu}}}$ from above	$\nabla \cdot (\omega \nabla \psi) = [\nabla \times (\omega \vec{u}_{(0)})] \cdot \hat{k}$ $\psi _{\partial \mathcal{D}} = \psi_b \equiv \begin{cases} \psi_{b^e} & \text{if } s \in \partial \mathcal{D}^e \\ \psi_{C_k^{\text{ic}}} & \text{if } s \in C_k^{\text{ic}} \\ \psi_{C_n^{\text{iu}}} & \text{if } s \in C_n^{\text{iu}} \end{cases}$

Table 2: Summary of algorithm (§3) for computing the: (a) 3D velocity (level-by-level  $\vec{u}$  and then  $w$  from eq. (C.6)); and (b) transport. Both are optimized for domains with complex geometries including islands. Intermediate transports/velocities can be computed from the intermediate streamfunctions, but are not needed for the algorithm.

Table 2b: Algorithm for transport

Propagate interior data to boundaries (eq. 11)	$\nabla \cdot (\omega \nabla \Psi_{(-1)}) = \left[ \nabla \times (\omega H \vec{U}_{(0)}) \right] \cdot \hat{k}$ $\Psi_{(-1)} _{C^{1\text{cst}}} = \Psi_{C^{1\text{cst}}}$
<ul style="list-style-type: none"> <li>in 2<sup>nd</sup> BC, <math>\partial^2 \Psi_{(-1)} / \partial n \partial t = 0</math> is a simple weak OBC, conserving the normal advective flux (locally maintained transport). Other good choices are possible.</li> <li>(11) not needed for downscaling or “certain boundaries”</li> </ul>	<p>and either</p> $\nabla \Psi_{(-1)} \cdot \hat{n} _{\partial \mathcal{D}} = -\hat{k} \times H \vec{U}_{(0)} \cdot \hat{n} _{\partial \mathcal{D}}$ <p>or zero wt &amp; weak OBC</p> $\omega _{\partial \mathcal{D}} = 0 \quad \& \quad \frac{\partial H U \cdot \hat{n}}{\partial n} _{\partial \mathcal{D}} = \frac{\partial^2 \Psi_{(-1)}}{\partial n \partial t} _{\partial \mathcal{D}} = 0$ <p>recompute: <math>H \vec{U}_{(0)} = \hat{k} \times \nabla \Psi_{(-1)}</math></p>
Construct exterior BCs (optimize $J_b$ , eq. 10) using either original $\vec{U}_{(0)}$ or recomputed $\vec{U}_{(0)}$ above (for nesting, interpolate $\Psi_{b^e}$ from larger domain)	$-\frac{\partial}{\partial s} \left( \omega \frac{\partial \Psi_{b^e}}{\partial s} \right) = \frac{\partial}{\partial s} \left( \omega H \vec{U}_{(0)} \cdot \hat{n} \right) \quad \text{along open boundaries}$ $-\left( \omega \frac{\partial \Psi_{b^e}}{\partial s} \right) \Big _{C_m^{e+}} = \left( \omega H \vec{U}_{(0)} \cdot \hat{n} \right) \Big _{C_m^{e+}} \quad \text{at unknown coasts } \{C_m^e\}$ $-\left( \omega \frac{\partial \Psi_{b^e}}{\partial s} \right) \Big _{C_m^{e-}} = \left( \omega H \vec{U}_{(0)} \cdot \hat{n} \right) \Big _{C_m^{e-}} \quad \text{at unknown coasts } \{C_m^e\}$ $\Psi_{b^e} \Big _{C_m^{e+}} = 0 \quad \text{at unknown coasts } \{C_m^e\}$ $\Psi_{b^e} \Big _{C_k^e} = \Psi_{C_k^e} \quad \text{at known coasts } \{C_k^e\}$
Construct “certain coast” solution (eq. 12) using $\Psi_{b^e}$ from above	$\nabla \cdot (\omega \nabla \Psi_{(0)}) = \left[ \nabla \times (\omega H \vec{U}_{(0)}) \right] \cdot \hat{k}$ $\Psi_{(0)} _{\partial \mathcal{D}^e} = \Psi_{b^e} \equiv \begin{cases} \Psi_{b^e} & \text{if } s \in \partial \mathcal{D}^e \\ \Psi_{C_k^{\text{ic}}} & \text{if } s \in C_k^{\text{ic}} \end{cases}$
Construct interior island BCs (optimize $J_{b^u}$ , eq. 15) using $\Psi_{(0)}$ from above	$\left[ \sum_{\substack{m=1 \\ m \neq n}}^{N^{iu}} \varpi_{nm}^{uu} + \sum_{k=1}^{M^c} \varpi_{nk}^{\text{uc}} + \varpi_{nb}^{\text{uo}} \right] \Psi_{C_n^{\text{iu}}} - \sum_{\substack{m=1 \\ m \neq n}}^{N^{iu}} \varpi_{nm}^{\text{uu}} \Psi_{C_m^{\text{iu}}} =$ $\sum_{\substack{m=1 \\ m \neq n}}^{N^{iu}} \varpi_{nm}^{\text{uu}} \Delta_{nm}^{uu} \Psi_{(0)} + \sum_{k=1}^{M^c} \varpi_{nk}^{\text{uc}} \Psi_{(0)}(s_{nk}^{\text{uc}}) + \varpi_{nb}^{\text{uo}} \Psi_{(0)}(s_{nb}^{\text{uo}})$
Solve full problem (optimize $J$ , eqs. 5, 16) using $\Psi_{b^e}$ and $\Psi_{C_n^{\text{iu}}}$ from above	$\nabla \cdot (\omega \nabla \Psi) = \left[ \nabla \times (\omega H \vec{U}_{(0)}) \right] \cdot \hat{k}$ $\Psi _{\partial \mathcal{D}} = \Psi_b \equiv \begin{cases} \Psi_{b^e} & \text{if } s \in \partial \mathcal{D}^e \\ \Psi_{C_k^{\text{ic}}} & \text{if } s \in C_k^{\text{ic}} \\ \Psi_{C_n^{\text{iu}}} & \text{if } s \in C_n^{\text{iu}} \end{cases}$

Table 2: (continued)

Weights for imposing inter-island transports	Westward Transports (Sv)	
	Dipolog	Surigao
--	-1.1	-0.63
$\varpi_{nm}^{uu}$	-0.60	-0.20
10 $\varpi_{nm}^{uu}$	-0.18	0.26
100 $\varpi_{nm}^{uu}$	0.34	0.30
1000 $\varpi_{nm}^{uu}$	0.48	0.30
10000 $\varpi_{nm}^{uu}$	0.50	0.30

Table 3: Testing weights for imposing inter-island transports. Our island optimization scheme is employed with the imposition of inter-island transports, eq. (17). Here, we impose westward transports of 0.5 Sv through the Dipolog Strait and 0.3 Sv through the Surigao Strait. The resulting transports from calculations using different weights are compared to the default values,  $\varpi_{nm}^{uu} = (\mathcal{A}_{global\ min}/\mathcal{A}_{nm})^2$ . For Dipolog  $\varpi_{nm}^{uu} = 2.19 \times 10^{-3}$  while for Surigao  $\varpi_{nm}^{uu} = 2.29 \times 10^{-2}$ .

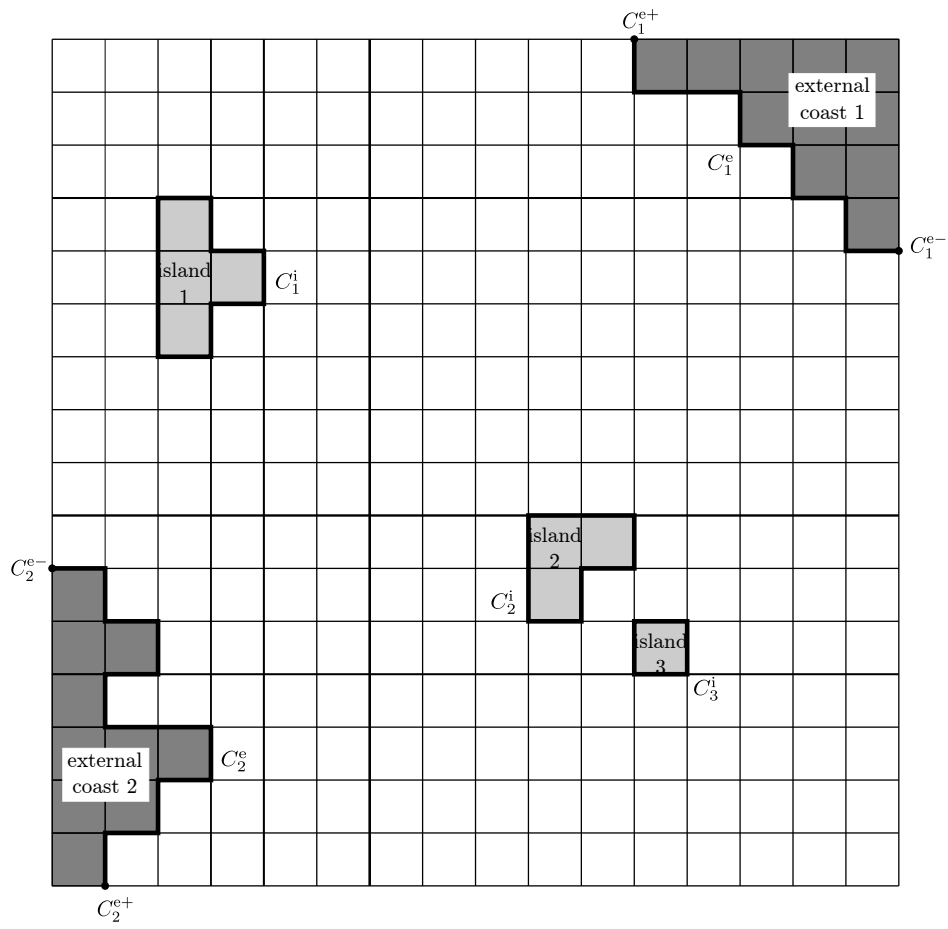


Figure 1: Canonical computational domain, highlighting the different types of landforms and coasts.

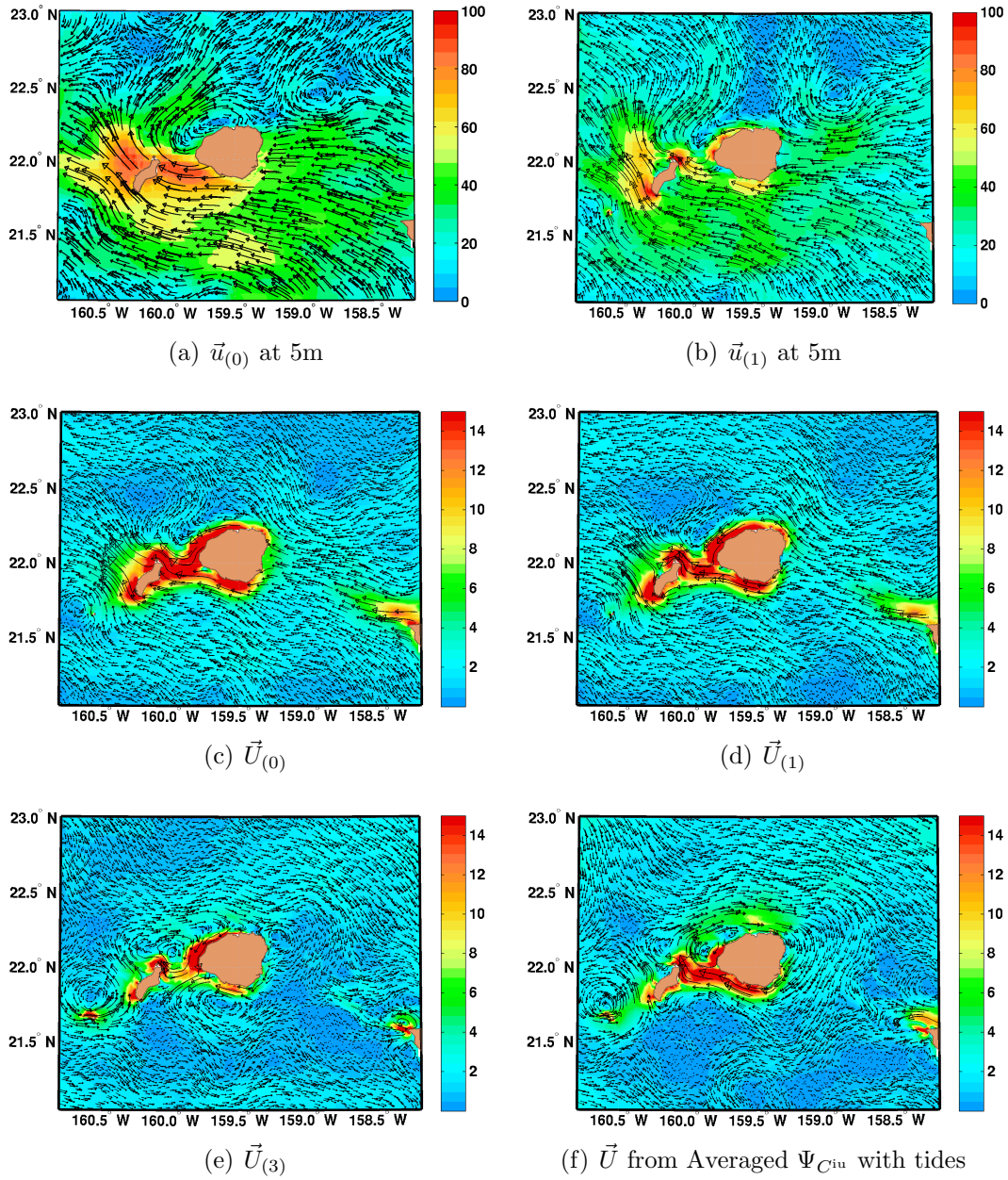


Figure 2: Illustrating the steps in optimizing velocities and transports. (a) First guess velocity field on flat levels. (b) Applying level-by-level coastal/bathymetric constraints on flat levels. (c) Resulting first guess transport (after interpolation to terrain-follow grid). (d) Applying coastal/bathymetric constraints to transport. (e) Superimposing tides. This is the final IC estimate, result of our optimization. (f) IC obtained using averaging to impose no-normal flow, shown for comparison.

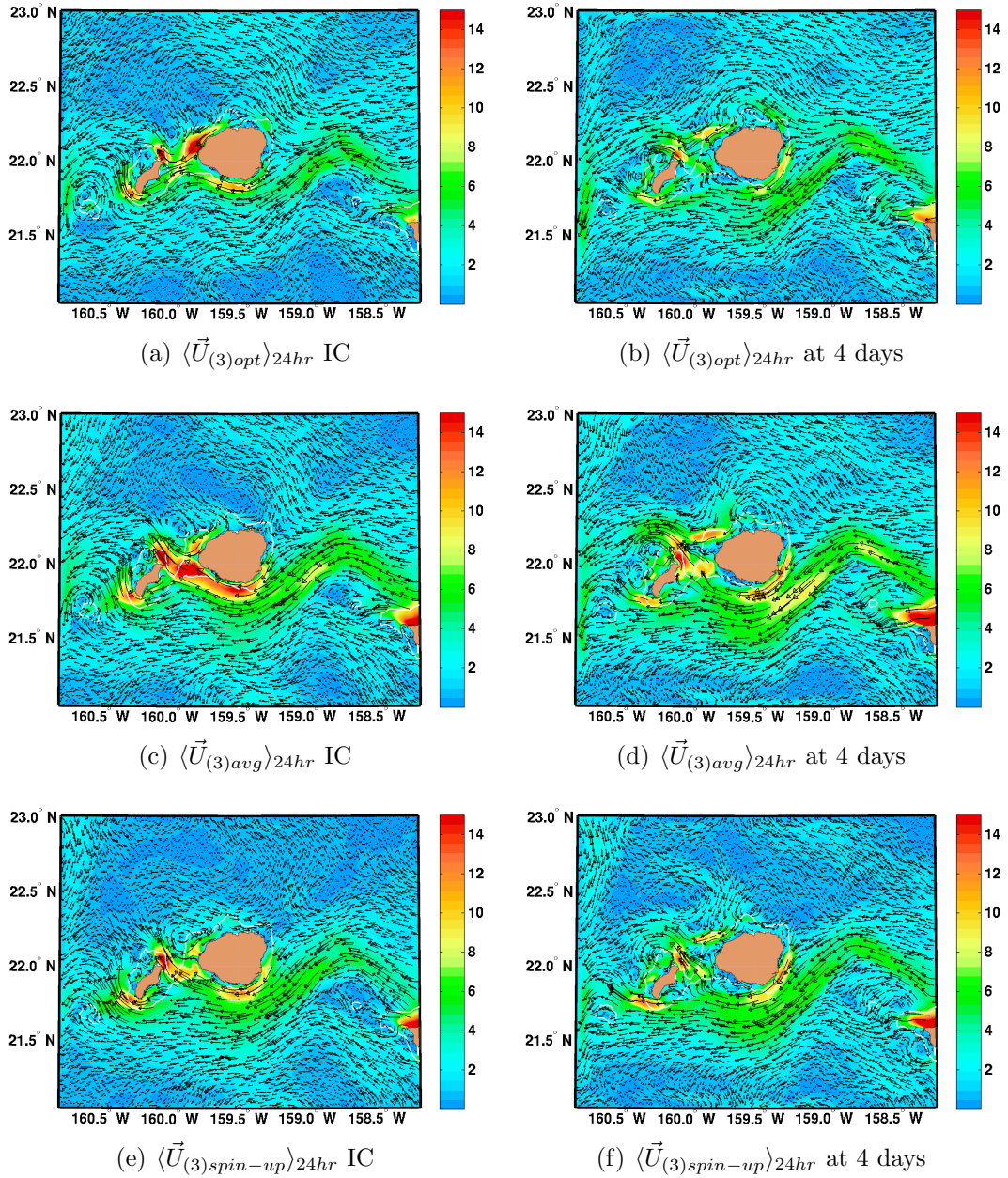


Figure 3: Comparing 24 hr-averaged velocity,  $\langle \vec{U} \rangle_{24hr}$ , from 3 simulations (at initial time and after 4 days). (a),(b) Simulation from optimized ICs. (c),(d) Simulation from ICs using averaged  $\Psi_{Ciu}$ . (e),(f) Simulation from spin-up ICs. Both averaged and spin-up ICs over-estimate transport between islands of Kauai and Niihau.

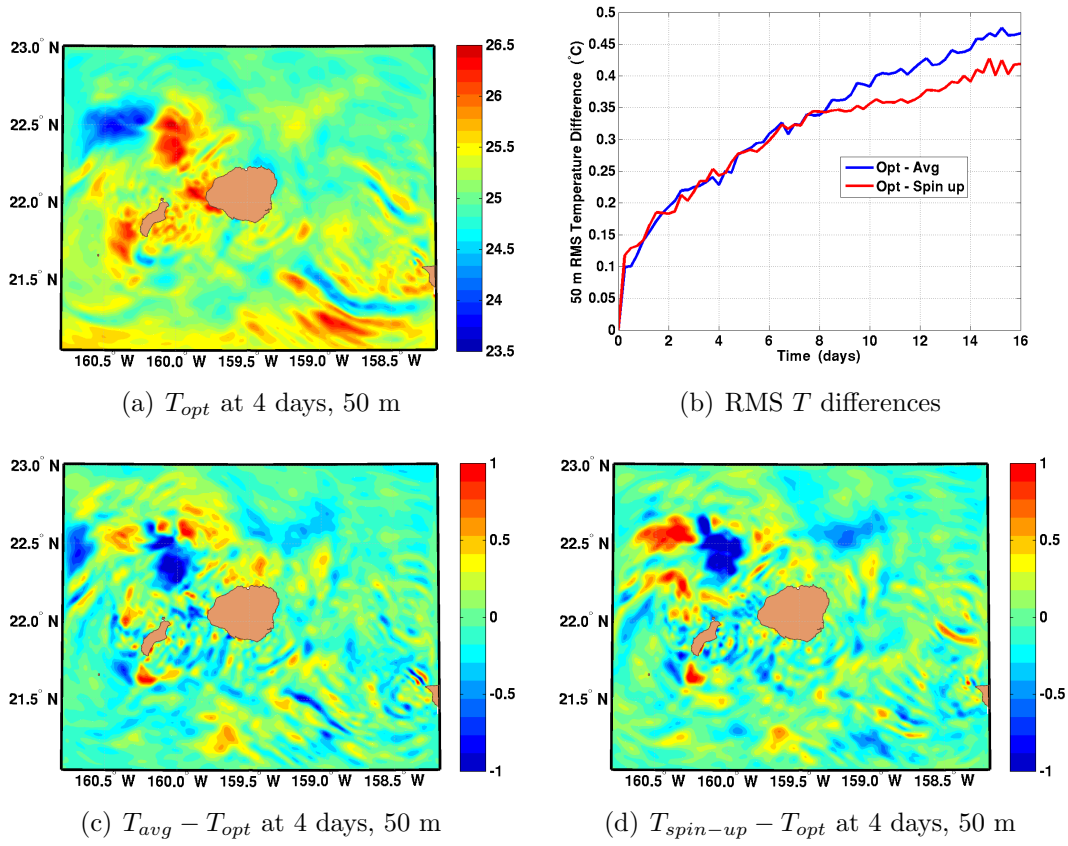
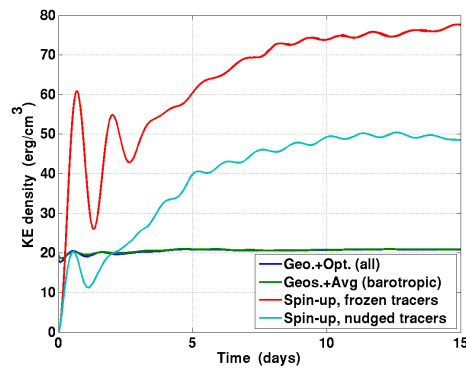
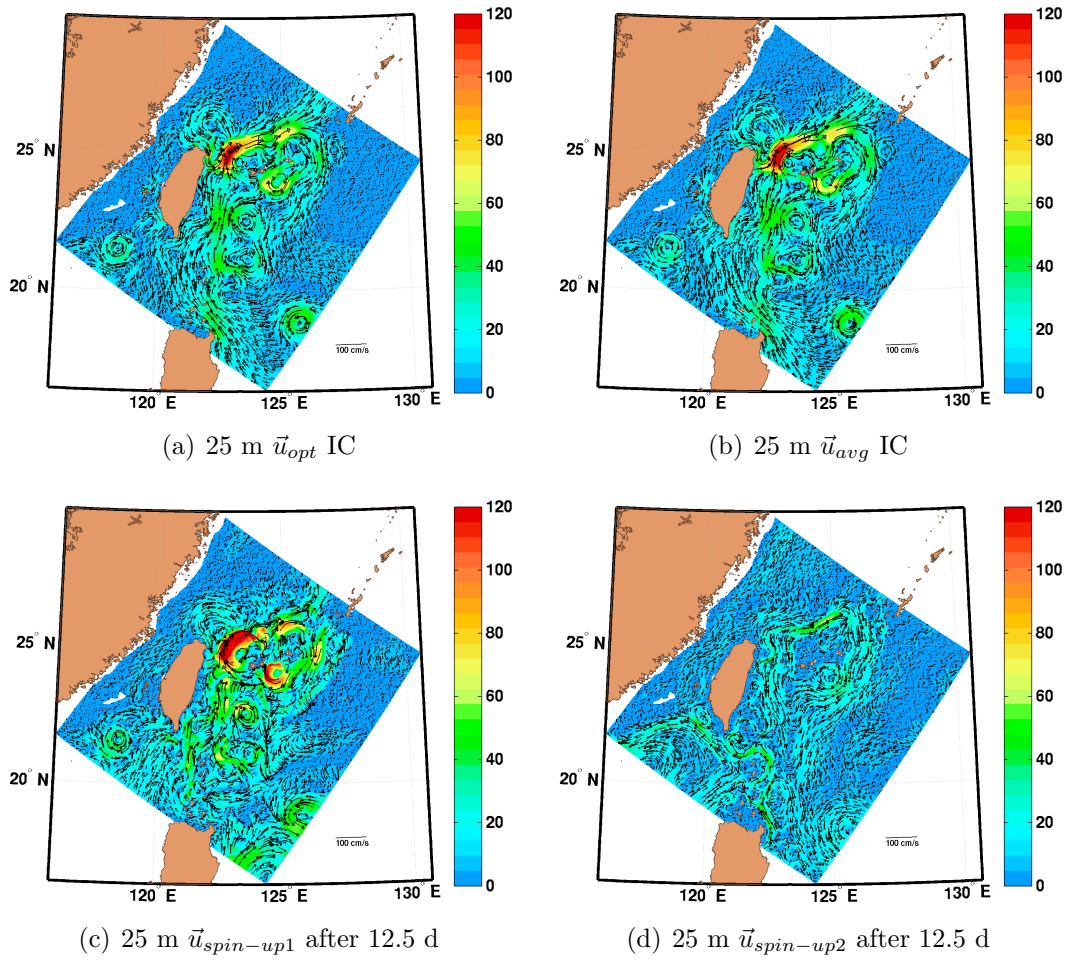


Figure 4: Comparing temperature at 50 m from the same 3 simulations as on Fig. 3. (a) Simulation from optimized ICs. (b) Time history of RMS differences between simulations. (c) Simulation from ICs using averaged  $\Psi_{C^{iu}}$ . (d) Simulation from spin-up ICs. The erroneous transports of the averaged and spin-up ICs (Fig. 3) have led to growing differences in the tracer fields throughout the 2 week simulations.





(e) KE per unit volume for runs (a)-(d)

Figure 5: Subtidal velocity adjustment. (a) Initial velocity at 25 m, from geostrophy and optimization between islands. (b) Initial velocity at 25 m from geostrophy and averaging of island BCs for barotropic mode only. Without level-by-level optimization, initial velocities enter coasts, e.g.: southern end of Taiwan, Luzon and neighboring islands, and islands along Ilan ridge. (c) Spin-up from zero holding tracers constant. (d) Spin-up from zero but with nudging tracers at open boundaries to ICs. (e) KE per unit volume for runs initialized from (a),(b) and spin up runs (c),(d). KE relatively uniform for ICs from geostrophy. Although KE stabilized in all runs, spin-up simulations still have not developed a Kuroshio.

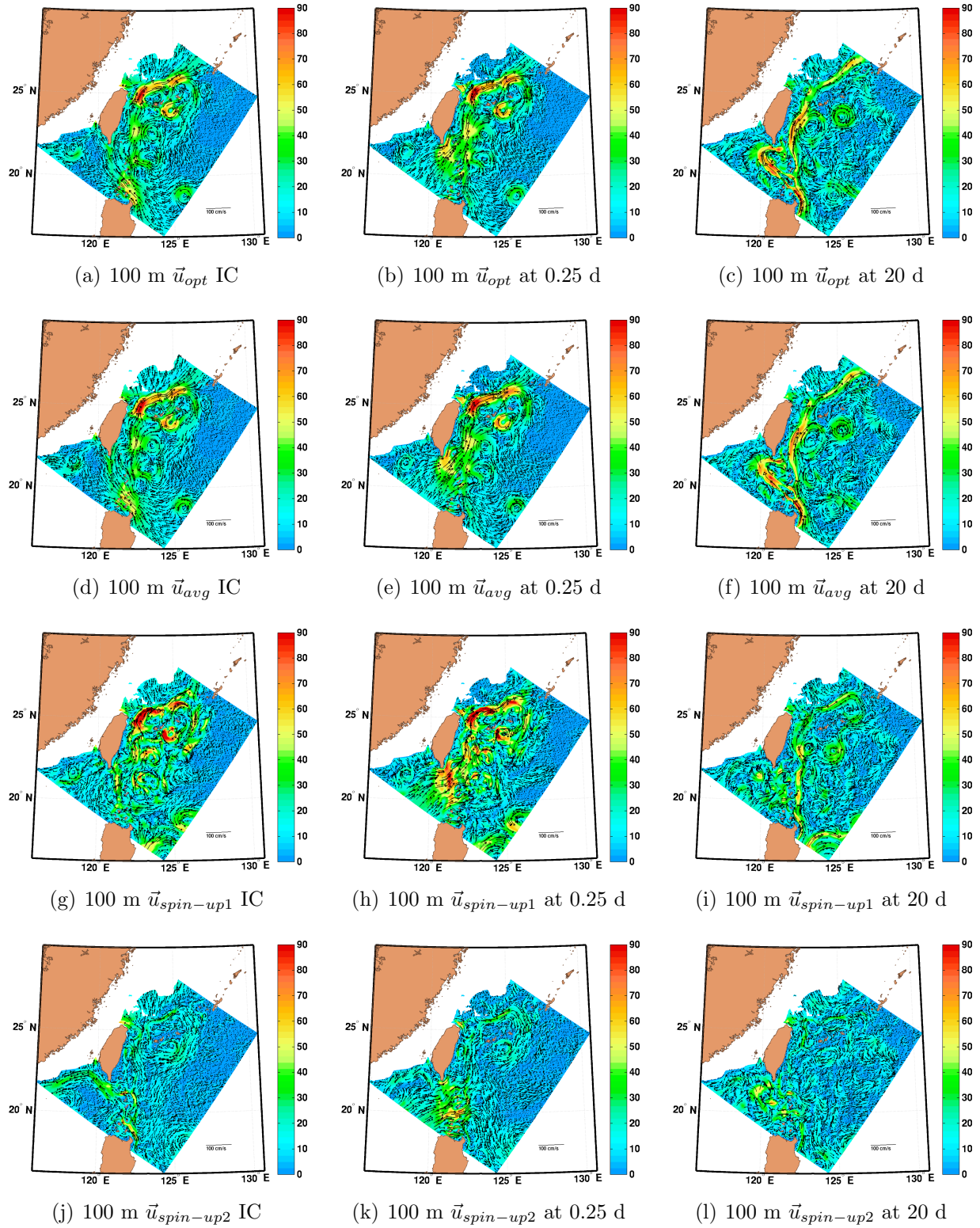


Figure 6: Comparing 100 m velocity fields from simulations (horizontally: at initial time, after 0.25 day and after 20 days) initialized from four different ICs. (a)-(c) Optimized ICs. (d)-(f) Averaged  $\Psi_{C^{in}}$  ICs. (g)-(i) Spin-up (frozen tracer) ICs. (j)-(l) Spin-up (nudged tracer) ICs. Results include: the two reduced physics, optimized and averaged, ICs better maintain Kuroshio; Simulation from spin-up using nudged tracers is losing its Kuroshio.

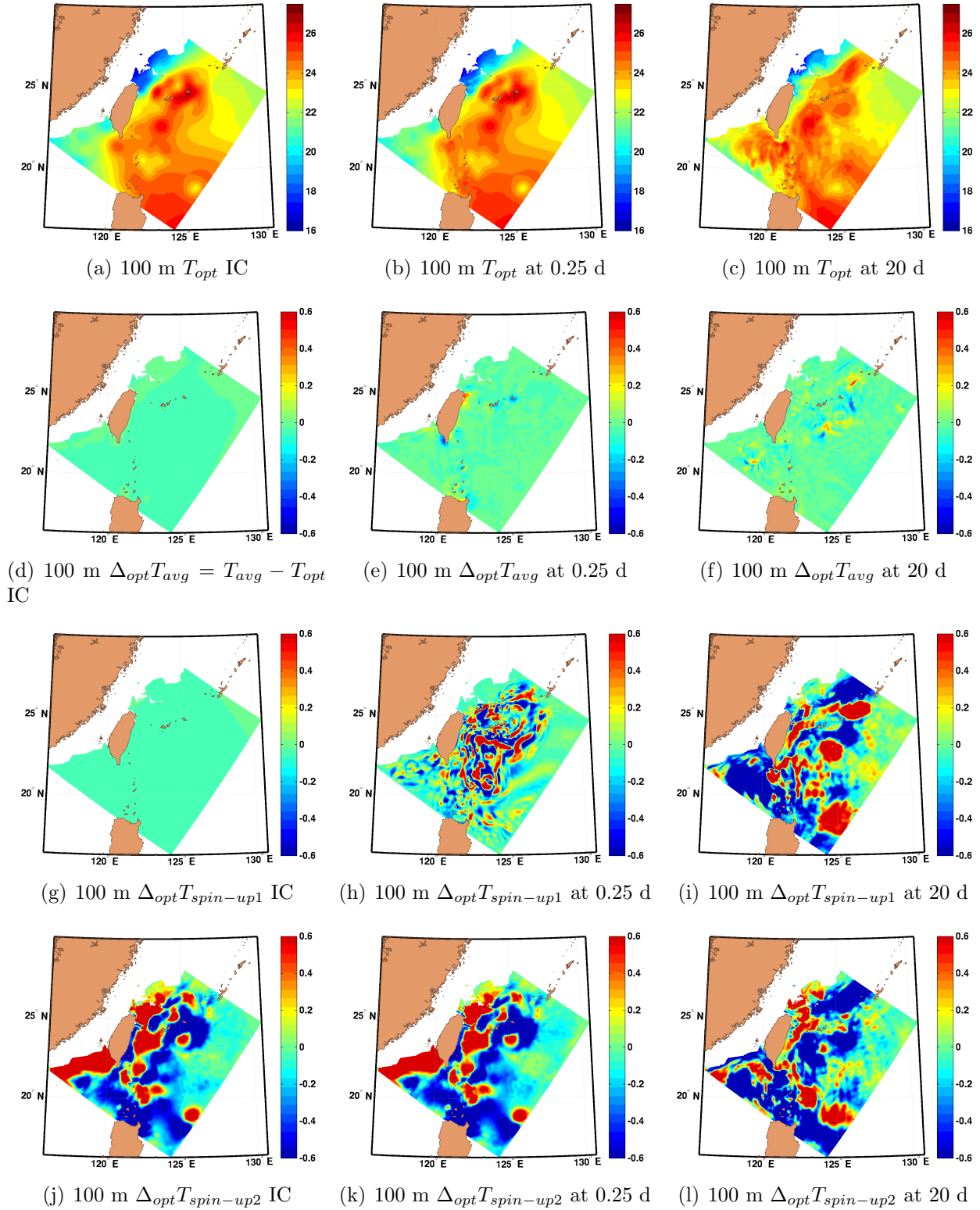
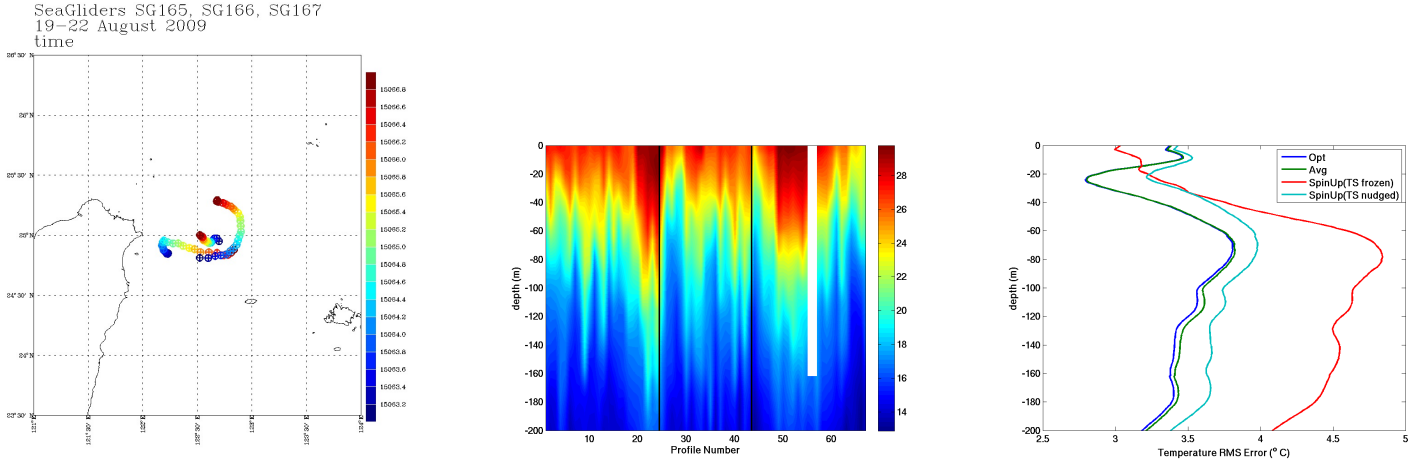
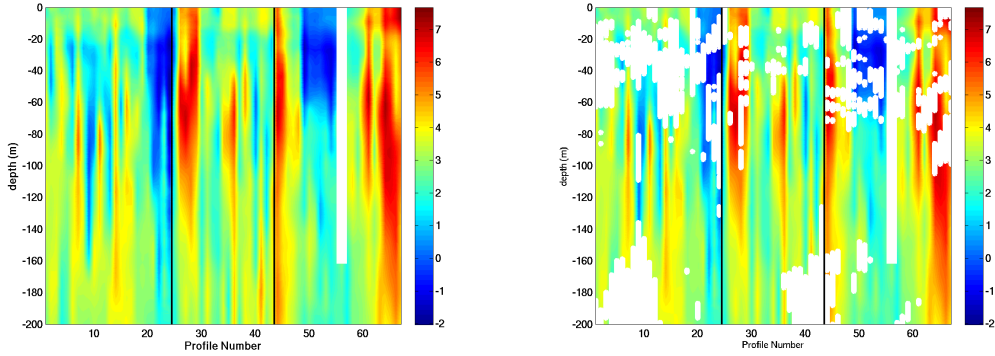


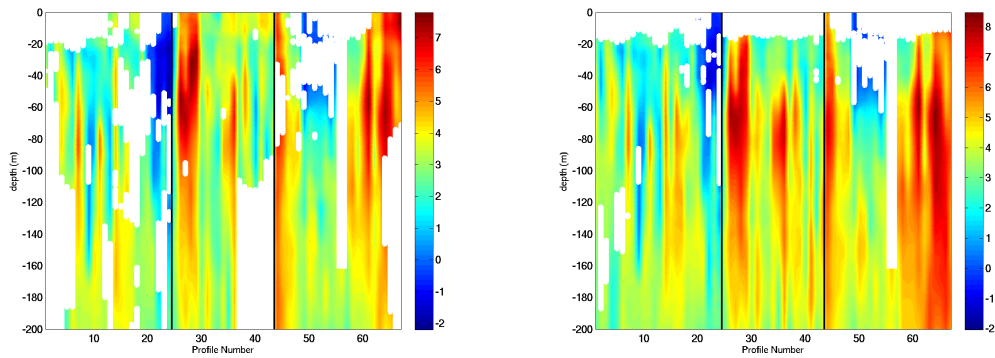
Figure 7: As for Fig. 6, but comparing the 100 m temperature fields. Results include: adjustment differences between hindcasts with optimized and averaged ICs appear by 0.25 day off northern coast of Taiwan and advect into Kuroshio; much larger differences 1–2 °C between optimized and spin-up hindcasts. Errors continue to grow throughout the 20 simulation days



(a) Sea glider positions colored by time (b) Glider  $T$  data cross sections along SG165, SG166, SG167 (separated by black lines) (c) RMS  $T$  errors for 4 hindcasts

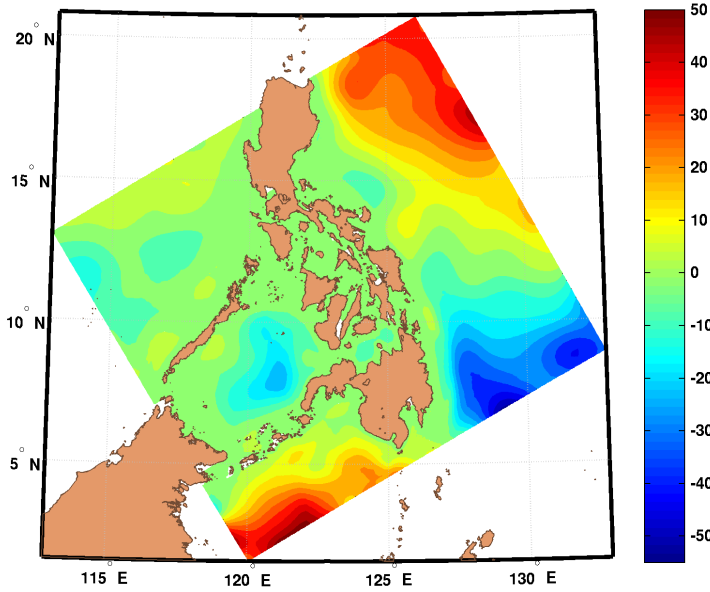


(d)  $\Delta T_{opt} = T_{opt} - T_{data}$  (e)  $\Delta T_{avg}$  where  $|\Delta T_{avg}| > |\Delta T_{opt}|$

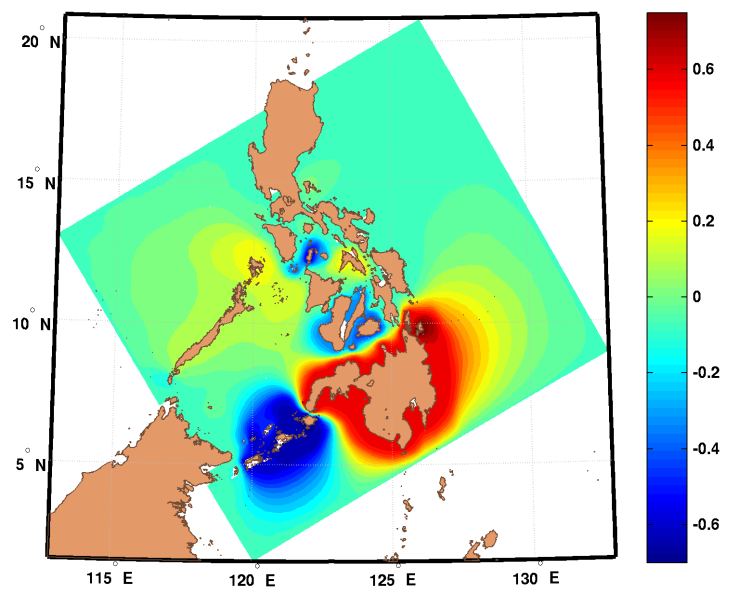


(f)  $\Delta T_{spin-up1}$  where  $|\Delta T_{spin-up1}| > |\Delta T_{opt}|$  (g)  $\Delta T_{spin-up2}$  where  $|\Delta T_{spin-up2}| > |\Delta T_{opt}|$

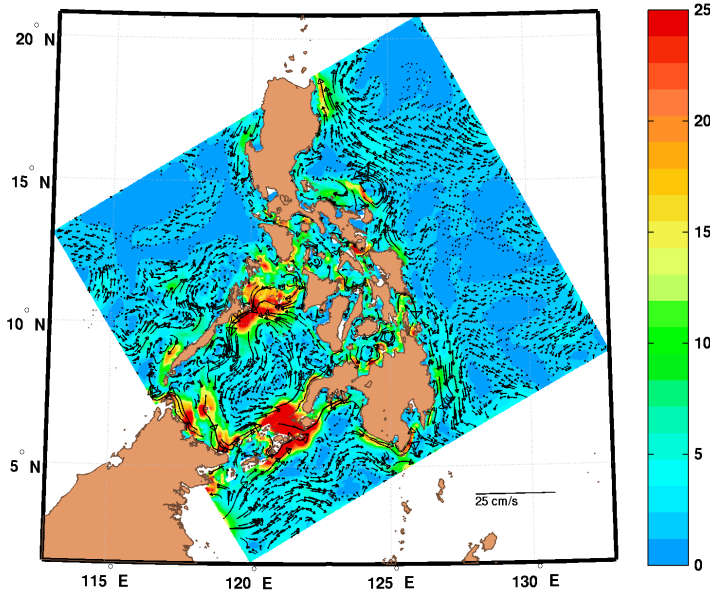
Figure 8: Comparing temperature from the 4 hindcasts shown on Fig. 6-7 to independent in situ data from 3 Sea Gliders at 2 weeks into the simulations. (a)-(b) Glider positions and data. (c) Along-track RMS errors for 4 hindcasts. (d)-(g) Along-track temperature differences for 4 hindcasts. For last 3 hindcasts, differences are shown only where they are larger than the differences of the hindcast from our optimized ICs. This hindcast shows best match to data, on average and almost everywhere.



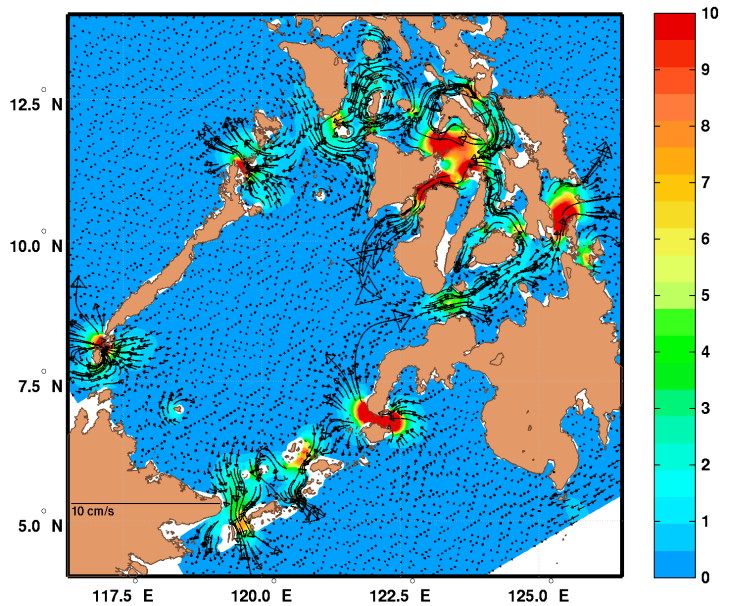
(a)  $\Psi$  (Sv) from Optimized  $\Psi_{Ciu}$



(b)  $\Psi$  Difference (Sv) (Averaged - Optimized)

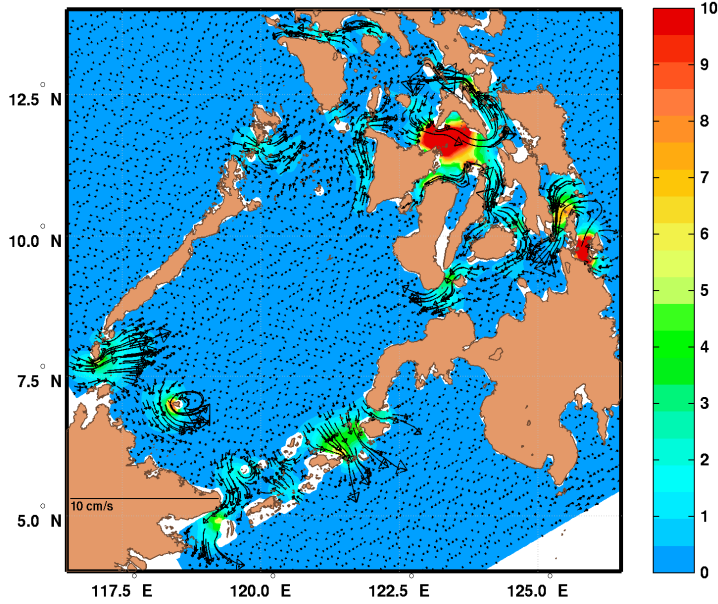


(c)  $\vec{U}_{(1)}$  (cm/s) from Optimized  $\Psi_{Ciu}$

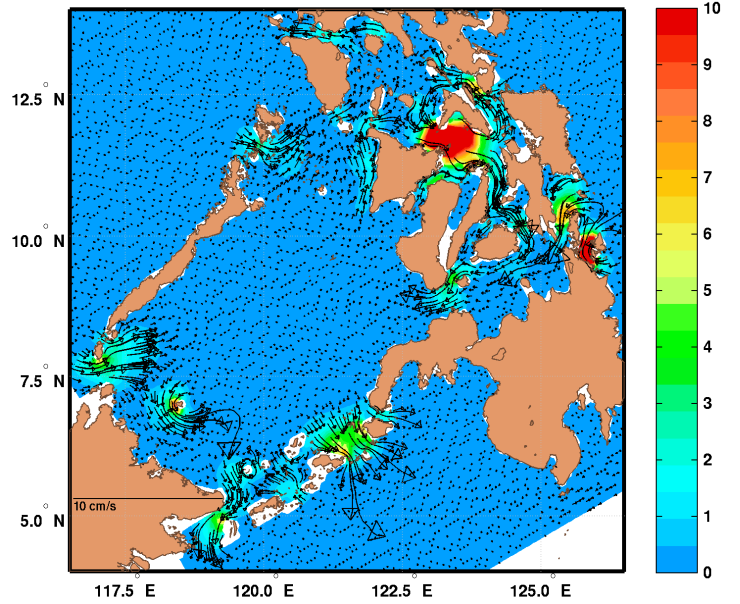


(d)  $\vec{U}_{(1)}$  Difference (cm/s) (Averaged - Optimized)

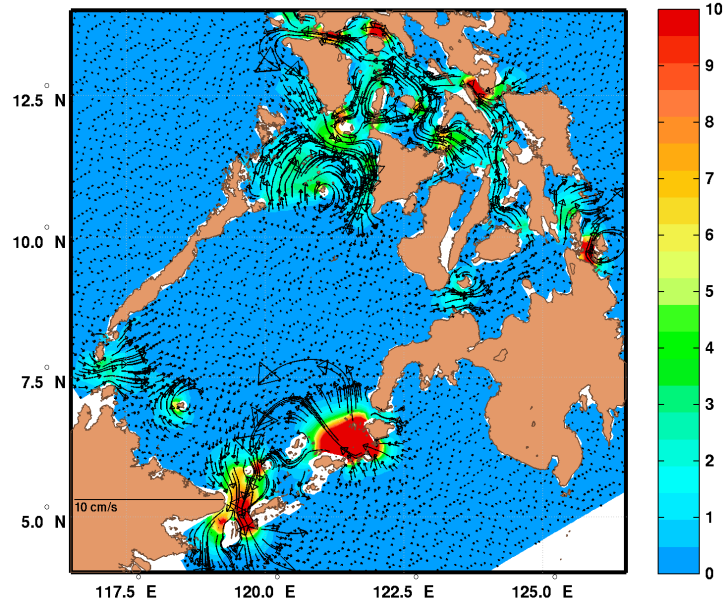
Figure 9: Philippines Archipelago. Comparison of initializations computed using  $\Psi_{Ciu}$  obtained via our optimization methodology (eq. 15) to those obtained via an averaging method (eq. 13). (a)-(b) maps of  $\Psi$ . (c)-(d) maps of  $\vec{U}_{(1)}$  magnitudes overlaid with vectors. (Note (d) is a zoom of the regions with the largest differences.) Optimizing island values removes excessive transports in various straits.



(a)  $\vec{U}_{(1)}$  difference  
Euclidean  $(d_{Eglobal\ min}/d_{Enm})^2 - \text{FMM } (\mathcal{A}_{global\ min}/\mathcal{A}_{nm})^2$

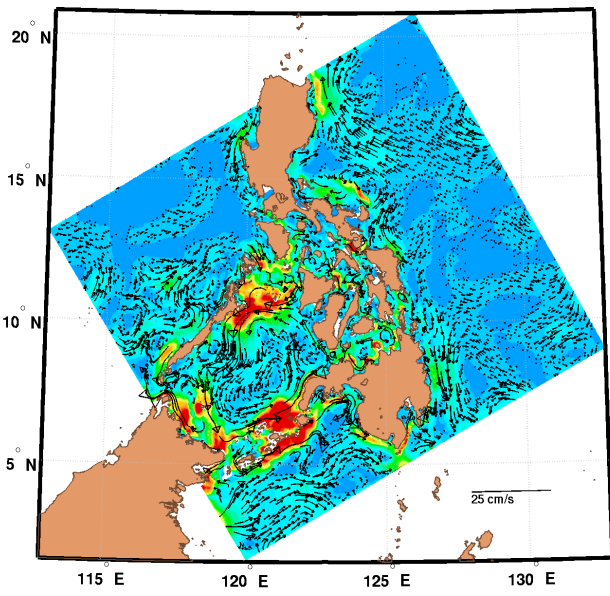


(b)  $\vec{U}_{(1)}$  difference  
FMM  $(d_{global\ min}/d_{nm})^2 - \text{FMM } (\mathcal{A}_{global\ min}/\mathcal{A}_{nm})^2$

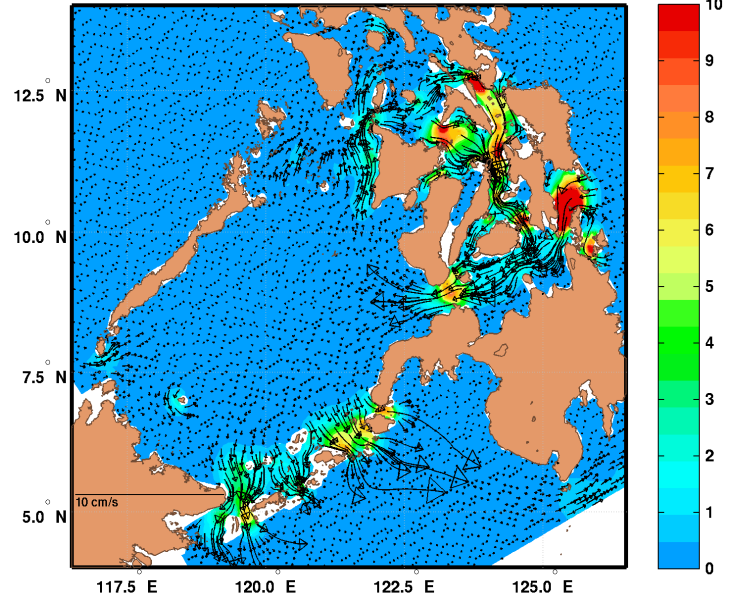


(c)  $\vec{U}_{(1)}$  difference  
FMM  $(\mathcal{A}_{global\ min}/\mathcal{A}_{nm})^2$  (velocity limit - no limit)

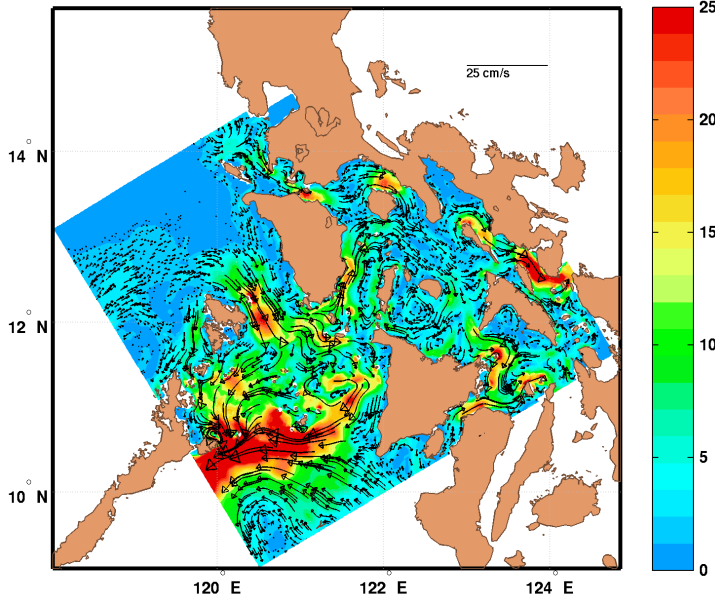
Figure 10: Differences between  $\vec{U}_{(1)}$  constructed using three weighting schemes in the Philippines and the reference result using our FMM  $\varpi_{nm}^{uu} = (\mathcal{A}_{global\ min}/\mathcal{A}_{nm})^2$  (shown on 9(c)); maps of magnitudes overlaid with vectors, restricted to the region of the largest differences. Our FMM area weightings reduces spurious large velocities in various straits. Adding velocity limiting further reduces the velocities in especially problematic straits.



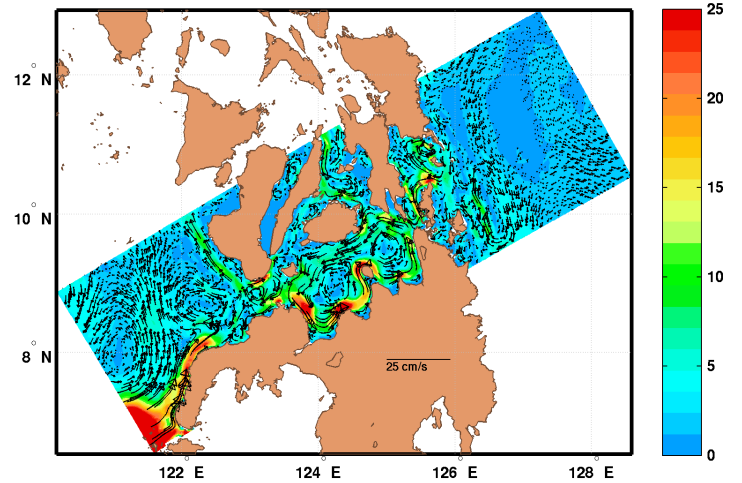
(a)  $\vec{U}_{(1)}$  (cm/s) in 9 km domain for the Philippine Archipelago



(b)  $\vec{U}_{(1)}$  (cm/s) difference (imposed - not imposed). Only showing region of large differences



(c)  $\vec{U}_{(1)}$  (cm/s) in 3 km domain for Mindoro Strait



(d)  $\vec{U}_{(1)}$  (cm/s) in 3 km domain for Bohol Sea

Figure 11:  $\vec{U}_{(1)}$  after imposing transports of 0.5 Sv through Dipolog Strait (9N,123E) and 0.3 Sv through Surigao Strait (10.5N,126E), maps of  $\vec{U}_{(1)}$  magnitudes overlaid with  $\vec{U}_{(1)}$  vectors. Using the maximum weights of Table 3, the desired transports are imposed, resulting in the reversal of the transports through these straits. The imposition of a larger transport through Dipolog than Surigao draws additional transport through the San Bernadino strait and the Visayan Sea. The added transport through Dipolog into the Sulu Sea exits through the Sulu Archipelago. Elsewhere the changes are negligible.

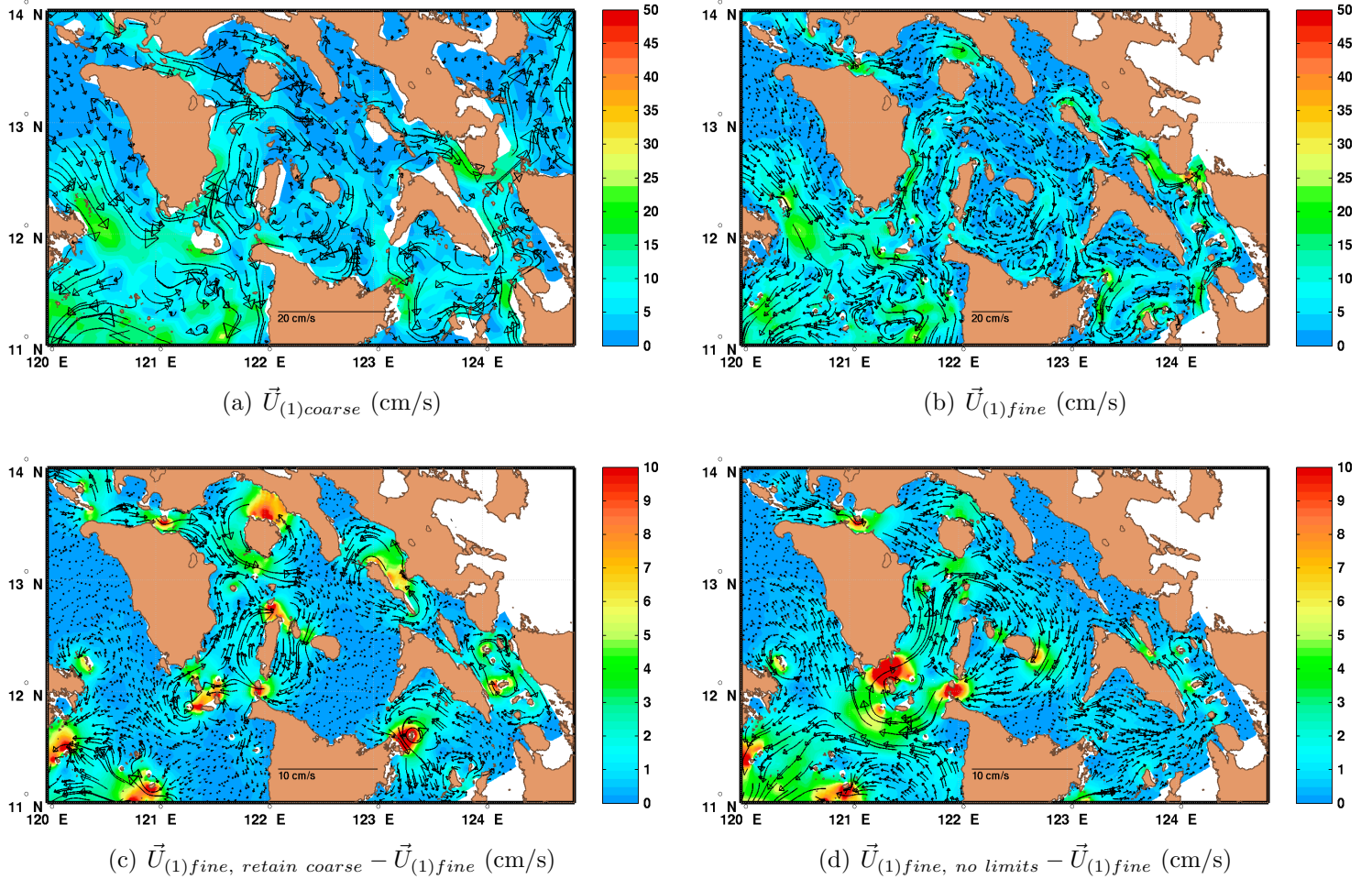


Figure 12: Testing different strategies for initializing nested sub-domains in the Philippines. Shown are maps the magnitudes of  $\vec{U}_{(1)}$  (cm/s) overlaid with  $\vec{U}_{(1)}$  vectors. (a)  $\vec{U}_{(1)}$  in coarse (9 km) domain. (b)  $\vec{U}_{(1)}$  in fine (3 km) domain, in which all island values are recomputed in fine domain using velocity limits (§3.2.2). (c) Difference between  $\vec{U}_{(1)}$  in fine (3 km) domain retaining island values from coarse domain (for inter-domain consistency) and  $\vec{U}_{(1)fine}$ .  $\vec{U}_{(1)}$  in Verde Island passage (13.5N,121E) increases from 17 cm/s to 50 cm/s due to reduced cross-section area from refined coasts and bathymetry. (d) Difference between  $\vec{U}_{(1)}$  in fine (3 km) domain without imposing velocity limits and  $\vec{U}_{(1)fine}$ .  $\vec{U}_{(1)}$  reduces in Verde Island passage from 50 to 30 cm/s but increases  $\vec{U}_{(1)}$  to 30 cm/s at southern tip of Mindoro (12N,121.25E).



- a) **Separate  $\partial D$  into:**
- Boundaries,  $\partial D^{iu}$ , along which the streamfunction values,  $\Psi_{C_n^{iu}}$ , are uncertain
  - Boundaries,  $\partial D^c$ , along which the streamfunction values,  $\Psi_{b^c} \cup \Psi_{C_k^c}$ , are certain
- b) **Compute “certain coast” streamfunction,  $\Psi_{(0)}$ , (table 2, eq. 17)**
- $$\nabla \cdot (\omega \nabla \Psi_{(0)}) = [\nabla \times (\omega H \bar{U}_{(0)})] \cdot \hat{k} \quad \Psi_{(0)}|_{\partial D^c} = \Psi_{b^c} \equiv \begin{cases} \Psi_{b^c} & \text{if } s \in \partial D^c \\ \Psi_{C_k^c} & \text{if } s \in C_k^c \end{cases}$$

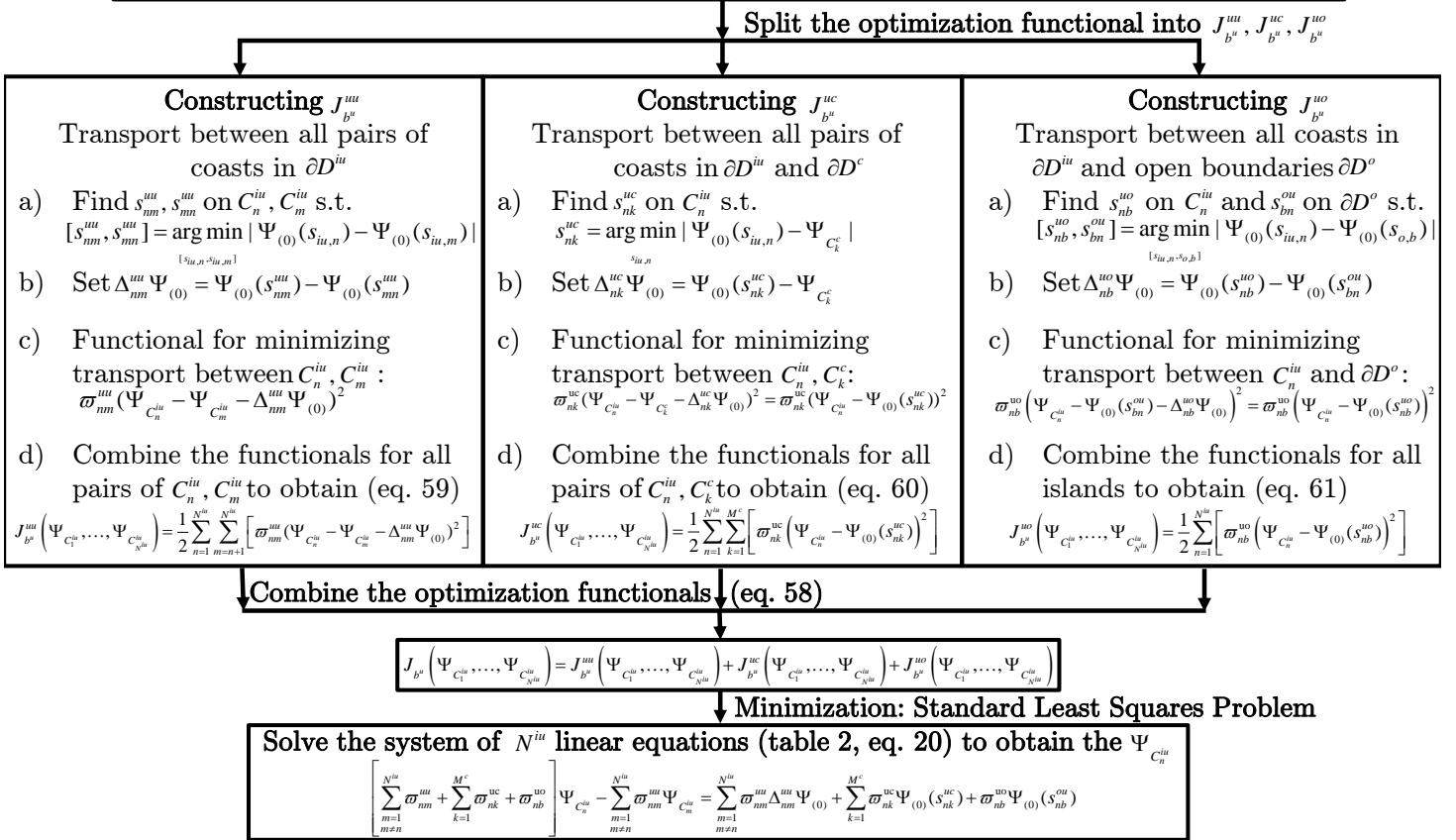


Figure 13: Flowchart for constructing  $J_{b^a}$  and computing streamfunction along uncertain islands  $\Psi_{C_n^{iu}}$ .